Alma Mater Studiorum – Università di Bologna

DOTTORATO DI RICERCA IN

Ingegneria Biomedica, Elettrica e dei Sistemi

Ciclo XXXI

Settore Concorsuale: 09/E2

Settore Scientifico Disciplinare: ING-IND/32

TITOLO TESI

Development of Grid-Connected and Front-End Converters for Renewable Energy Systems and Electric Mobility

Presentata da: **Albino Amerise**

Coordinatore Dottorato
Chiar.mo Prof. Daniele Vigo

Relatore
Chiar.mo Prof. Luca Zarri

Esame finale anno 2019

This page was intentionally left blank.

Table of contents

PREFACE

The spread of renewable energy sources and electric vehicles is increasing thanks to the greater awareness of the climate problems due to the large and long-lasting use of the non-renewable energy sources. At the Paris climate conference (COP21) in December 2015, 195 countries adopted the first-ever universal, legally binding global climate deal. The action plan defines a long-term goal of keeping the increase in global average temperature below 2°C above pre-industrial levels. Governments agreed to come together every 5 years to set more ambitious targets as required by science. Huge financial investments, hence, have been and will be allocated in order to promote further efforts in this direction.

The power converters are the technology that enables the interconnection of different players (renewable energy generation, energy storage, flexible transmission and controllable loads) to the electric power system. The integration of renewable energy sources to the power grid, however, poses significant technical challenges, since it drastically changes its topology and nature. In fact, while the traditional power generation system is centralized and the power flow unidirectional, the renewable energy is distributed and intermittent. The uncontrollability of the renewable energy source is a cause of fluctuations of the generated power in terms of voltage and frequency, which is problematic to deal with in a power grid where synchronous electrical machines are leaving place to static converters, which cannot guarantee the same robustness to those fluctuations due to their lack of inertia. Great concern is also due to the harmonic distortion that comes from the increase of power electronic devices connected to the grid. For all these reasons, great efforts are devoted in the design and control of grid-connected converters, which can improve efficiency, reliability and flexibility of the new smart grid.

The use of Power Conditioning Systems (PCSs) can be extended to motor drive applications as well. For example, it has been verified that the performance of the induction machine improves if it is fed from stator and rotor sides by two separate inverters. The rotor-side inverter, which operates as PCS, allows compensating the rotor reactive power and introduces an additional degree of freedom in the control scheme. The same principle can be applied to squirrel-cage rotor induction machines with open-end stator windings. Initially, the open-ended configuration was developed for permanent-magnet synchronous machines to reduce the current ripple in high-speed applications. It is then clear how, the same technologies, used to improve the flexibility, reliability and power quality of the power grid, can be usefully applied to motor drive applications in order to improve the performance and the quality of the currents.

In this PhD thesis, different control systems for power converters have been developed for grid-connected and motor drive applications.

In Part I, the operation of Active Power Filters (APFs), used working as power factor corrector and harmonic compensator to improve the power quality of the grid has been investigated. Particular attention was paid to the study of the current controller, which represents the core of an APF. On this topic, according to the state of the art, the most performant current controllers are represented by the resonant and repetitive controllers, which have been studied and tested on a laboratory prototype of APF.

A problem that has been investigated in this PhD work is the exploitation of the DC-link voltage of the APF, in the case of voltage overmodulation or current saturation, when the reduction of the high frequency harmonics is performed by an array of resonant controllers. In this regard, three different saturation algorithms have been proposed and tested, with the goal to improve the overall performance of the filter in this critical condition while ensuring an adequate stability margin.

In Chapter 1, the study and development of the control system for an APF has been developed. The main issue related to this application are the synchronization with the grid, the control of the floating capacitor and the current control.

In Chapter 2, the current controller for an APF is investigated. In particular, two different kind of current controllers, the resonant and repetitive controllers, have been compared in terms of performance, stability and implementation issues.

In Chapter 3, the problem of the saturation of a multi-resonant controller has been under study.

Although it is believed that the theory of PCSs can be applied only in grid-connected applications, it can lead to remarkable results also when the voltage source are the electromotive forces of an electric motor.

In Part II of this thesis, the control system developed for an APF has been applied to three kinds of electrical motors in open-end winding configurations. This configuration, in fact, allows the additional power converter to work as power factor corrector and harmonic compensator, making possible to extend the constant power speed range of the motor and to work in linear and overmodulation zones, without compromising the quality of the motor currents.

In Chapter 4, a general mathematical model for an open-end winding motor has been developed and, based on this study, the control system for this drive has been tested on three different electrical motors, such as:

- Induction Motor (IM) in Chapter 5 ,
- Surface Permanent Magnet Synchronous Motor (SPMSM) in Chapter 6,
- Synchronous Reluctance Motor (Sync-Rel) in Chapter 7.

Finally, the conclusions are drawn and the results discussed.

The main contributions of this PhD work can be summarized as follows:

- development of control systems for repetitive current controllers, where the effects of the delay, introduced by the discretization process, on the performance and stability of the system are highlighted;
- development of saturation algorithms in multi-resonant current controllers for the optimization of the DC-link voltage;
- development of control systems for induction, SPM and Sync-Rel motors in open-end windings configuration, which allows one to improve the drive performance over all the speed range.

Part I

GRID-CONNECTED CONVERTERS

Chapter 1

ACTIVE POWER FILTER

The issues of grid connected converters are similar despite the differences of the applications, such as PV power systems and wind power systems [1]. These common problems are related to synchronization with the grid, harmonic control, detection and management of islanding conditions for several applications.

In this PhD work, the focus is mostly on harmonic control.

The circulation of current harmonics in the power grid generates voltage harmonics, due to the voltage drop on the power grid impedance. Such voltage harmonics are a problem especially in weak power grid conditions, i.e., with high impedance. This can be the cause of various damages to the power grid infrastructure of both supplier and users, such as:

- overheating of cables and transformers, which leads to premature aging of the insulation and therefore higher maintenance costs;
- reverse sequences in rotating machines, which causes torque fluctuations;
- saturation of the magnetic cores of the transformers, caused by possible continuous components of the current, generated for example by asymmetries in the operation of the converters;
- malfunction of the control devices.

Concerning power quality, a further problem is represented by the phase displacement between power grid voltage and current, which causes an increase in the currents making therefore necessary the oversizing of cable and electrical devices.

Among the possible solutions there are the passive filters, which can be classified depending on their cutting frequency as:

- *sine filter*, designed to compensate low frequency harmonics (5, 7, ...,19). It can be of the first order, if it is composed of an inductance, or of the second order if a capacitor is added;
- *EMI filter,* designed to compensate high frequency emissions;
- *Choke filter,* used to reduce common mode currents.

Those solutions, however, are not very flexible and their design has to change if the set of harmonics that should be compensated changes. These drawbacks can be overcome through

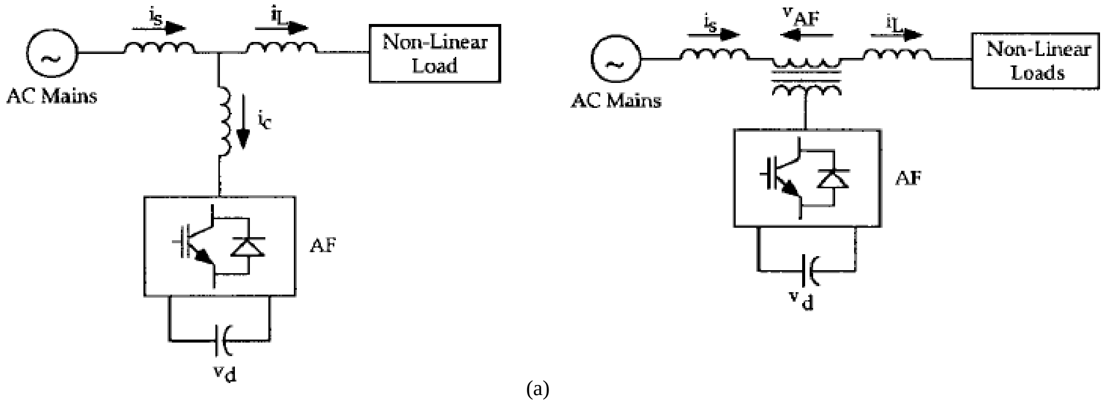

(a) (b)

Fig. 1.1. Active Power Filter in shunt configuration (a) and series configuration (b).

the use of Active Power Filters (APFs), which dynamically adapt to the power grid condition. They fall into the category of Power Conditioning Systems (PCSs) and are used to improve the power quality of the grid by working as a power factor corrector and harmonic compensator [2].

There are mainly two possible configurations, shown in Fig. 1.1. The shunt configuration, Fig. 1.1 (a), is the most used since it can be installed without modifying the plant, as required by the series configuration, Fig. 1.1 (b). It is composed of an inverter connected to the Point of Common Coupling (PCC) through a passive filter.

The inverter can store the electrostatic energy necessary for its operation as electrostatic energy in a capacitor, thus leading to the category of Voltage Source Inverters (VSI) shown in Fig. 1.2(a), or as magnetic energy in an inductor. This solution is referred to as Current Source Inverter (CSI) and it is shown in Fig. 1.2 (b).

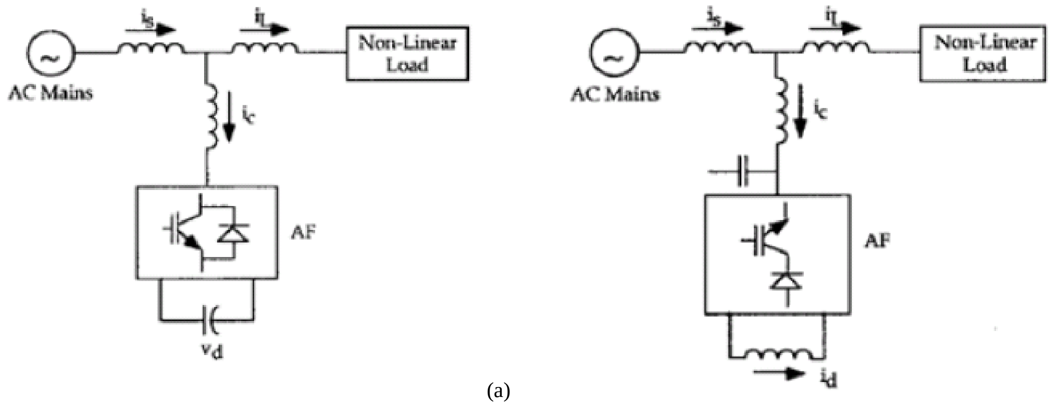

(a) (b)

Fig. 1.2. Active Power Filter VSI type (a) and CSI type (b).

In this chapter, the operation principles of an APF are discussed and the mathematical model is studied. The control system developed is explained in its part and the reference signal for the current controller, which represents the core of the APF, is derived. The design of the current controller, due to its importance, will be widely studied in Chapter 2.

1.1 MATHEMATICAL MODEL OF A SHUNT APF

In this PhD work a VSI type APF, connected through a decoupling inductance, is considered. It is shown in Fig 1.3.

A. *Operation Principles of a Shunt APF*

The operation of an APF has to be consistent with the available voltage across the floating capacitor C. The voltage E_F of the DC link depends on the electrostatic energy W_C stored in the capacitor

$$W_C = \frac{1}{2} C E_F^2 , \tag{1.1}$$

whose rate of change is related to the instantaneous active power of the converter. If the losses of the APF are neglected, the following expressions can be written:

$$\frac{d}{dt}\left(\frac{1}{2} C E_F^2\right) = P_F \tag{1.2}$$

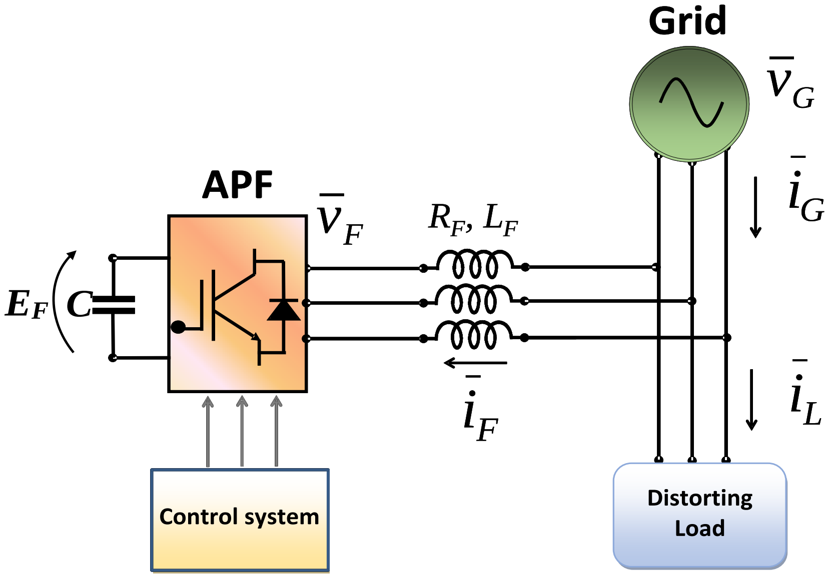

Fig 1.3. Active Power Filter VSI type, connected to the power grid in shunt configuration through a decoupling inductance.

$$P_F = \frac{3}{2}\overline{v}_F \cdot \overline{i}_F \tag{1.3}$$

where P_F is the instantaneous active power at the input of the APF, $\overline{v}_F$ and $\overline{i}_F$ are respectively the space vectors of the output voltage and current of the APF, and "·" is the dot product operator, defined as the sum of the products of the corresponding components of the two vectors.

In order to control the filter current, it is necessary to find the relationship between $\overline{v}_F$ and $\overline{i}_F$. In a reference frame aligned with the space vector of the grid voltage $\overline{v}_G$, this relationship is given by the equation of the decoupling inductance:

$$\overline{v}_G = R_F\overline{i}_F + j\omega L_F\overline{i}_F + L_F\frac{d\overline{i}_F}{dt} + \overline{v}_F\ , \tag{1.4}$$

where ω is the angular frequency of the space vector of the grid voltage $\overline{v}_G$, R_F and L_F are respectively the filter resistance and inductance.

It is straightforward to find the expression of the instantaneous active power P_G exchanged by the grid with the APF through the dot product of (1.4) by $\frac{3}{2}\overline{i}_F$:

$$P_G = \frac{3}{2}R_F i_F^2 + \frac{d}{dt}\left(\frac{3}{4}L_F i_F^2\right) + P_F\ , \tag{1.5}$$

where

$$P_G = \frac{3}{2}\overline{v}_G \cdot \overline{i}_F = \frac{3}{2}v_G i_{Fd}\ . \tag{1.6}$$

In (1.6), i_{Fd} is the d-axis component of the filter current $\overline{i}_F$, and v_G is the magnitude of the grid voltage $\overline{v}_G$.

Equation (1.5), combined with (1.2), can be rewritten to emphasize the derivative of the total electromagnetic energy of the system.

$$\frac{d}{dt}\left(\frac{1}{2}CE_F^2 + \frac{3}{4}L_F i_F^2\right) = P_G - \frac{3}{2}R_F i_F^2\ . \tag{1.7}$$

If the Joule losses of the filter resistance are negligible, (1.7) shows that the rate of change of the energy stored in the reactive elements of the system depends on the instantaneous active power P_G, which is proportional to i_{Fd} as shown in (1.6). Therefore, the voltage level of the DC-link capacitor can be indirectly controlled by adjusting the total energy of the system through i_{Fd}, under the assumption that the magnetic energy of the filter inductance is regarded as a measurable disturbance, which can be properly compensated.

A similar procedure can be used to find the relation between the reactive power exchanged by the power grid and the APF by considering the dot product between (1.4) and $\frac{3}{2} j\bar{i}_F$:

$$Q_G = -\frac{3}{2}\omega L_F i_F^2 + Q_F , \tag{1.8}$$

where

$$Q_G = -\frac{3}{2} v_G i_{Fq} . \tag{1.9}$$

From (1.8) and (1.9) it can be seen that it is possible to control the reactive power injected into the grid by the APF by acting on the q-component of the filter current i_{Fq} and compensating the reactive power of the decoupling inductance.

With reference to Fig 1.3, if $\bar{i}_L$ and $\bar{i}_G$ respectively denote the load and grid current vectors, the balance of the currents at the PCC leads:

$$\bar{i}_F = \bar{i}_G - \bar{i}_L . \tag{1.10}$$

If the high frequency components, identified by the subscript “HF”, are considered, (1.10) allows finding the harmonic content of $\bar{i}_F$ that nullifies $\bar{i}_{G,HF}$:

$$\bar{i}_{F,HF,ref} = -\bar{i}_{L,HF} . \tag{1.11}$$

Equation (1.11) states that the shunt APF has to generate the high frequency components of the load current so as to relieve the grid from providing the undesired harmonics.

Since the energy carried by the high-frequency harmonics of the voltages and currents is usually much lower than that of the fundamental components, it results that the low frequency components of the i_{Fd} and i_{Fq} can be used to control the average energy of the capacitor and the reactive power at the PCC, according to (1.6) and (1.9), while the high frequency components can be used to reduce the demand of distorted currents of the grid, according to (1.11).

1.2 CONTROL SYSTEM

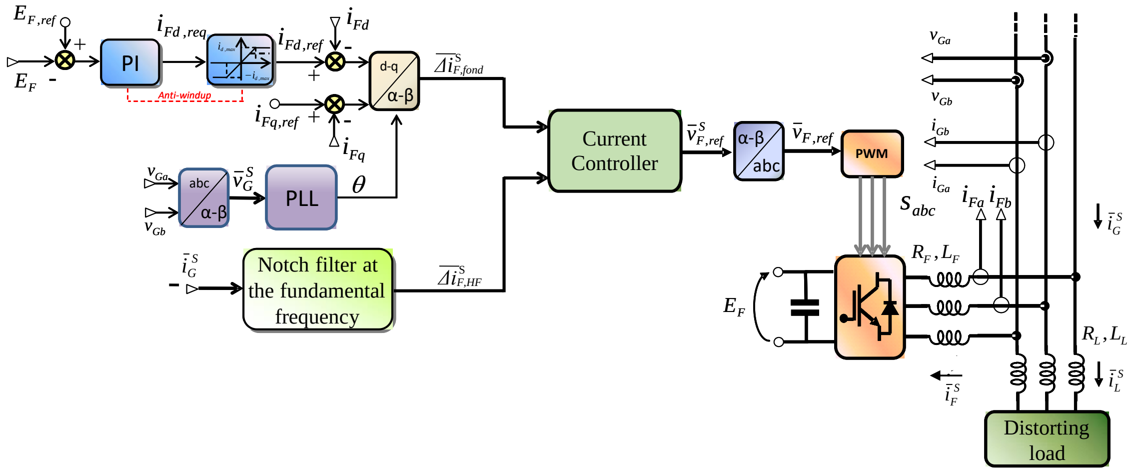

Fig 1.4. APF control scheme

The control system has to:

- provide the inverter with the reference voltages that allow to generate a filter current $\bar{i}_F$ necessary to compensate the power factor and the current harmonics in the power grid;
- maintain control the floating bridge voltage E_F at the reference value that guarantees the correct operation of the APF.

The measurements required by the control system, as shown in Fig 1.4, are:

- power grid voltages, used for the synchronization;
- voltage across the floating capacitor;
- filter current $\bar{i}_F$, which is the one to be controlled, and one current between the grid and load current. It has been chosen to measure the grid current since it represents the target variable.

B. *Phase Locked Loop (PLL)*

The mathematical model has been implemented on a rotating reference frame aligned with the space vector of the power grid voltage, Fig 1.5(a).

Fig 1.5(b) shows the scheme of the PLL. It allows one to estimate the phase angle θ that nullifies, instant by instant, the q-component of the fundamental component of the grid voltage.

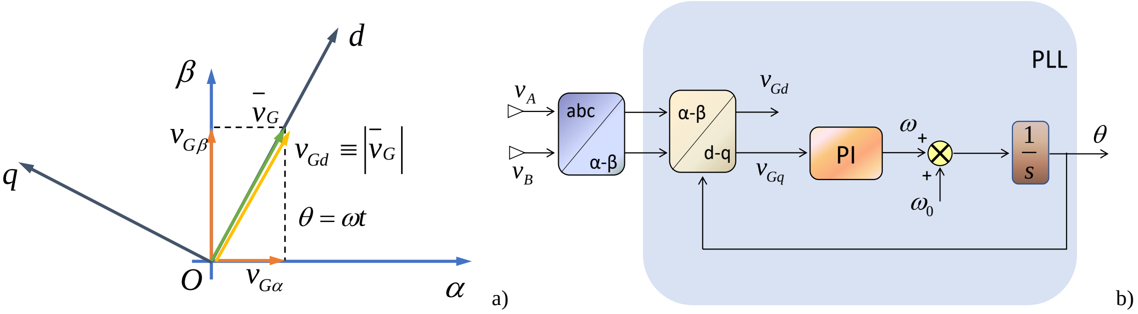

Fig 1.5. Rotating reference frame aligned with the space vector of the grid voltage (a) and control scheme of the PLL (b).

C. *Control of the DC-link*

Let us consider the expression of the active power balance (1.7) and develop the derivative:

$$\left(CE_F\frac{dE_F}{dt}+\frac{E_F^2}{R_C}\right)+\frac{3}{2}L_F i_F\frac{di_F}{dt}=\frac{3}{2}v_G i_{Fd}-\frac{3}{2}R_F i_F^2\,. \tag{1.12}$$

where power loss on the bleeder resistor R_C has also been considered.

To find the transfer function of the DC-link voltage loop it is possible to apply small variations to the nominal values as follows:

$$\begin{gathered} E_F = E_{F,nom}+\Delta E_F \\ i_{Fd} = i_{Fd,nom}+\Delta i_{Fd} \end{gathered} \tag{1.13}$$

Substituting (1.13) in (1.12) and under the assumption that $i_{Fq} = 0$, following expression can be written:

$$\begin{aligned} &\left(C\left(E_{F,nom}+\Delta E_F\right)\frac{d\left(E_{F,nom}+\Delta E_F\right)}{dt}+\frac{\left(E_{F,nom}+\Delta E_F\right)^2}{R_C}\right)= \\ &=\frac{3}{2}v_G\left(i_{Fd,nom}+\Delta i_{Fd}\right)-\frac{3}{2}R_F\left(i_{Fd,nom}+\Delta i_{Fd}\right)^2+ \\ &-\frac{3}{2}L_F\left(i_{Fd,nom}+\Delta i_{Fd}\right)\frac{d\left(i_{Fd,nom}+\Delta i_{Fd}\right)}{dt} \end{aligned} \tag{1.14}$$

It is possible to neglect the terms of a higher order, such as ΔE_F^2, Δi_{Fd}^2, $\Delta i_{Fd}\frac{d\Delta i_{Fd}}{dt}$ and $\Delta E_F\frac{d\Delta E_F}{dt}$. Equation (1.14) becomes:

$$\begin{aligned} & CE_{F,nom}\frac{d\Delta E_F}{dt}+\frac{\left(E_{F,nom}^2+2E_{F,nom}\Delta E_F\right)}{R_C}=\frac{3}{2}v_G\left(i_{Fd,nom}+\Delta i_{Fd}\right)+ \\ & -\frac{3}{2}R_F\left(i_{Fd,nom}^2+2i_{Fd,nom}\Delta i_{Fd}\right)-\frac{3}{2}L_F i_{Fd,nom}\frac{d\Delta i_{Fd}}{dt} \end{aligned} \tag{1.15}$$

In addition, by considering the steady state equation

$$\frac{E_F^2}{R_C}=\frac{3}{2}v_G i_{Fd}-\frac{3}{2}R_F i_F^2 \tag{1.16}$$

it is possible to rewrite (1.15) as follows:

$$CE_{F,nom}\frac{d\Delta E_F}{dt}+\frac{E_{F,nom}\Delta E_F}{R_C}=\frac{3}{2}v_G\Delta i_{Fd}-3R_F i_{Fd,nom}\Delta i_{Fd}-\frac{3}{2}L_F i_{Fd,nom}\frac{d\Delta i_{Fd}}{dt}\,. \tag{1.17}$$

Expression (1.17) can be written in the Laplace domain as follows

$$\left(sCE_{F,nom}+\frac{2E_{F,nom}}{R_C}\right)\Delta E_F=\frac{3}{2}\left(v_G-2R_F i_{Fd,nom}-sL_F i_{Fd,nom}\right)\Delta i_{Fd} \tag{1.18}$$

And, finally, the transfer function for the DC-link voltage becomes:

$$G_{DC}=\frac{\Delta E_F}{\Delta i_{Fd}}=\frac{3}{4}\frac{R_C\left(v_G-2R_F i_{Fd,nom}\right)}{E_{F,nom}}\frac{\left(1-\tau_L s\right)}{\left(1+s\tau_C\right)} \tag{1.19}$$

where

$$\tau_C=\frac{CR_C}{2} \tag{1.20}$$

$$\tau_L=\frac{L_F i_{Fd,nom}}{v_G-2R_F i_{Fd,nom}}\,. \tag{1.21}$$

Equation (1.20) expresses is a time constant related to the floating capacitor, while (1.21) represents a time constant related to the transient of the decoupling inductance to reach the flux value set by the d-component current $i_{Fd,nom}$. It can be noted that (1.19) includes an unstable real zero, whose sign depends on the sign of $i_{Fd,nom}$, which is related to the condition of charge or discharge of the floating capacitor voltage. However, the value of τ_L is much smaller than τ_C and describes a fast transient. It is then possible to neglect its contribute for the DC-link voltage regulation, which can be achieved through a PI controller with an antiwind-up scheme, implemented in the reference frame synchronous with the power grid voltage, as shown in Fig 1.4. The reference value of the q-component of the filter current is a degree of freedom that can be used to exchange reactive power with the power grid.

The reference values are then compared with the measurement of the filter current in order to get the input error at the fundamental frequency for the current controller.

D. *High Frequency Current Reference*

The input error for the high frequency current is equal to:

$$\Delta\bar{i}_{F,HF} = \bar{i}_{F,HF,ref} - \bar{i}_{F,HF}\ . \tag{1.22}$$

By substituting (1.11) in (1.22) and taking into account (1.10) one finds

$$\Delta\bar{i}_{F,HF} = -\bar{i}_{G,HF}\ . \tag{1.23}$$

The high frequency content of the power grid current is obtained by means of a notch filter at the fundamental frequency. This kind of filter allows one to eliminate a frequency component from a signal. Its transfer function is:

$$G_{notch} = \frac{s^2 + \omega_0^2}{s^2 + 2\delta\omega_0 s + \omega_0^2} \tag{1.24}$$

where ω_0 is the frequency that should be eliminated and δ is the damping factor. It is possible to analyze its behavior through the study of the Bode diagram, shown in Fig 1.6, where the magnitude and phase variables are plotted for different values of the damping factor δ.

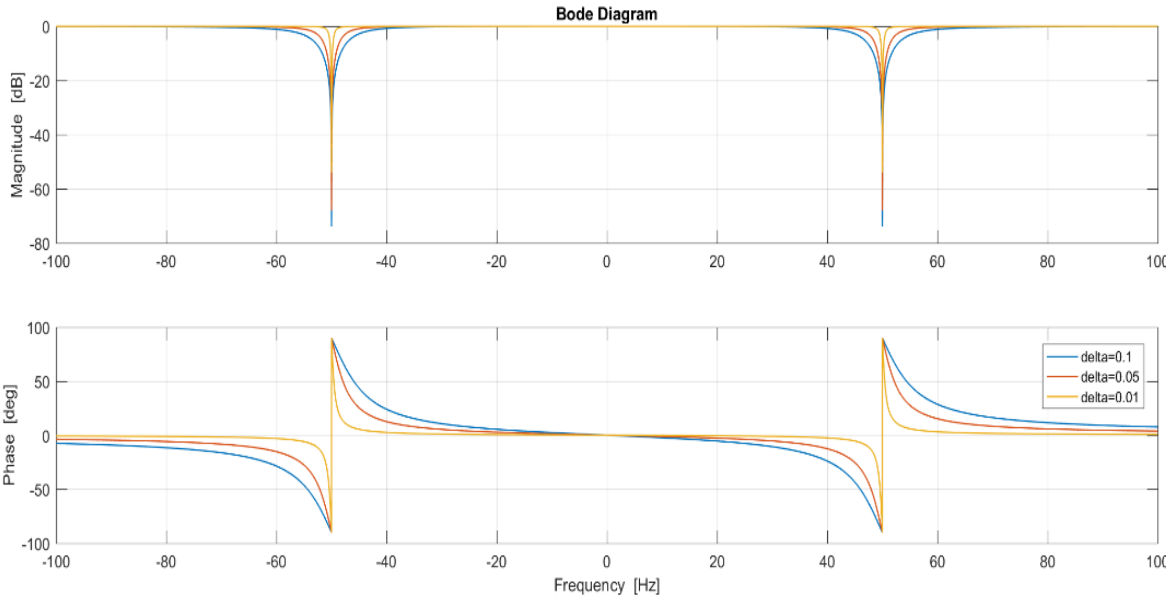

Fig 1.6. Bode diagram of the magnitude and phase of a notch filter for different value of δ.

A decrease in the value of δ leads to a narrower frequency band around ω_0.

The expression for the high frequency input error for the current controller (1.23) can be written as:

$$\Delta\bar{i}_{F,HF}^{S} = G_{notch}\left(-\bar{i}_{G}^{S}\right). \tag{1.25}$$

where the superscript *S* means that the variables are written in the stationary reference frame.

Equations (1.6), (1.9) and (1.25) define the reference current, in its frequency components, that has to be tracked by the current controller which is studied in the next chapter.

Chapter 2

CURRENT CONTROL

Several approaches have been investigated and tested for the current control loop, which, usually, has to track a reference signal composed of several harmonic components. Proportional-integral controllers implemented in a reference frame rotating at the frequency of the disturbing harmonics can be used [3], [4], [5]. Dead-beat and hysteresis controllers [6], [7], [8] require less computational effort than PI controllers implemented in rotating reference frames, but they are not so effective in compensating the harmonic distortion. Recently, repetitive control has been proposed due to its excellent performance in terms of harmonic compensation and low computational burden [9], [10]. Another solution that has become popular in recent years is the use of resonant controllers implemented in the stationary reference frame, or in rotating reference frames, to cancel more harmonic components of the grid current at a time [11], [12]. In [13] several kinds of resonant controllers are compared, such as multiple rotating integrators, stationary frame resonant controllers, proportional-sinusoidal signal integrators and vector PI controllers, in order to determine, for each method, the operating frequency range and the stability limit. A classification of the current control methods is shown in Fig 2.1.

In this PhD work, the methods under investigation are the resonant current control and the repetitive current control.

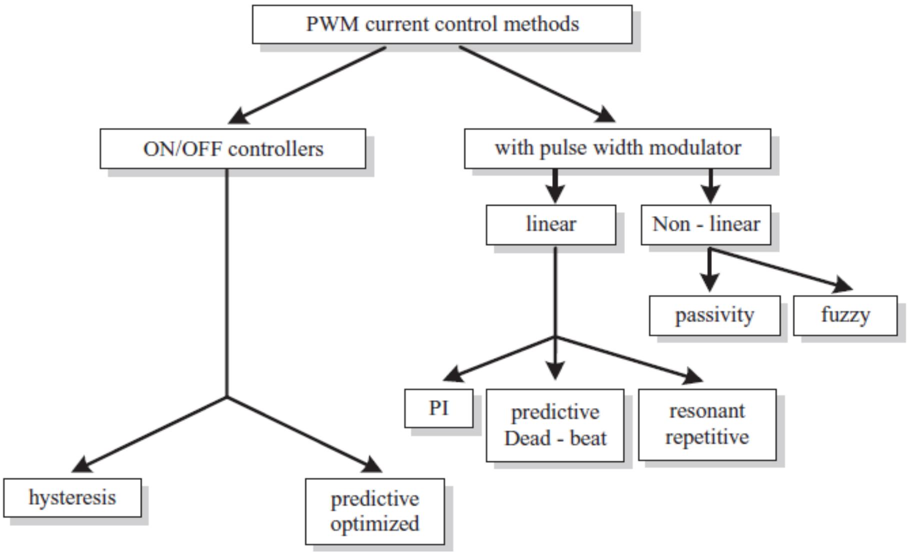

Fig 2.1 Current control methods.

2.1 RESONANT CONTROLLER

The resonant regulators are able to track sinusoidal references, of direct and inverse sequence simultaneously, with zero steady-state error. They are equivalent to PI regulators implemented in two reference frames having equal and opposite angular frequencies. Their implementation in the stationary reference frame does not require the Park transform, thus allowing a substantial reduction in the computation time. Their use is widespread in power electronics, such as active filters, active rectifiers, wind turbines, hydraulic turbines, inverters for photovoltaic applications, uninterruptible power systems, etc.

A. *Study of the Transfer Function of a Resonant Controller*

The transfer function of a Proportional Resonant (PR) controller in the Laplace domain is usually expressed as:

$$R(s) = K_p + K_i \frac{s}{s^2 + \omega_0^2} = K_p + K_i I_R(s) \tag{2.1}$$

where K_p e K_i represent the proportional and integral gains respectively, while the function $I_R(s)$ is the resonant term, which has infinite gain at the angular frequency of resonance $\pm\omega_0$. The integral gain K_i affects the band width around the resonance peak, and the amplitude of the resonance peak. The value of K_p defines the gain of $R(s)$ in the remaining part of the frequency domain. Fig. 2.2 shows the Bode diagram of $R(s)$, with $\omega_0 = 2\pi 50$ rad s^{-1}, K_p constant, for different values of K_i.

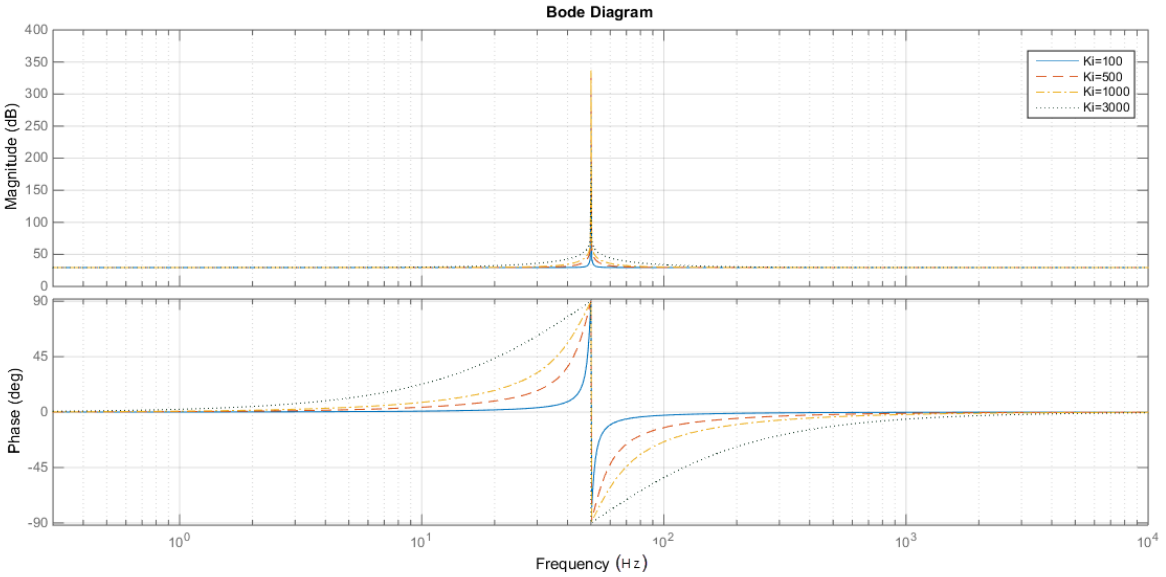

Fig. 2.2 Bode diagram of the magnitude and phase of a PR for different values of K_i.

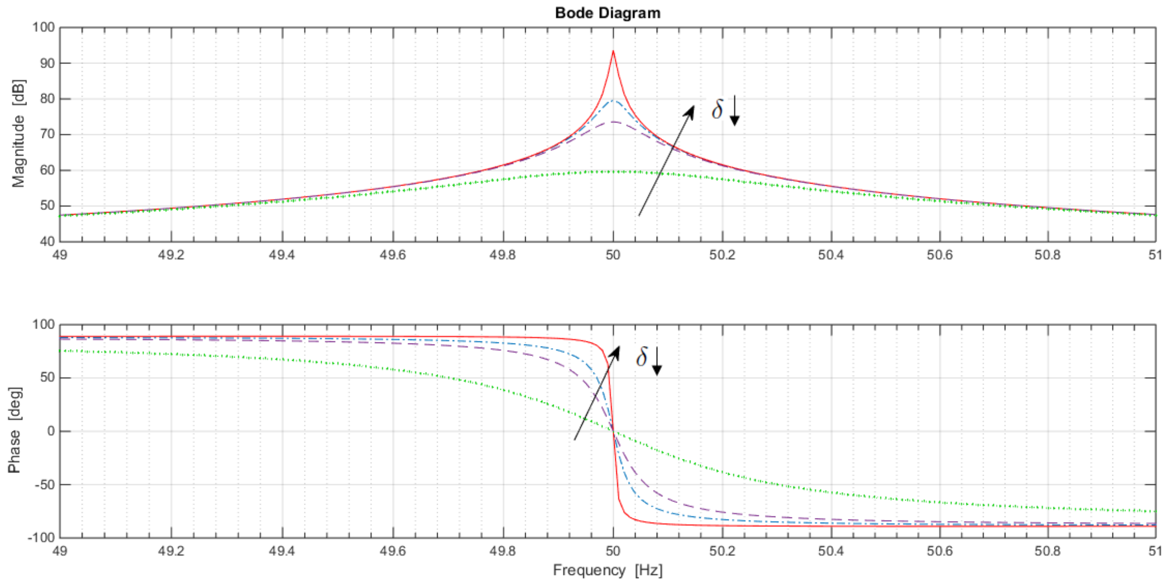

Fig. 2.3 Bode diagram of the magnitude and phase of a PR for different value of δ.

However, the transfer function in (2.1) is quite sensitive to any mismatch in the resonance frequency and this can be cause of instability, due to the infinite gain. In order to improve the controller robustness, the expression of $I_R(s)$ can be modified as follow:

$$I_R(s) = \frac{s}{s^2 + 2\delta\omega_0 s + \omega_0^2} \tag{2.2}$$

where δ is the dumping coefficient, whose increase corresponds to a decrease in the gain at the resonance frequency, as shown in Fig. 2.3.

As the resonance frequency increases the delay introduced by the process of discretization, through the sample and hold, and the delay due to the computation time required by the inverter before generating the output signal, can cause a decrease of the performance or even the instability. It is hence necessary to modify the transfer function (2.2) so as to take into account these delays.

According to [14], it can be rewritten as:

$$I_R(s) = \frac{s\cos(\theta) - \omega_0 \sin(\theta)}{s^2 + 2\delta\omega_0 s + \omega_0^2} \tag{2.3}$$

where θ represents the delay that affects the regulator. Its value is:

$$\theta = N T_C \omega_0 . \tag{2.4}$$

The value of N represents the number of sampling periods T_S, at the defined resonance angular frequency ω_0.

For the sake of clarity, it is useful to understand the changes that are brought to (2.3).

Let us consider the time domain expression of $I_R(S)$ in (2.1) by applying the reverse Laplace transform

$$I_R(t) = L^{-1}\left[\frac{s}{s^2+\omega_0^2}\right] = \cos\left(\omega_0 t\right). \tag{2.5}$$

which represents a sinusoidal signal at the angular frequency of ω_0.

Applying the same procedure to the expression of $I_R(S)$ one finds:

$$\begin{aligned} I_R(t) &= L^{-1}\left[\frac{s\cos\left(\theta\right)-\omega_0\sin\left(\theta\right)}{s^2+2\delta\omega_0 s+\omega_0^2}\right] = \\ &= \cos\left(\theta\right)L^{-1}\left[\frac{s}{s^2+\omega_0^2}\right] - \sin\left(\theta\right)L^{-1}\left[\frac{\omega_0}{s^2+\omega_0^2}\right] = \\ &= \cos\left(\theta\right)\cos\left(\omega_0 t\right) - \sin\left(\theta\right)\sin\left(\omega_0 t\right) = \cos\left(\omega_0 t+\theta\right) \end{aligned} \quad . \tag{2.6}$$

which, as expected, gives a sinusoidal signal at the angular frequency of ω_0 with initial phase θ.

It is now possible to write the final form of the proportional-resonant controller as:

$$R(s) = K_p + K_i\frac{s\cos\left(\theta\right)-\omega_0\sin\left(\theta\right)}{s^2+2\delta\omega_0 s+\omega_0^2}. \tag{2.7}$$

B. *Implemented Multi-Resonant Current Control*

The control system developed for the control of the current is composed by an array of proportional-resonant regulators, consisting of a regulator for each harmonic in the set ω_1, ω_2, …, ω_N that are intended to be controlled.

As it can be seen in Fig 2.4, the set of resonant controllers can be divided in two parts:

- the first part consists in a proportional resonant regulator at the fundamental frequency, used to control the exchange of active and reactive power,

$$R_1\left(s\right) = K_p^{(1)} + K_i^{(1)}\frac{s\cos\left(\theta_1\right)-\omega_1\sin\left(\theta_1\right)}{s^2+2\delta_1\omega_1 s+\omega_1^2}; \tag{2.8}$$

- the second part is composed of the remaining regulators, whose harmonic order is defined by the letter *k*, used to compensate the harmonic distortion in the power grid,

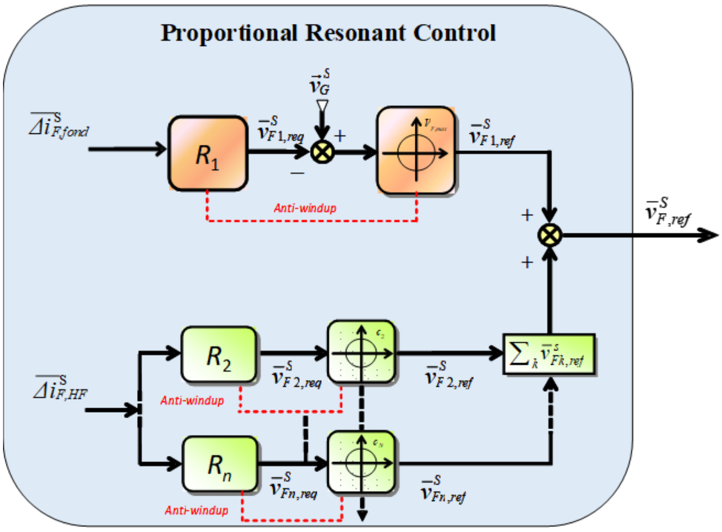

Fig 2.4 Current control methods.

$$\sum_{k=2,\ldots n} R_k(s) = \sum_{k=2,\ldots n} \left(K_p^{(k)} + K_i^{(k)} \frac{s\cos(\theta_k) - \omega_k \sin(\theta_k)}{s^2 + 2\delta_k \omega_k s + \omega_k^2} \right). \tag{2.9}$$

The reference output voltage collects these two parts multiplied by the respective current input errors as follow:

$$\overline{v}^S_{F,ref} = \overline{v}^S_{F1,ref} + \sum_{k=2,\ldots,n} \overline{v}^S_{Fk,ref} \tag{2.10}$$

$$\overline{v}^S_{F1,ref} = -R_1(s)\Delta\overline{i}^S_{F,fond} + \overline{v}^S_G \tag{2.11}$$

$$\sum_{k=2,\ldots,n} \overline{v}^S_{Fk,ref} = \sum_{k=2,\ldots,n} R_k(s)\Delta\overline{i}^S_{F,HF} \tag{2.12}$$

Each resonant controller needs an antiwind-up algorithm. The analysis of the saturation of a multi-frequency regulator is part of this PhD work and it will be widely discussed in the next chapter.

C. *Tuning of the Current Controllers*

Let us focus on an example of the tuning of the PR controller of the fundamental component of the current and of the DC-link PI controller, shown in Fig 1.4, that defines the reference i_{Fd}. It is necessary to start the analysis from the inner loop, i.e. the current loop, shown in Fig 2.5. The current open loop transfer function is composed of three terms, which are the PR controller in (2.8), the transfer function of the inverter and the one of the plant

$$G_{curr,ol} = R_1 * G_{INV} * G_{PLANT}, \tag{2.13}$$

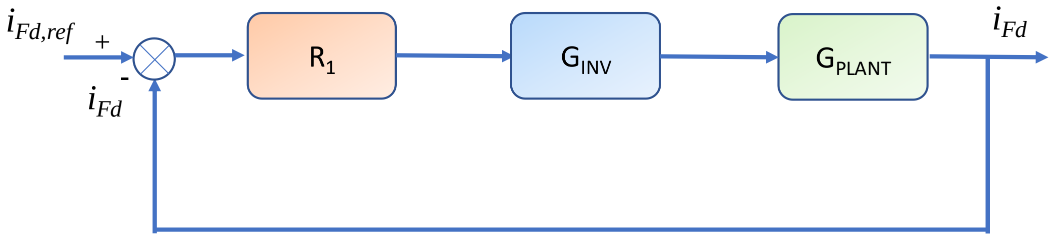

Fig 2.5 Current loop.

where

$$G_{INV} = e^{-\frac{3}{2}T_S s}, \tag{2.14}$$

$$G_{PLANT} = \frac{1}{R_F + L_F s}. \tag{2.15}$$

The value of the sampling time T_C is 100 µs, while R_F is 26 mΩ and L_F is 2,36 mH in the experimental set-up.

As already mentioned, a PR regulator is equivalent to two PIs implemented in two reference systems rotating at positive and negative speed. It is possible to tune the PR controller by exploiting this equivalence. In particular, it is possible to demonstrate that the gains of the PR regulator can be obtained from those of the PI controllers mentioned above, whose gain values are divided by two.

The integrator of the PI guarantee zero steady-state error, but it also introduces a delay of 90 degrees. This delay is partially compensated by the zero of the PI regulator, which can be placed in cancellation of the pole of the decoupling inductance, i.e. the plant. The only remaining degree of freedom is the integral gain, which can be increased until the phase margin of the open loop transfer function reaches 75 degrees.

This tuning procedure leads to the values for the proportional and integral gains of the equivalent PI controllers, which (divided by two) give the required value for PR regulator

$$K_p = 5.2\Omega, \tag{2.16}$$

$$K_i = 56.5\Omega / s. \tag{2.17}$$

Fig 2.7 (a) and (b) show the Bode diagrams of the transfer function in open loop and in closed loop respectively, with the designed regulator, while in Fig 2.7 the step response of the system is shown.

It is now possible to tune the PI regulator of the DC-link. Let us call ω_C the cutting

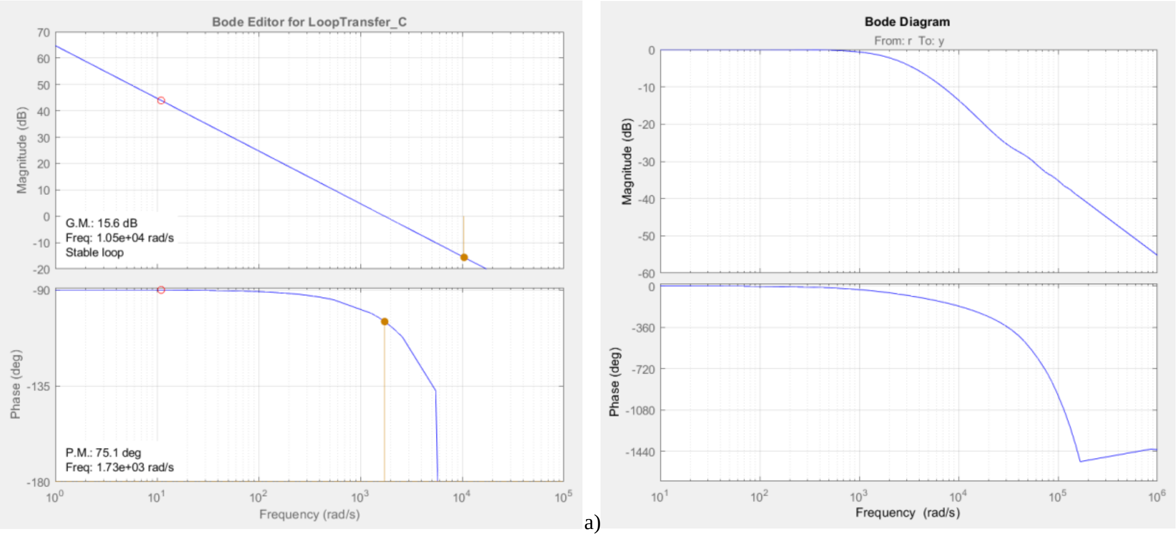

a) b)

Fig 2.6 Bode diagrams of the current open loop a) and the current closed loop b).

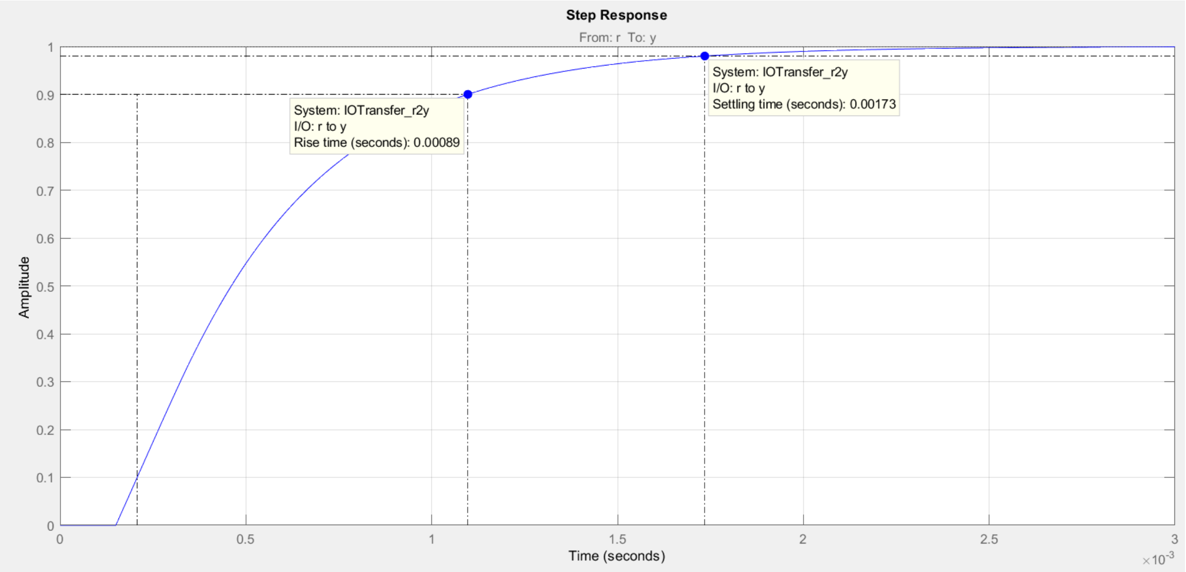

Fig 2.7 Step response of the current closed loop.

frequency of the current loop previously tuned, which is equal to 1730 rad/s.

The transfer function of the closed current loop can be written as

$$G_{curr} = \frac{1}{1+\dfrac{s}{\omega_c}} G_{INV} \,. \tag{2.18}$$

With reference to Fig 2.9, the transfer function of the voltage open loop can be expressed as follow:

$$G_{E_F} = PI * G_{curr} * G_{DC} \,, \tag{2.19}$$

where G_{DC} is given by (1.19).

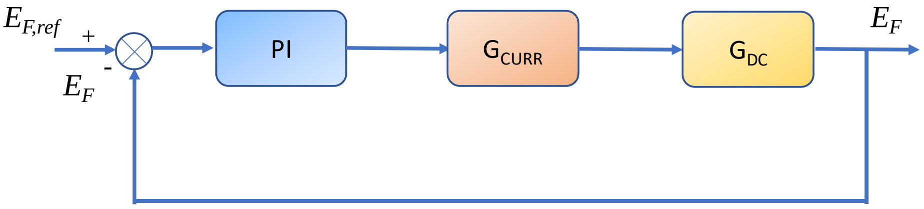

Fig 2.9 DC-link voltage loop.

With the same procedure used for the tuning of controller R_1, the zero of this PI regulator is placed in cancellation of the pole in (1.19) and the gain increased to a value that guarantees a phase margin higher than 75 degrees. Fig. 2.8 (a) e (b) show the Bode diagrams of the transfer function in open loop and in closed loop respectively, and the step response of the system in Fig. 2.10.

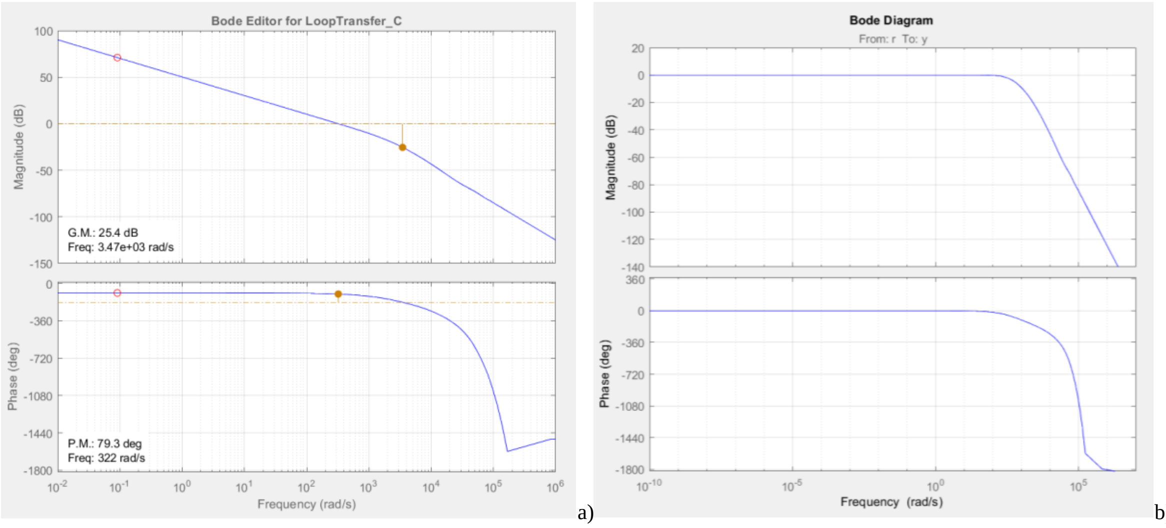

a) b)

Fig. 2.8 Bode diagrams of the voltage open loop a) and the voltage closed loop b).

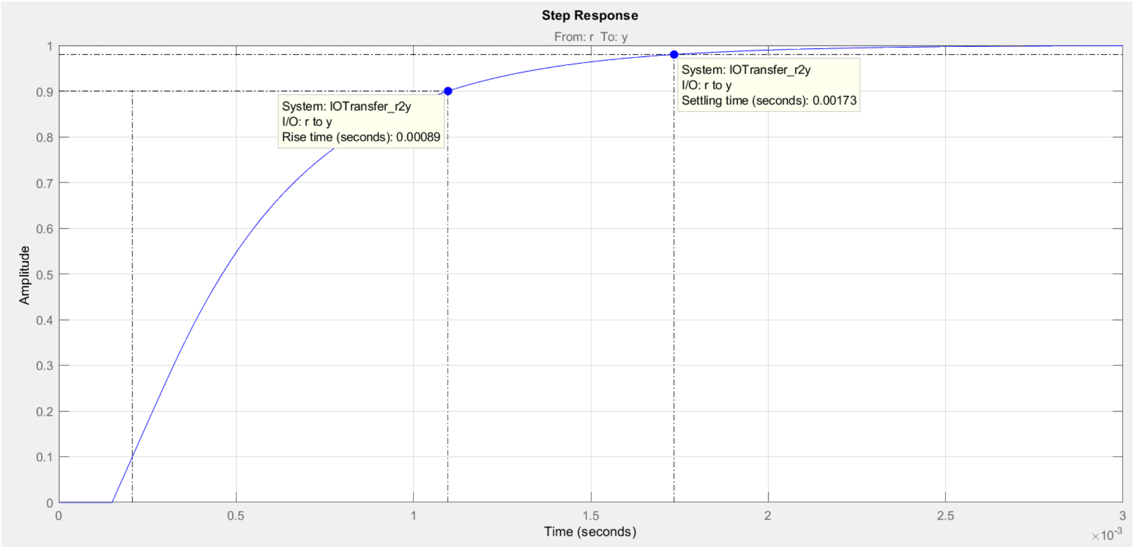

Fig. 2.10 Step response of the current closed loop.

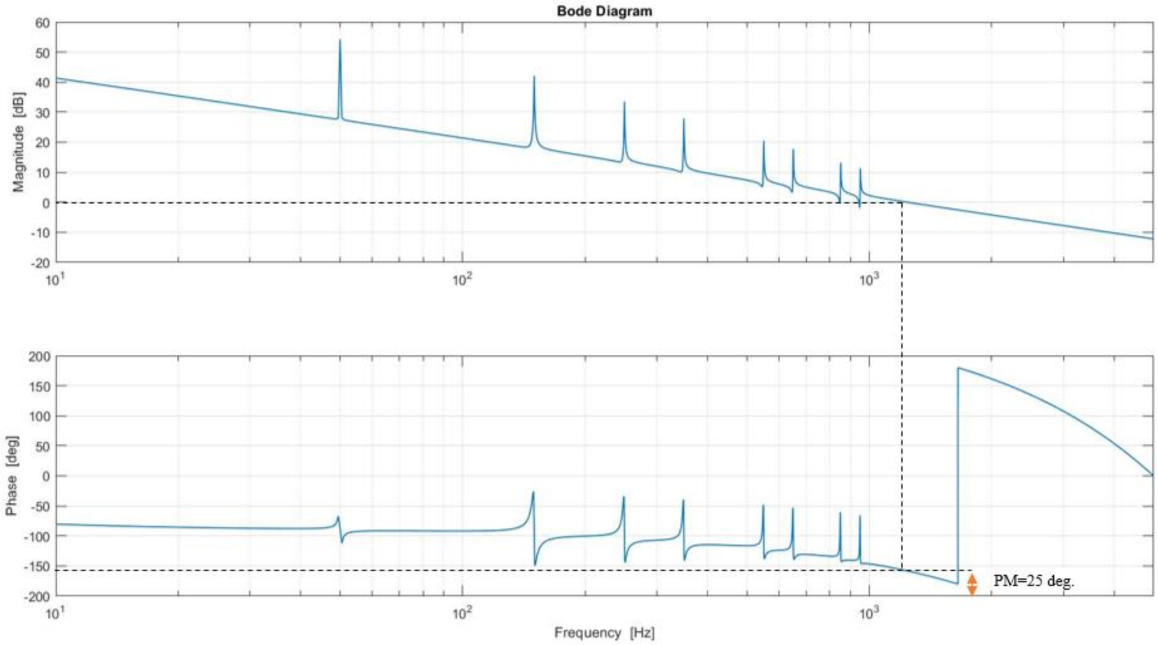

Fig. 2.11 Bode diagrams of the magnitude and phase of the open loop transfer function of the current

The study of the stability and tuning of multi-resonant controllers are open topics, given the complexity of these regulators. The choice of the proportional gain K_p is made in such a way as to have a phase margin that guarantees stability; the optimal number N of delay periods is experimentally found to be equal to 2 [15]; the integral K_i gain and damping δ have been chosen in such a way as to have a fair compromise between dynamic response and selectivity.

Theoretically the harmonics taken into consideration should be the odd ones until the 19th that are not multiple of three, since the system has three wires. However, due to the presence of single-phase loads connected to the power grid, a third harmonic can be present, making therefore necessary the use of PR regulator for this frequency.

Fig. 2.11 shows the Bode diagrams of the magnitude and phase of the open loop transfer function of Fig 2.5 where the harmonic compensator is also included in this example, the phase margin is 25 degrees.

D. *Discretization of the Control System*

In analog systems the input and output signals are continuous functions of time and the mathematical relationships that bind the input to the output are of integral-differential type. The Laplace transform transforms these relations into rational algebraic equations. In order to obtain implementable expressions on a micro-processor, the transform Z is used, which allows to pass from the algebraic equations obtained with Laplace transform to numerical iterative equations. The discretization process is fundamental for a resonant regulator, due to the high gain it presents in a narrow band of frequencies. Several discrete-time implementations are possible, but some of these cause discrepancies in resonance peaks compared to what is expected. These inaccuracies can lead to significant performance losses, especially for high-frequency signals. In fact, many of the existing discretization techniques cause a pole shift. This fact translates into a deviation of the resonance frequency and consequently the achievement of a null error is not guaranteed. The error becomes more significant as the sampling period and the resonance frequency increase. Discretization also has an effect on zeros, modifying their distribution with respect to the continuous time transfer function and this has a direct effect on the stability of the system.

The conversion from the Laplace domain to that of the Z-transform can be obtained through the relationships shown in TABLE 1. In [16] an analysis of the performance of resonant controllers with the different discretization methods has been carried out, highlighting the ones with the best performances in terms of accuracy in the location of the resonant peaks matching of the zeros and poles.

TABLE 1 – DISCRETIZATION METHODS

Zero-order Hold	$X(z) = (1 - z^{-1}) Z\left\{L^{-1}\left(\frac{X(s)}{s}\right)\right\}$
First-order Hold	$X(z) = \frac{(z-1)^2}{2T_c} Z\left\{L^{-1}\left(\frac{X(s)}{s}\right)\right\}$
Forward Euler	$s = \frac{z-1}{T_c}$
Backward Euler	$s = \frac{z-1}{zT_c}$
Tustin	$s = \frac{z-1}{(z+1)}\frac{2}{T_c}$
Tustin con pre-warping	$s = \frac{z-1}{(z+1)}\frac{\omega_0}{\tan(\frac{\omega_0 T_c}{2})}$
Zero-Pole matching	$z = e^{sT_c}$
Impulse invariant	$X(z) = Z\left\{L^{-1}\left(\frac{X(s)}{s}\right)\right\}$

In this PhD work, among those methods, the one called Tustin with pre-warping has been chosen.

E. *Experimental Results*

Experimental results have been carried out with a laboratory prototype of a shunt APF, which is used to compensate the highly distorted current produced by a diode bridge feeding a RC impedance, connected to the power grid through a filter inductance. The control system is implemented on a dSpace DS1104 platform and compensates up to the 19th harmonic component of the grid currents. The switching frequency is 10 kHz and the parameters of the experimental system are described in Table 2.

TABLE 2 – SYSTEM PARAMETERS

E_F	=	200	V_{DC}	R_F	=	50	mΩ
$V_{F,max}$	=	115	V_{peak}	L_F	=	2.36	mH
$I_{F,max}$	=	10	A_{peak}	C_L	=	0.6	mF
ω	=	2π 50	rad/s	R_L	=	60	Ω
C_F	=	2.2	mF	L_L	=	2.36	mH

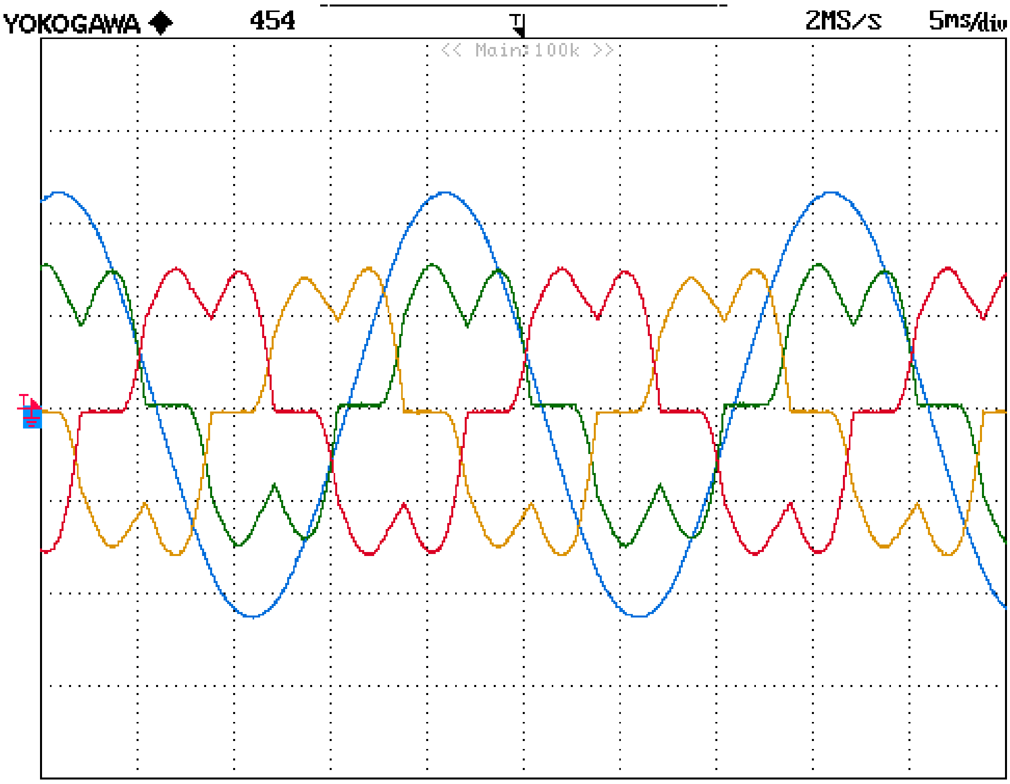

Fig. 2.12 Waveform of the grid currents and fundamental component of the phase voltage when the APF is off. Scale: current (2 A/div), voltage (40 V/div)

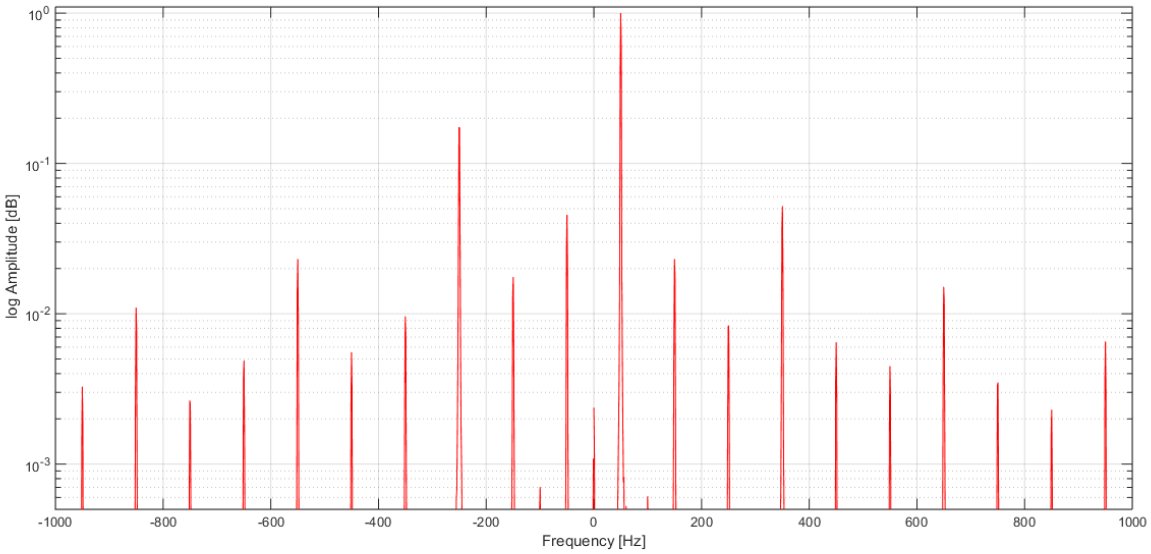

Fig. 2.14 Normalized spectrum of the grid currents when the APF is off.

Without any compensation, the currents absorbed by the passive load are the ones shown in Fig. 2.12. The phase delay of the phase current and the phase voltage is due to the decoupling inductance through which the distorting load is connected to the grid. The perfect sinusoidal waveform of the phase voltage is due to a software filter that extracts the fundamental component used for the synchronization of the PLL.

In Fig. 2.14 the spectrum of the grid current of Fig. 2.12 is shown in semi-logarithmic scale and normalized to the fundamental component. This spectrum is evaluated over a 1kHz band, which is wide enough to assess the most prominent current harmonics. The highest current harmonics are the fifth harmonic of the inverse sequence and the seventh harmonic of the direct sequence. Also, it can be noticed that a first inverse harmonic as well as a third direct harmonic are present. They are caused by the imbalance of the three currents of network. For this harmonic spectrum, the THDI is 21,56%.

As the APF turns on the DC-link control loop brings the voltage of the floating capacitor from the phase-to-phase peak voltage of 150 V to the reference value of 200 V as shown in Fig. 2.13.

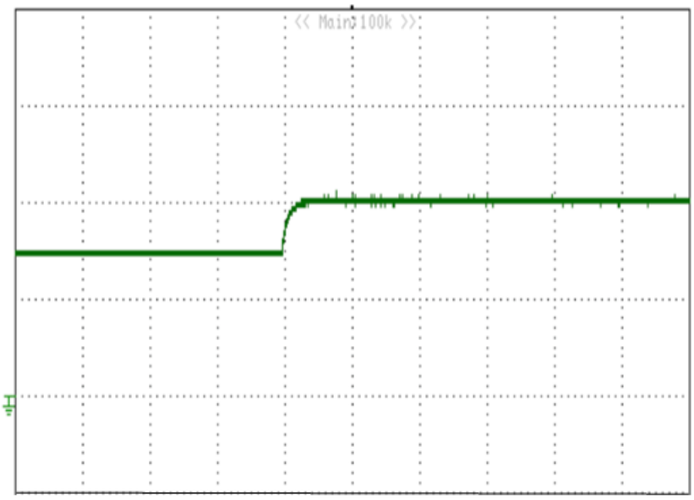

Fig. 2.13 Transient of the floating bridge voltage to the reference value. Scale: voltage (100 V/div)

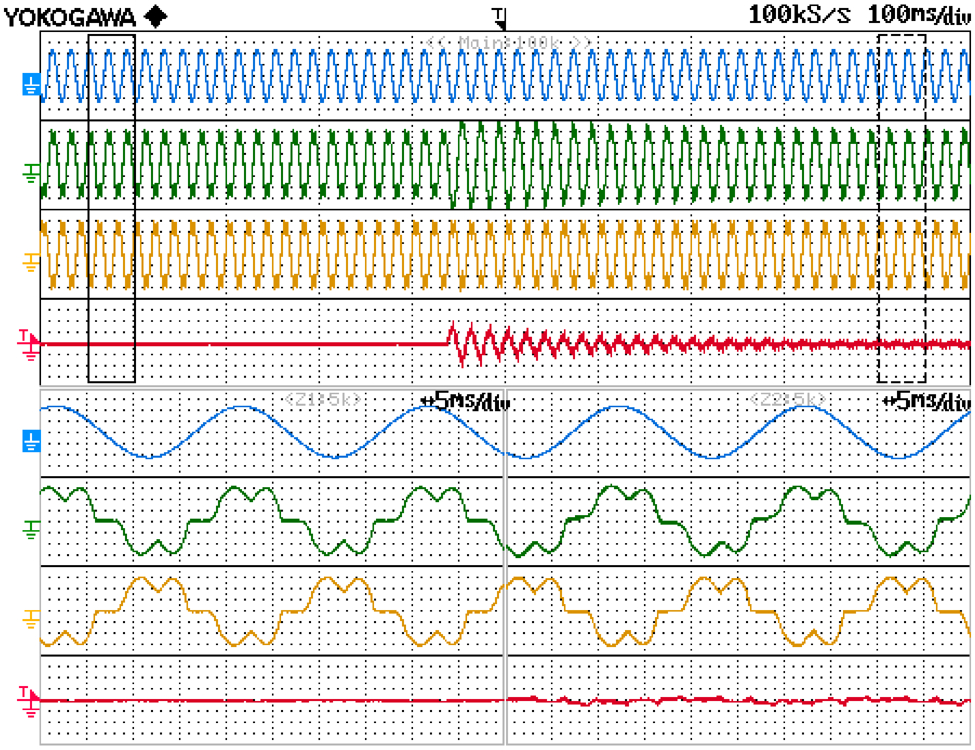

Fig. 2.15 Transient due to the charge of the DC-link of the power grid phase voltage and current, load current and filter current. Scale: current (2 A/div), voltage (40 V/div)

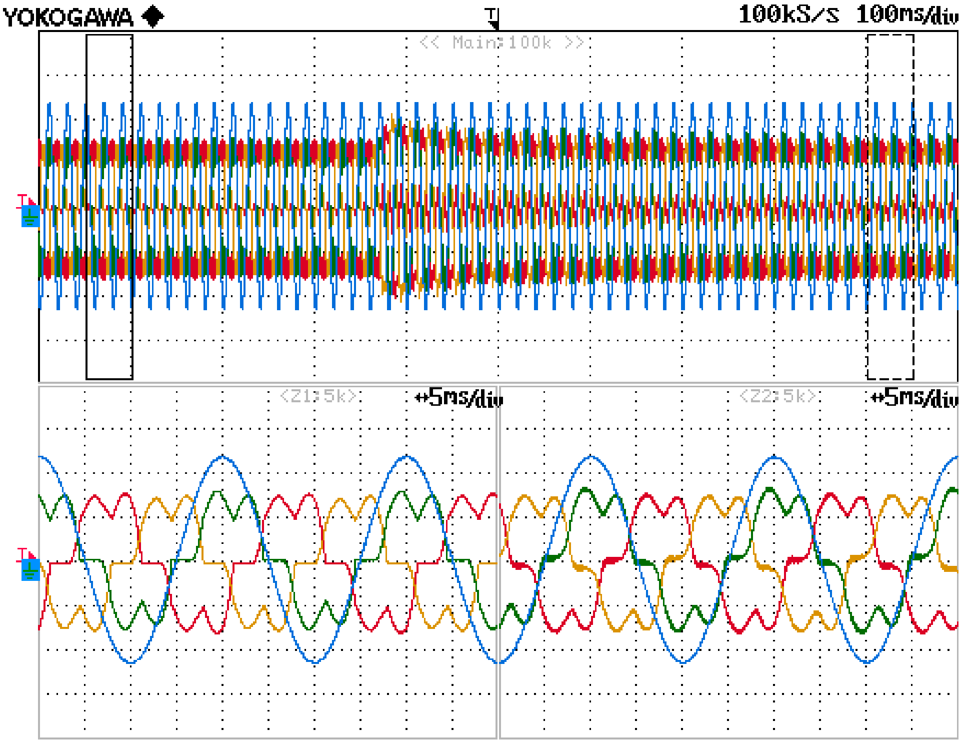

Fig. 2.16 Transient of the power grid currents due to the charge of the DC-link. Scale: current (2 A/div), voltage (40 V/div)

Fig. 2.15 shows the transient of the grid voltage and current, load current and filter current due to the charge of the DC-link. The PI controller that regulates the floating capacitor voltage provides the reference value for the d-component of the filter current. The resonant controller at the fundamental frequency tracks the reference value of the current, which causes an increase in the active power absorbed by the APF in order to increase its DC-link voltage, hence an increase in the current coming from the power grid. In Fig. 2.16 the same transient is shown and the behavior of the power grid current is highlighted.

Fig. 2.17 shows transient of the power grid phase voltage and current, load current and filter current due to the activation of the harmonic compensation.

In Fig. 2.18 the steady-state waveform of the power grid currents is shown and their harmonic spectrum is represented in Fig. 2.19. The THD of the power grid currents when the APF is tuned on drops to the value of 2,60%, proving therefore the good performance of the developed control system.

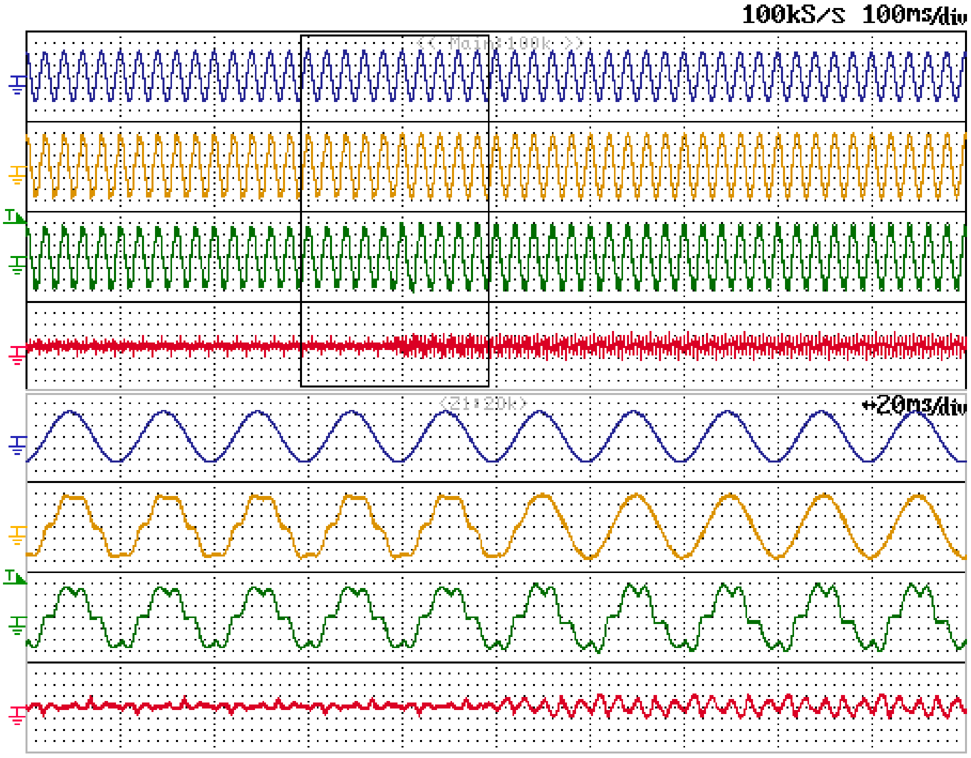

Fig. 2.17 Transient of the power grid phase voltage and current, load current and filter current due to the activation of the harmonic compensation. Scale: current (2 A/div), voltage (40 V/div)

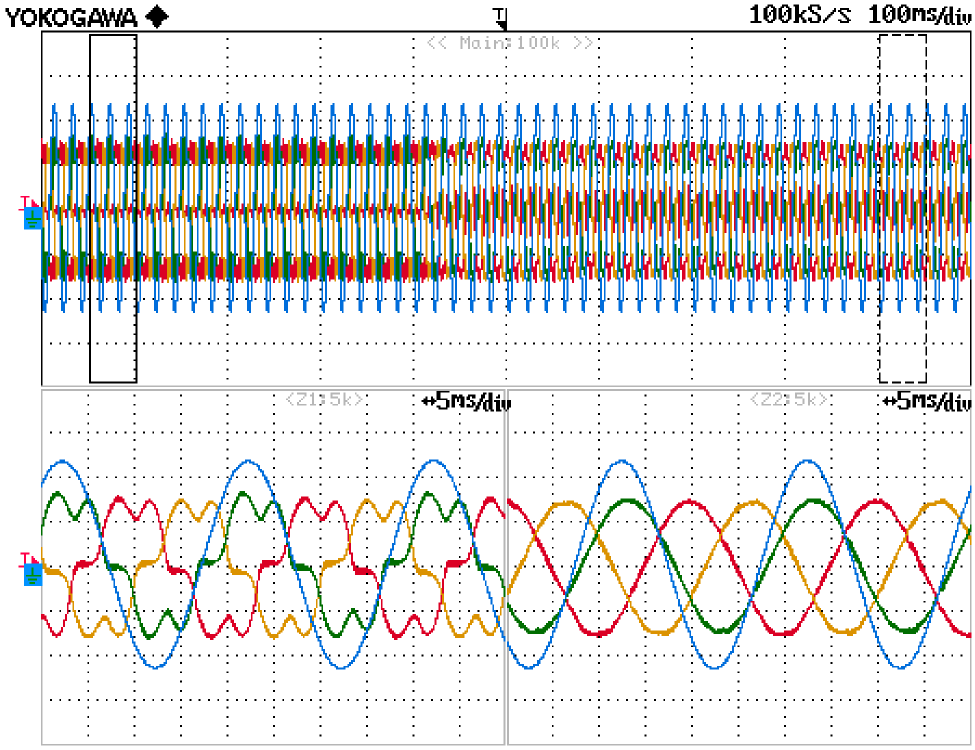

Fig. 2.18 Power grid currents before and after the harmonic compensation of the APF. Scale: current (2 A/div), voltage (40 V/div)

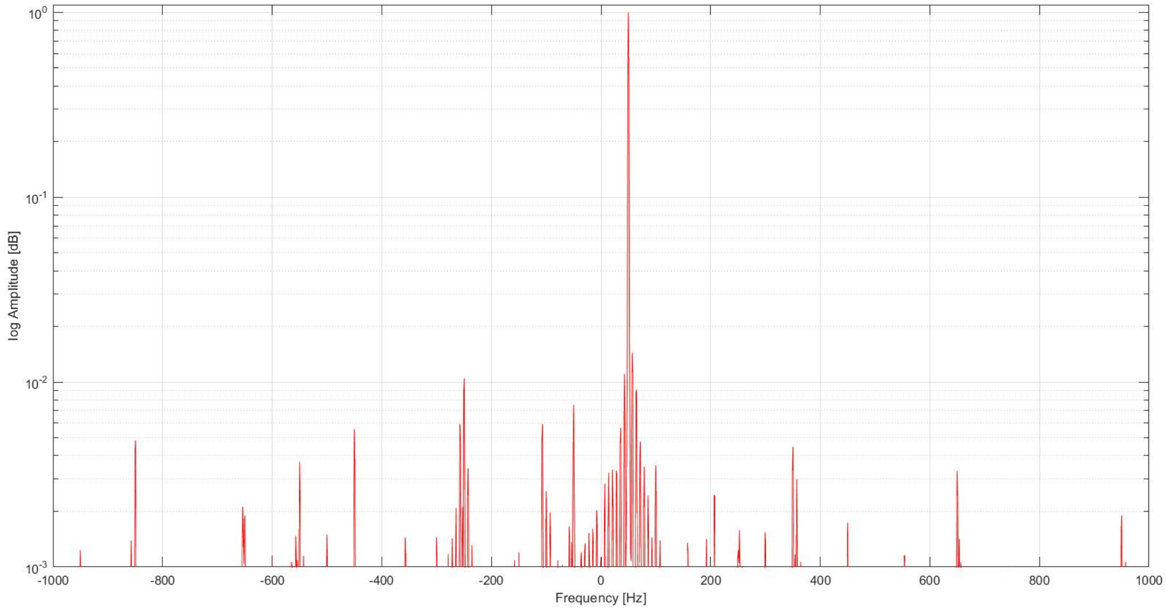

Fig. 2.19 Normalized spectrum of the grid currents when the APF is on.

It is possible to notice in Fig. 2.18 that there is a delay of the power grid current to the power grid phase voltage. It is possible to compensate the reactive power of the grid by acting on the q-component of the filter current at the fundamental frequency. The results of the reactive power compensation are shown in Fig. 2.20.

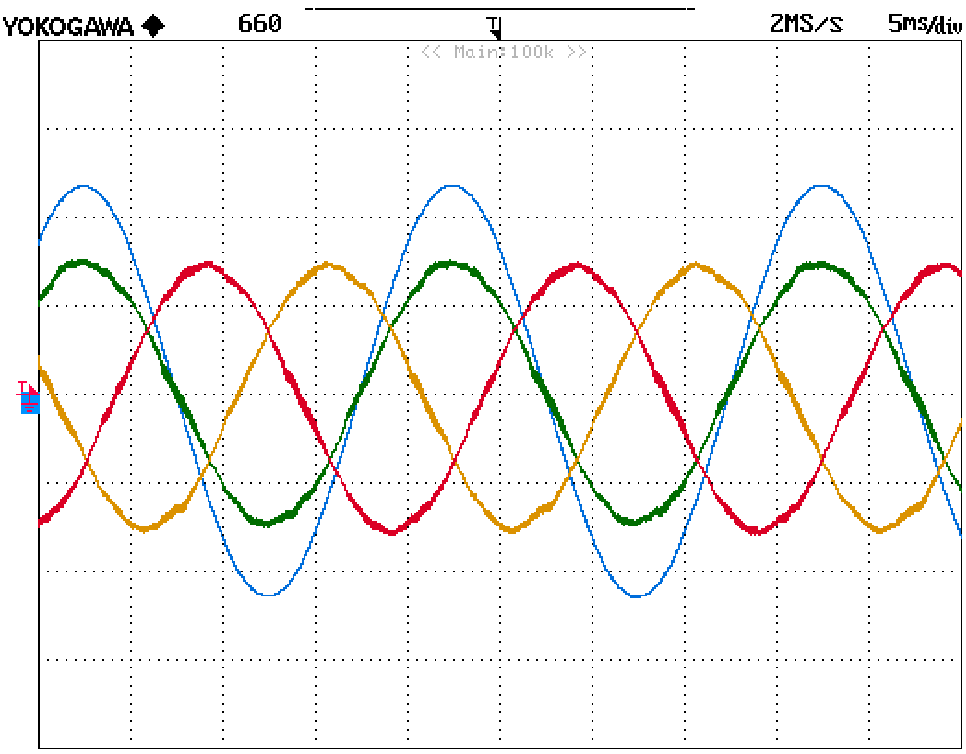

Fig. 2.20 Reactive power compensation of the power grid through the APF. Scale: current (2 A/div), voltage (40 V/div)

2.2 REPETITIVE CONTROLLER

A. Relation between Resonant Controller and Repetitive Controller

The relation between resonant and repetitive controllers (RCs) has been object of study in the literature of the last decade [17]- [18]. Both are based on the Internal Model Principle (IPM), which affirms that a sufficient condition for the asymptotic tracking of the reference signal is that the transfer function obtained by merging the controller and the controlled plant contains the generating polynomial of the reference signal in the denominator.

Let us then consider a sinusoidal reference signal with angular frequency equal to $k\omega_0$, where ω_0 is considered as fundamental component and k represents the harmonic order, written in the Laplace domain:

$$I_{ref}(s) = L\left[\cos\left(k\omega_0 t\right)\right] = \frac{s}{s^2 + \left(k\omega_0\right)^2} \tag{2.20}$$

which is equal to the transfer function of a resonant controller with frequency $k\omega_0$. Thanks to the IPM, the resonant controller at $k\omega_0$ is able to track a sinusoidal signal at that frequency. If the reference signal is composed by the sum of N sinusoidal signals at multiple frequency of the fundamental one,

$$I_{ref}(t) = \sum_{k=0}^{N} \cos\left(k\omega_0 t\right) \tag{2.21}$$

then the controller able to track it, has to have the sum of N resonant controllers, one for each sinusoidal signal that contributes to the reference signal, as follow:

$$K_i \sum_{k=0}^{N} \frac{s}{s^2 + \left(k\omega_0\right)^2}\,. \tag{2.22}$$

If the number N of resonant controllers summed up in (2.22) tends to infinite, for the properties of the exponential functions, it can be written:

$$K_i \sum_{k=0}^{\infty} \frac{s}{s^2 + \left(k\omega_0\right)^2} = K_i \frac{\pi}{\omega_0} \left(\frac{e^{s\frac{\pi}{\omega_0}} + e^{-s\frac{\pi}{\omega_0}}}{e^{s\frac{\pi}{\omega_0}} - e^{-s\frac{\pi}{\omega_0}}} \right) \tag{2.23}$$

which, with few mathematical steps and by neglecting for the moment the gain in front of the transfer function, can be written as follow:

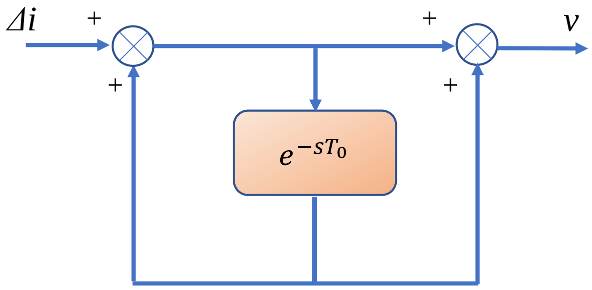

Fig 2.21. Repetitive control scheme.

$$G_{RC} = \frac{1+e^{-sT_0}}{1-e^{-sT_0}} . \tag{2.24}$$

The (2.24) represents the transfer function of a repetitive controller, whose control scheme is shown in Fig 2.21.

It sums to the input reference, the same signal delayed of a period *T₀*. This cause an infinite number of resonances at multiple frequencies of the fundamental one $f_0 = 1/T_0$, as can be found by nullifying the denominator of (2.24):

$$\begin{aligned} &1-e^{-sT_0} = 1-e^{-j\omega T_0} = 1-\cos(\omega T_0) + j\sin(\omega T_0) = 0 \Rightarrow \\ &\Rightarrow \omega T_0 = 2k\pi \Rightarrow f_{res} = kf_0 \qquad k \in \mathbb{Z} \end{aligned} \tag{2.25}$$

(2.25) confirms hence that the repetitive controller is equivalent to a sum of infinite resonant controllers. These resonances, obtained by buffering the reference input signal, imply a lower computational burden compared with the resonant controllers, but it requires a memory effort in order to store a whole period of the input signal.

The feedforward contribute instead, causes an infinite number of zeroes in (2.24), located in between the resonance frequencies, as shown in (2.26).

$$\begin{aligned} &1+e^{-sT_0} \xrightarrow{s=j\omega} 1+e^{-j\omega T_0} = 1+\cos(\omega T_0) - j\sin(\omega T_0) = 0 \Rightarrow \\ &\Rightarrow \omega T_0 = (2k+1)\pi \Rightarrow f_{zeros} = \left(k+\frac{1}{2}\right) f_0, \qquad k \in \mathbb{Z}, \end{aligned} \tag{2.26}$$

The Bode diagrams of the magnitude and phase for the transfer function (2.24), are represented in Fig. 2.22.

A simpler version of repetitive control can be obtained if the control scheme shown in Fig 2.21 is modified by cutting away the feedforward path as shown in Fig. 2.23(a).

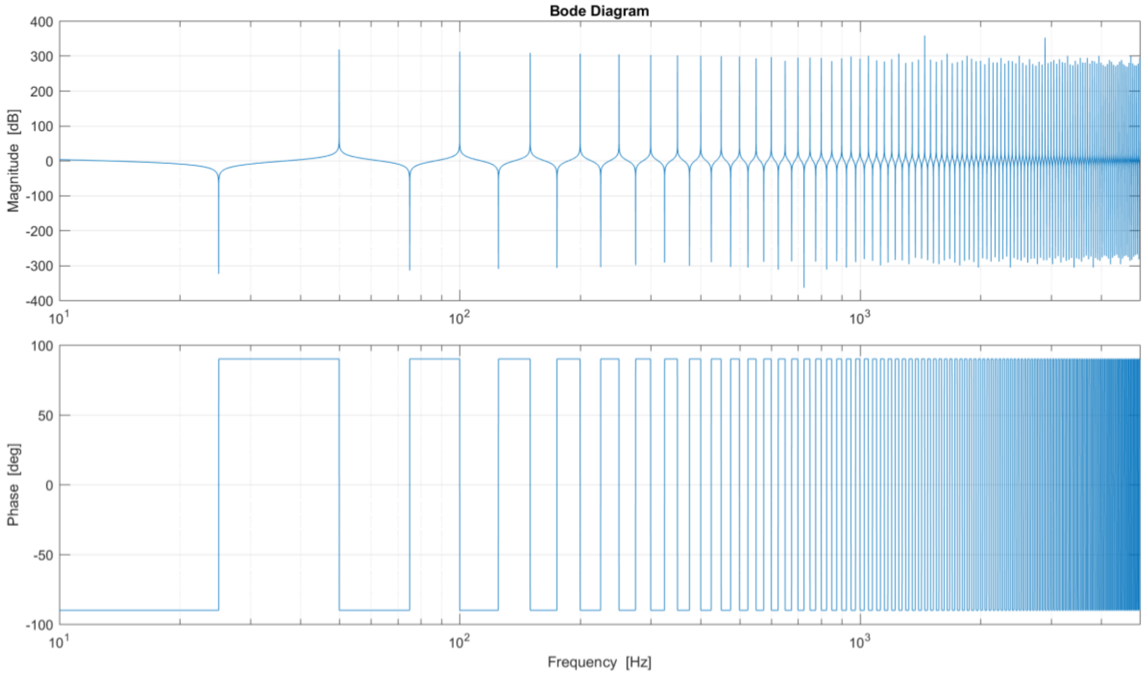

Fig. 2.22 Bode diagrams of the repetitive controller base scheme.

As already said during the study of the resonant controller, it is necessary to take into account the delay introduced by the process of discretization and compensate it with a phase lead. If T_d represents this phase delay, the scheme Fig. 2.23(a) can be modified as shown in Fig. 2.23(b), which transfer function can be found with the following mathematical steps:

$$v=\left(\Delta i+ve^{-sT_d}\right)e^{-s(T_0-T_d)}=\frac{e^{-s(T_0-T_d)}}{1-e^{-sT_0}}\Delta i=\frac{e^{-sT_0}}{1-e^{-sT_0}}e^{sT_d}\Delta i\Rightarrow \tag{2.27}$$

$$\Rightarrow G_{FHRC}^{(1)}=\frac{e^{-sT_0}}{1-e^{-sT_0}}e^{sT_d}\,. \tag{2.28}$$

The transfer function (2.28) still presents the same resonance frequencies of (2.24), ensuring the harmonics tracking, and the delay on the direct path allows one to achieve also a phase lead, which is causal as long as $T_d < T_0$.

This topology will be indicated with the superscript $^{(1)}$ hereafter, while the subscript

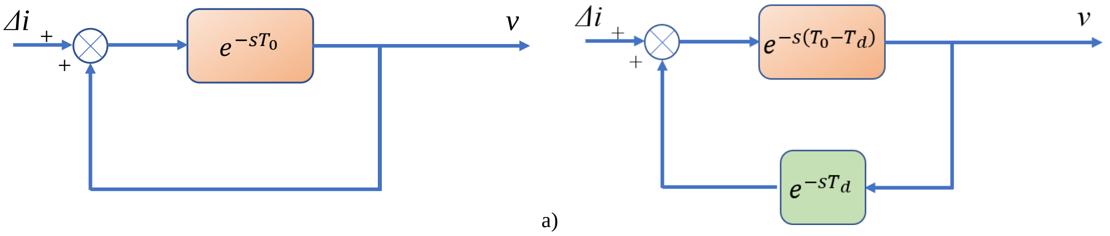

a)

b)

Fig. 2.23 Base scheme of a repetitive controller a) and base scheme with the phase lead b

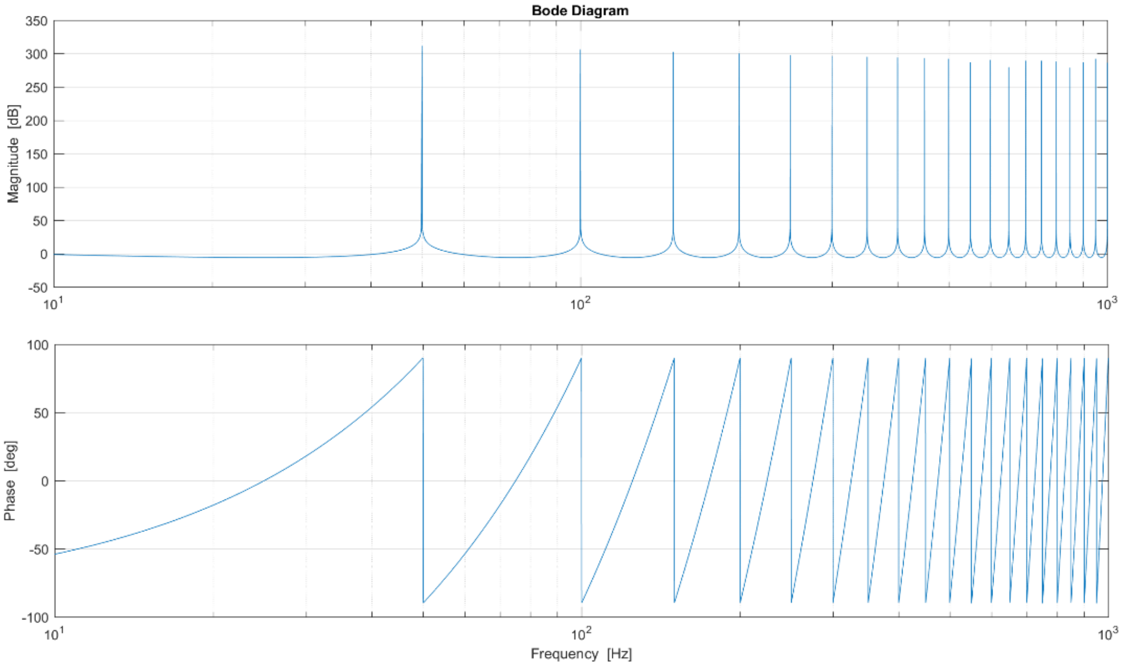

Fig. 2.24 Bode diagrams of the base scheme transfer function $G_{FHRC}^{(1)}$.

(FHRC) stands for "Full Harmonic Repetitive Controller" and will be used for those configurations that presents resonance frequencies for all the multiple frequencies of the fundamental one.

The Bode diagrams of magnitude and phase for the transfer function in (2.28) are shown in Fig. 2.24.

Taking into account the delay compensation of T_d for the control scheme of Fig 2.21 is not as easy as for the topology 1, due to the fact that the delayed period T_0 is not on the direct path.

The phase lead has been achieved by adding a further period delay from which the phase lead is obtained. The term is represented by the function $e^{-s(T_0-T_d)}$ in the control scheme of

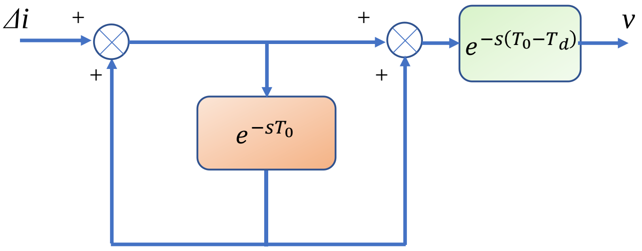

Fig 2.25. Repetitive control scheme – Topology 2, FHRC.

Fig 2.25. The transfer function modifies as follow:

$$G_{FHRC}^{(2)} = k_s \frac{1+e^{-sT_0}}{1-e^{-sT_0}} e^{-s(T_0-T_d)} . \tag{2.29}$$

B. *Stabilization of the Repetitive Control*

The high gain over a wide frequency band affects the system stability. Several solutions have been investigated in order to stabilize this kind of controllers. An interesting solution has been developed in [19], where a low pass filter with zero-phase shift has been used to reduce the contribution at high frequency of the repetitive controller. The general expression of a zero-phase filter can be written as follow:

$$Q(s) = \sum_{n=1}^{n_{\lim}} C_n e^{-sn\tau} + C_0 + \sum_{n=1}^{n_{\lim}} C_n e^{sn\tau} , \tag{2.30}$$

Whose first order approximation is:

$$\begin{aligned} Q(s) &= \sum_{n=1}^{n_{\lim}} C_n e^{-sn\tau} + C_0 + \sum_{n=1}^{n_{\lim}} C_n e^{sn\tau} \simeq C_1 e^{-s\tau} + C_0 + C_1 e^{s\tau} = \\ &= 2C_1 \frac{e^{-s\tau}+e^{s\tau}}{2} = 2C_1 \cosh\left(s\tau\right) + C_0 \end{aligned} \tag{2.31}$$

The values for the coefficients C1 and C0 can be found by writing (2.31) in the domain of the angular frequency ω,

$$Q(\omega) = 2C_1 \cosh\left(j\omega\tau\right) + C_0 = 2C_1 \cos\left(\omega\tau\right) + C_0 \quad . \tag{2.32}$$

In order to have $0 \le Q\left(\omega\right) \le 1$, the constraint of the coefficient becomes:

$$0 \le C_0 + 2C_1 \le 1 \tag{2.33}$$

Equation (2.32) represents a real number, which behaves as a moving average low-pass filter variable with the frequency. Its magnitude has a minimum for $\omega\tau = \pi$. The frequency of this minimum can be found as:

$$f_{\min} = \frac{1}{2\tau} . \tag{2.34}$$

Choosing τ = T_s, where T_s represents the sampling period, sets the system Shannon frequency as the frequency for which the filter has a minimum, obtaining a decreasing trend in the whole system band. In Fig 2.27 the trend of the gain of the filter is shown when its

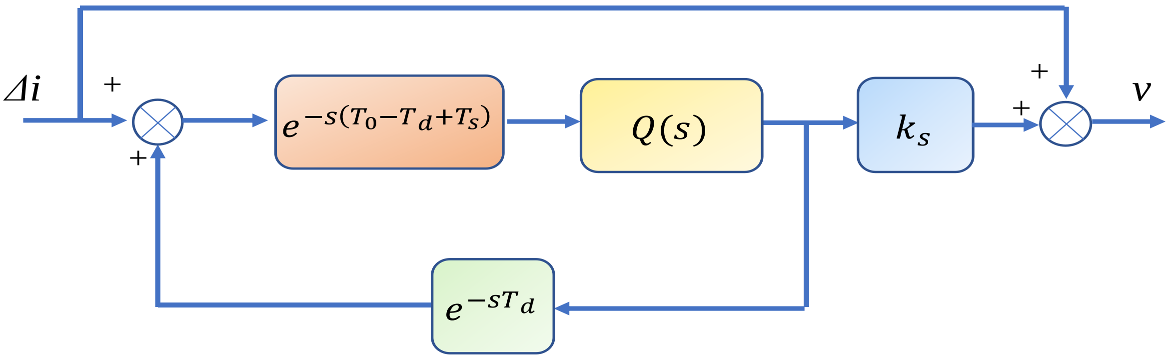

Fig 2.26. Repetitive control scheme implemented – Topology 1, FHRC.

coefficients vary; the sampling frequency has been assumed to be 10 kHz, so the trend of the module up to 5 kHz is shown.

The cut-off frequency decreases as C_1 increases. It is important to design this filter with a cut-off frequency above 1 kHz, where the harmonics of interest are, in order to not interfere with the current controller. The filter *Q(s)* strongly reduces high frequencies disturbances, which may be harmful and cause of instability.

However, this filter topology is not implementable due to the lead phase term $C_1\, e^{s\tau}$ in its transfer function. Nevertheless, once again, it is possible to compensate the phase lead required by the filter by including it in the direct path, where it is multiplied by a delay operator. It is possible to write:

$$Q'(s) = Q(s)e^{-sT_s} = \left(C_1 e^{-sT_s} + C_0 + C_1 e^{sT_s}\right)e^{-sT_s} = C_1 e^{-s2T_s} + C_0 e^{sT_s} + C_1, \tag{2.35}$$

$$Q'(s)e^{-sT_0} = Q(s)e^{-s(T_0+T_s)}. \tag{2.36}$$

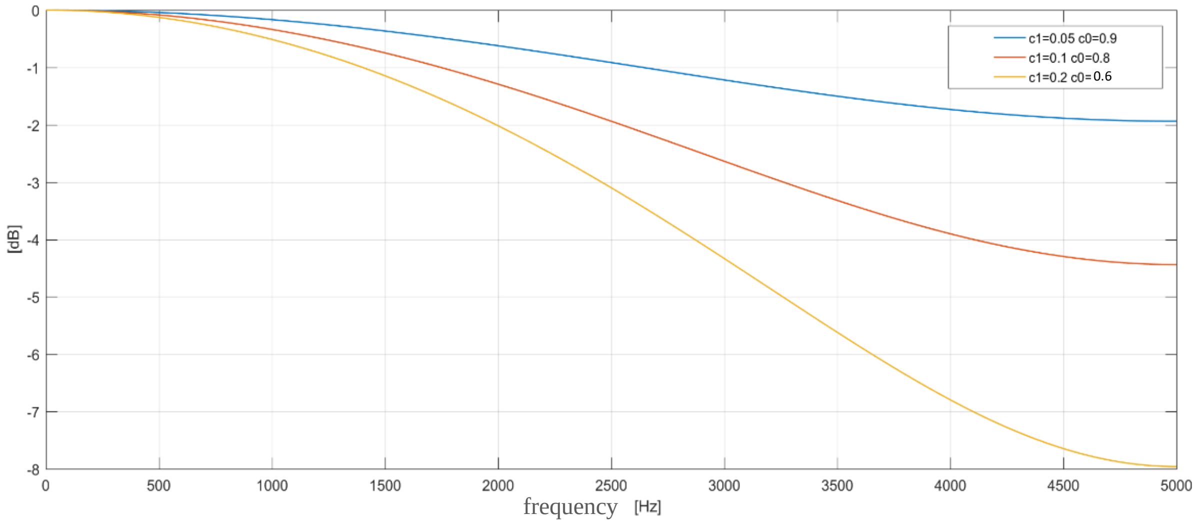

Fig 2.27. Bode diagram of the magnitude of the average moving low pass filter

The control scheme of the repetitive controller of Fig. 2.23(b) can be implemented as shown in Fig 2.26. Its transfer function is:

$$G^{(1)}_{FHRC,plug-in} = k_s \frac{Q(s)e^{-s(T_0+T_s)}}{1-Q(s)e^{-s(T_0+T_s)}} e^{sT_d} + 1 = 1 + G^{(1)}_{FHRC} \cdot \qquad (2.37)$$

In addition to the filter Q(s), a series gain k_S has also been added. It is used to increase the controller gain overall the bandwidth.

A "plug-in" path is added to control scheme of Fig 2.26. It sums the input error to the repetitive output and allows one to define a regulation loop that does not include the controller. This feature will helpful in the mathematical steps for the tuning of the series gain k_S.

Likewise (2.28), the repetitive controller $G^{(1)}_{FHRC}$ contains resonance frequencies for all the multiple harmonics of the fundamental one.

The tuning of the series gain k_S is accomplished by studying the stability of the closed-loop (2.38), shown in Fig 2.28.

$$G_{current,cl} = \frac{\left(1+G^{(1)}_{FHRC}\right)G_{INV}G_{PLANT}}{1+\left(1+G^{(1)}_{FHRC}\right)G_{INV}G_{PLANT}} = \frac{\left(1-e^{-s(T_0-T_d)}Q(s)\left(1-k_s e^{sT_d}\right)\right)G(s)}{1-e^{-s(T_0-T_d)}Q(s)\left(1-k_s e^{sT_d}G(s)\right)} \cdot \qquad (2.38)$$

According to [19], the current loop is stable if:

- the transfer function (2.39), considering $G^{(1)}_{FHRC} = 0$, is stable,

$$G = \frac{G_{INV}G_{PLANT}}{1+G_{INV}G_{PLANT}} \qquad (2.39)$$

- the denominator of (2.38) is not zero in the frequency band up to the Shannon

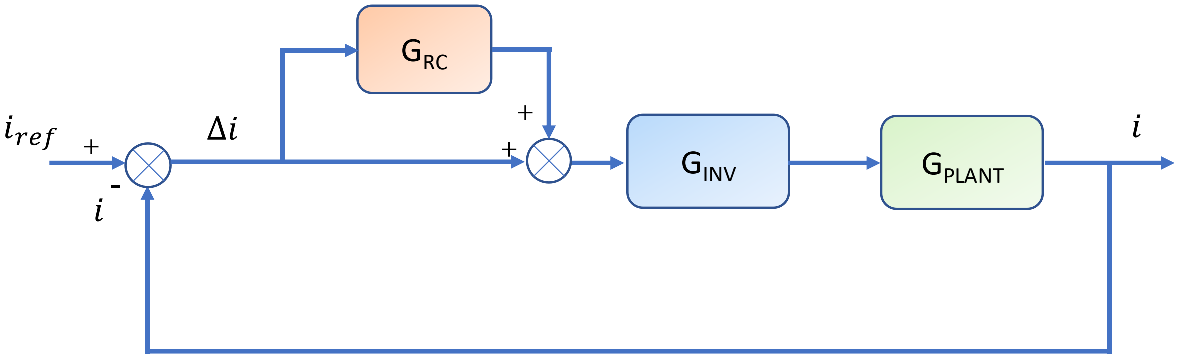

Fig 2.28. Current control loop.

frequency $\frac{f_s}{2}$,

$$\left| Q(s)\left(1-k_s e^{sT_d} G(s)\right) \right| < 1 . \tag{2.40}$$

By writing (2.40) in the frequency domain and Q and G in polar coordinates, the last condition becomes

$$\begin{aligned} &\left| \left|Q(\omega)\right| e^{j\vartheta_Q(\omega)} \left(1-k_s \left|G(\omega)\right| e^{j\left(\vartheta_G(\omega)+\omega T_d\right)}\right) \right| < 1 \Rightarrow \\ &\Rightarrow \left| \left(1-k_s \left|G(\omega)\right| e^{j\left(\vartheta_G(\omega)+\omega T_d\right)}\right) \right| < \frac{1}{\left|Q(\omega)\right|} \end{aligned} \tag{2.41}$$

By solving the last inequality, one finds the values of the series gain k_s that satisfy the stability condition,

$$0 < k_s < \frac{1-\left|Q(\omega)\right|^2}{\left|Q(\omega)\right|^2 k_s \left|G(\omega)\right|^2} + \frac{2\cos\left(\vartheta_G(\omega)+\omega T_d\right)}{\left|G(\omega)\right|} . \tag{2.42}$$

The last condition can be approximated since the first term of upper limit tends to zero in the frequency band of the regulator, becoming:

$$0 < k_s < \frac{2\cos\left(\vartheta_G(\omega)+\omega T_d\right)}{\left|G(\omega)\right|} . \tag{2.43}$$

It can be noticed that there are admissible values of k_s as long as $\left|\vartheta_G(\omega)+\omega T_d\right| < \frac{\pi}{2}$. It is then possible to choose the phase T_d in order to maximize the upper bound of the series gain.

In Fig 2.29 is shown the trend of the series gain k_s for different values of the phase lead

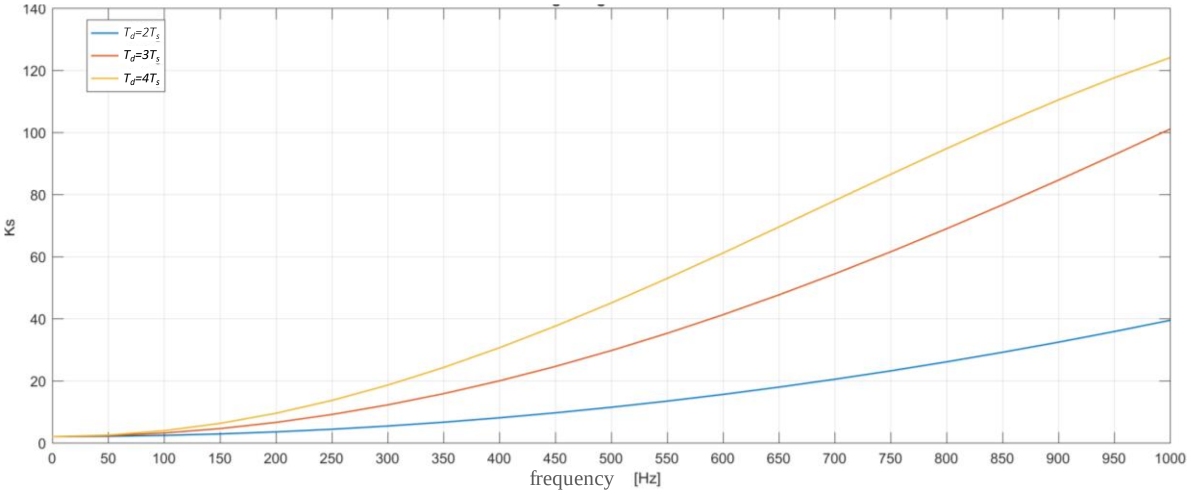

Fig 2.29. Trend of the series gain k_s for different value of the phase lead T_d.

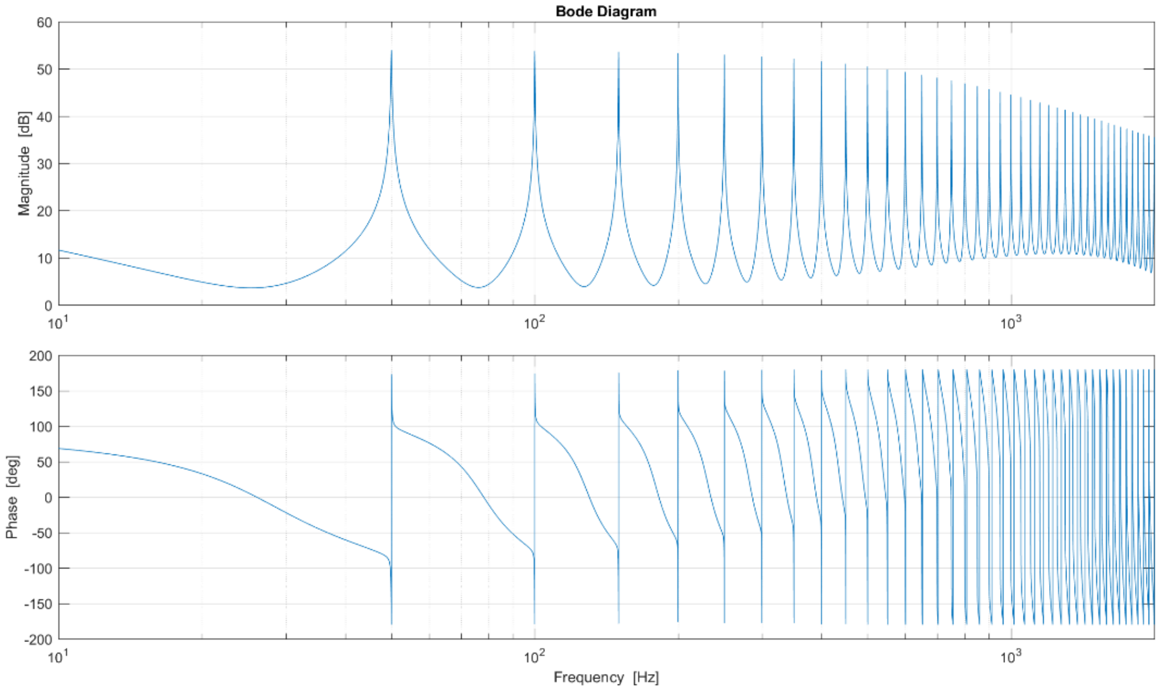

Fig. 2.30 Bode diagrams of the transfer function $G_{FHRC}^{(1)}$ stabilized.

T_d, which depends on the number of sample time that have to be compensated.

The Bode diagrams of magnitude and phase of $G_{FHRC}^{(1)}$ in (2.37) with the low-pass filter and the series gain so tuned become as shown in Fig. 2.30

Similar techniques are used to stabilize the topology of repetitive controller shown in Fig 2.25, which modifies as shown in Fig 2.31.

The transfer function for this control scheme becomes:

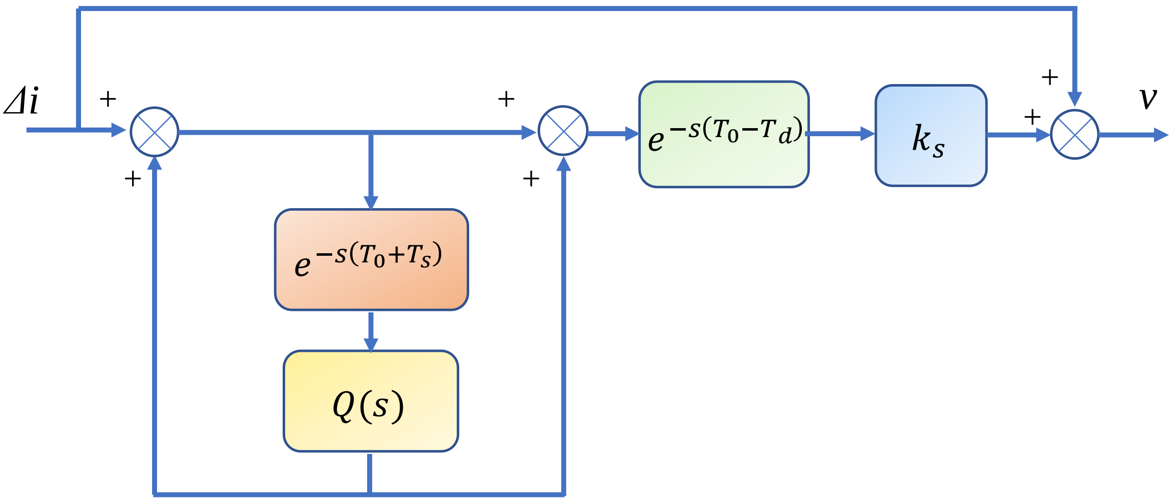

Fig 2.31. Repetitive control scheme implemented – Topology 2, FHRC.

$$G^{(2)}_{FHRC,\,plug-in}=k_s\frac{1+Q(s)e^{-s(T_0+T_s)}}{1-Q(s)e^{-s(T_0+T_s)}}e^{-s(T_0-T_d)}+1=1+G^{(2)}_{FHRC}\,. \tag{2.44}$$

The tuning of the gain series gives the following range of admissible values:

$$0<k_s<\frac{1-|Q(\omega)|^2}{|Q(\omega)|^2\,k_s\,|G(\omega)|^2}+\frac{2\cos(\vartheta_1(\omega))}{|G(\omega)|k^*}+\frac{2\cos(\vartheta_2(\omega))}{|G(\omega)|k^*|Q(\omega)|}\,. \tag{2.45}$$

where the parameters k^*, θ_1, θ_2 *and* θ_3 stand for:

$$k^*=\left(1+\frac{1}{|G(\omega)|}+\cos(\vartheta_Q(\omega))\left(1+\frac{1}{|Q(\omega)|}\right)+\left(\frac{1}{|Q(\omega)|}-1\right)\cos(\vartheta_3(\omega))\right), \tag{2.46}$$

$$\vartheta_1=\vartheta_G+\omega T_d\,, \tag{2.47}$$

$$\vartheta_2=\vartheta_G+\omega T_d-\vartheta_Q\,, \tag{2.48}$$

$$\vartheta_3=\vartheta_1+\vartheta_2\,. \tag{2.49}$$

The Bode diagrams of magnitude and phase of (2.44) are shown in Fig. 2.32.

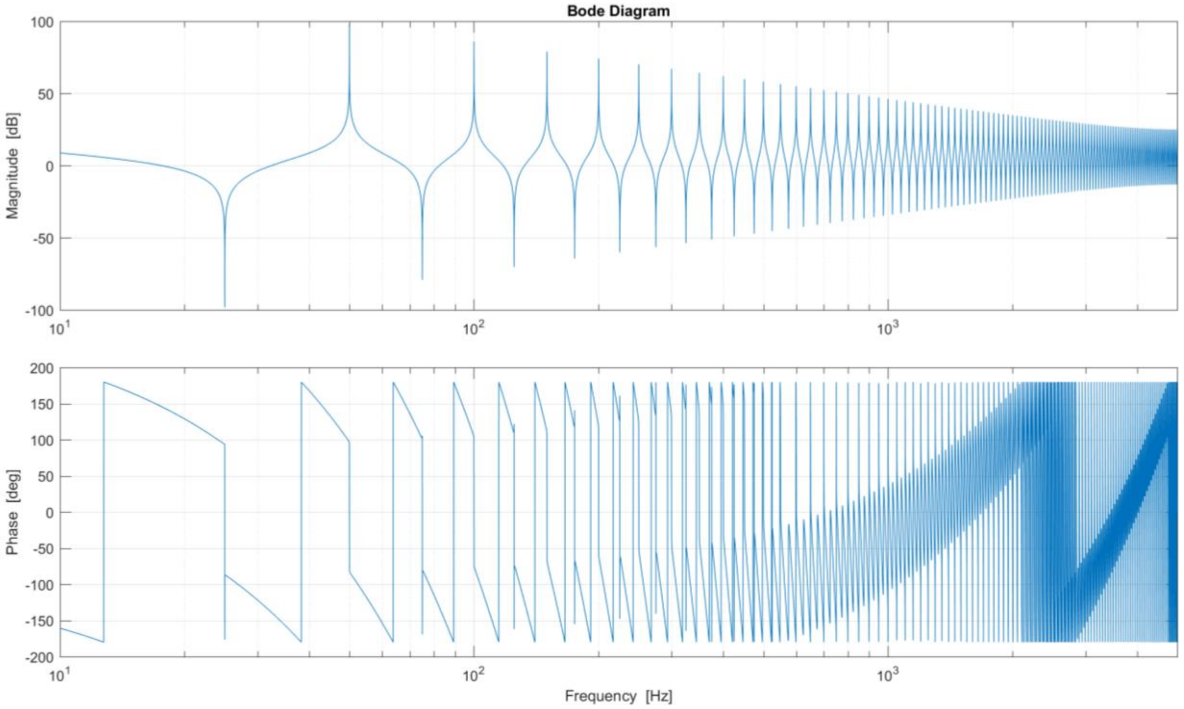

Fig. 2.32 Bode diagrams of the transfer function $G^{(2)}_{FHRC}$ stabilized.

C. *Odds Harmonic Repetitive Controller (ODRC)*

It is possible to change the set of resonance frequencies for both topologies shown, by acting on the sign of the feedback signal. The control scheme of Fig 2.26, modified as shown in Fig 2.33, has the following transfer function

$$G^{(1)}_{ODRC,plug-in} = -k_s \frac{Q(s)e^{-s\left(\frac{T_0}{2}+T_s\right)}}{1+Q(s)e^{-s\left(\frac{T_0}{2}+T_s\right)}} e^{sT_d} + 1 = 1 + G^{(1)}_{OHRC} \cdot \qquad (2.50)$$

The set of resonance frequencies can be found equating to zero the denominator of $G^{(1)}_{ODRC}$,

$$\begin{aligned} &1+e^{-j\omega\frac{T_0}{2}} = 1+\cos\left(\omega\frac{T_0}{2}\right) - j\sin\left(\omega\frac{T_0}{2}\right) = 0 \Rightarrow \\ &\Rightarrow \omega\frac{T_0}{2} = (2k+1)\pi \Rightarrow f_{res} = (2k+1)\, f_0, \qquad k \in \mathbb{Z}, \end{aligned} \qquad (2.51)$$

The resonance frequencies are located at the odd harmonics of the fundamental frequency *f₀*.

The Bode diagrams of $G^{(1)}_{ODRC}$, without considering the effects of *Q(s)* and k_s, are shown in Fig 2.33, while in Fig. 2.35 the same diagrams are shown after the stabilization procedure.

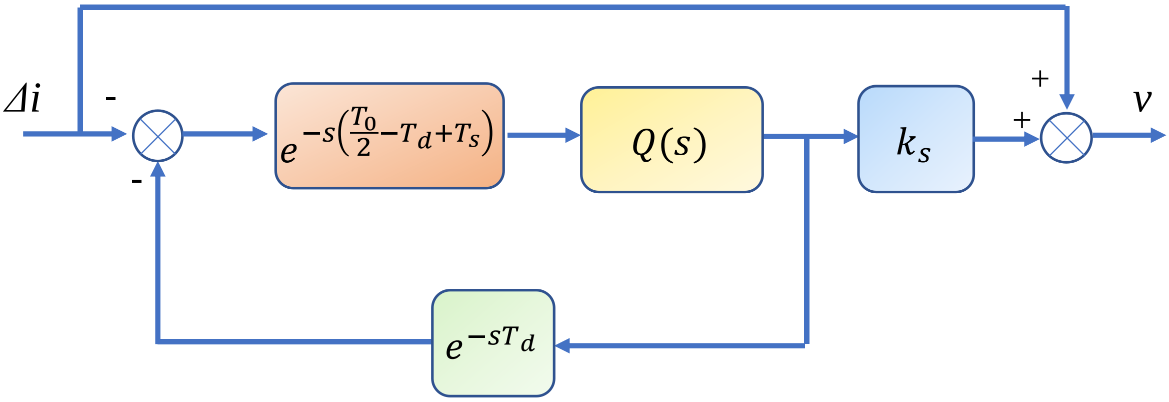

Fig 2.33. Repetitive control scheme implemented – Topology 1, ODRC.

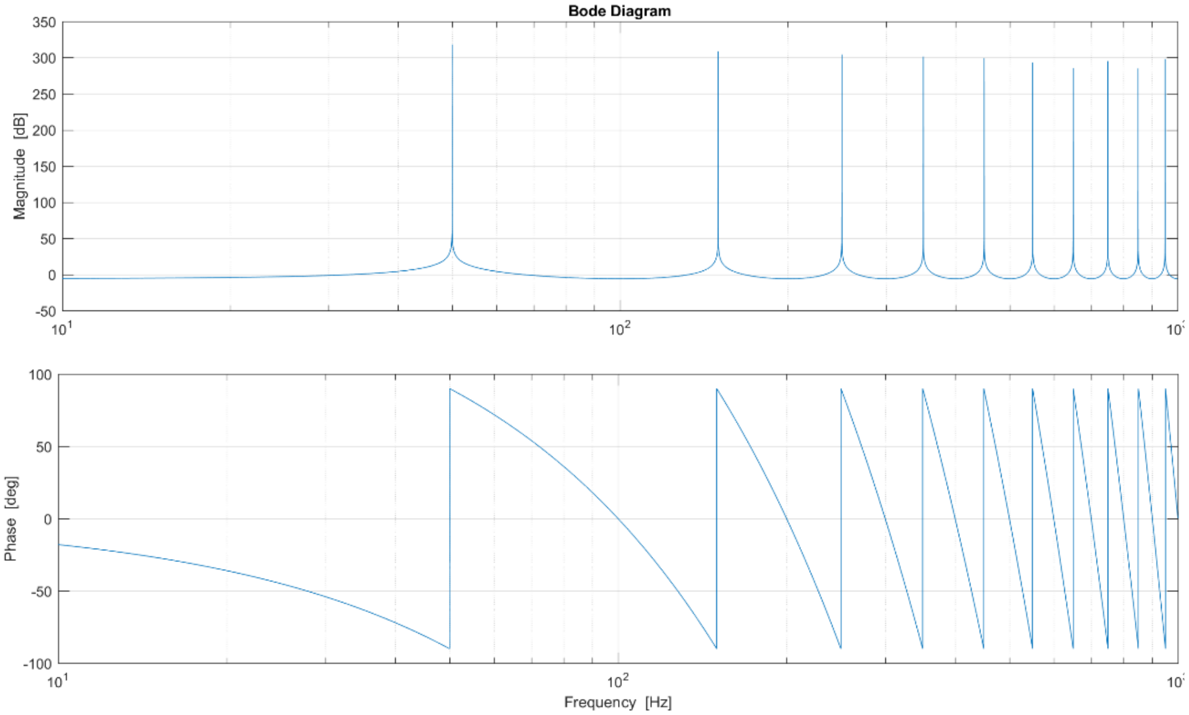

Fig. 2.34 Bode diagrams of the transfer function $G_{OHRC}^{(1)}$ not stabilized

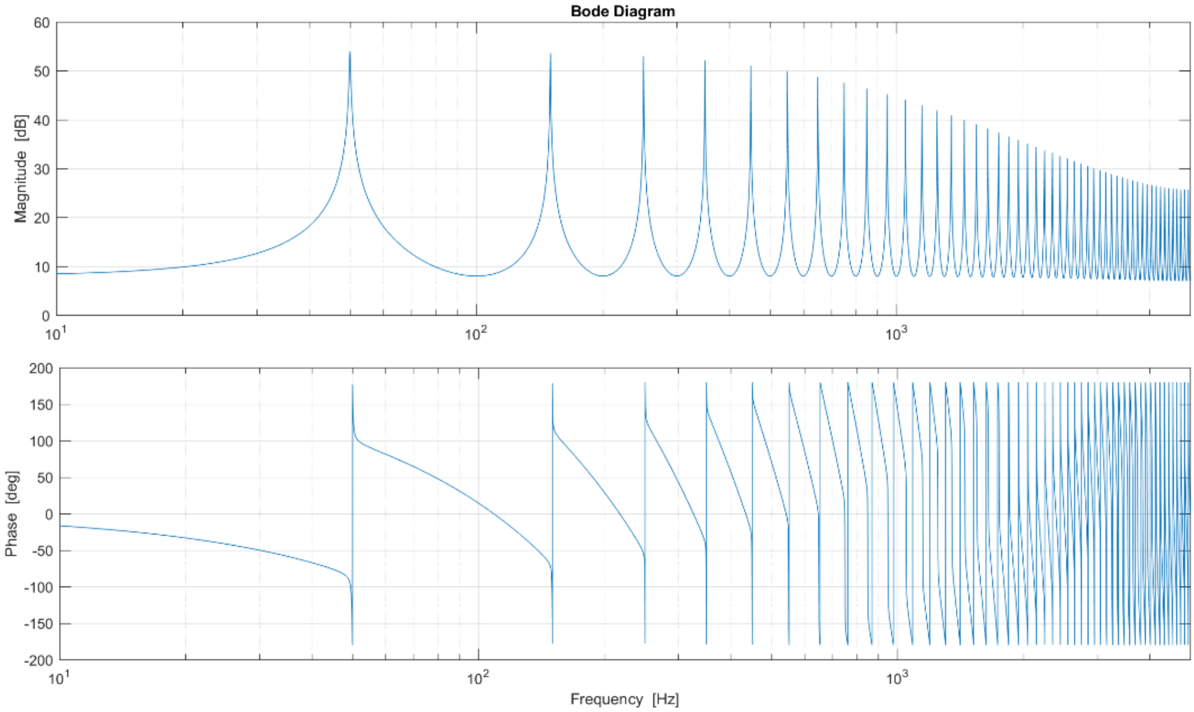

Fig. 2.35 Bode diagrams of the transfer function $G_{OHRC}^{(1)}$ stabilized.

Similar changes can be applied to the control scheme of the second topology in Fig 2.31, that becomes as shown in Fig 2.36. The transfer function becomes:

$$G^{(2)}_{OHRC,plug-in} = -k_s \frac{1-Q(s)e^{-s\left(\frac{T_0}{2}+T_s\right)}}{1+Q(s)e^{-s\left(\frac{T_0}{2}+T_s\right)}} e^{-s\left(\frac{T_0}{2}-T_d\right)} + 1 = 1 + G^{(2)}_{OHRC}, \tag{2.52}$$

which has the same set of resonance frequencies found in (2.51) for $G^{(1)}_{ODRC}$ and presents zeros at even harmonics:

$$\begin{gathered} 1-e^{-j\omega\frac{T_0}{2}} = 1-\cos\left(\omega\frac{T_0}{2}\right) + j\sin\left(\omega\frac{T_0}{2}\right) = 0 \Rightarrow \\ \Rightarrow \omega\frac{T_0}{2} = 2k\pi \Rightarrow f_{zeros} = 2kf_0, \qquad k\in\mathbb{Z}, \end{gathered} \tag{2.53}$$

Fig. 2.37 and Fig. 2.38 show the Bode diagrams for $G^{(2)}_{ODRC}$.

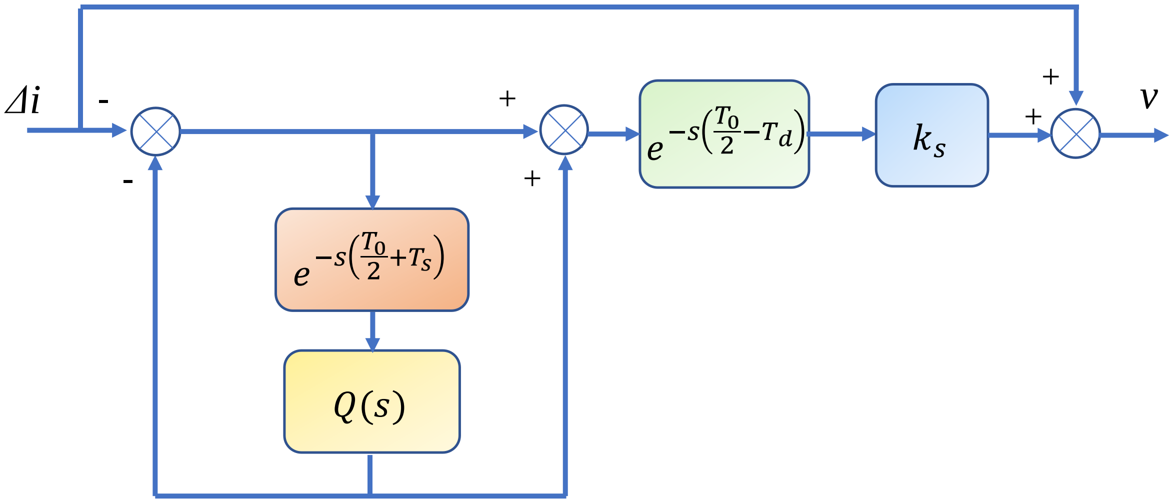

Fig 2.36. Repetitive control scheme implemented – Topology 2, OHRC.

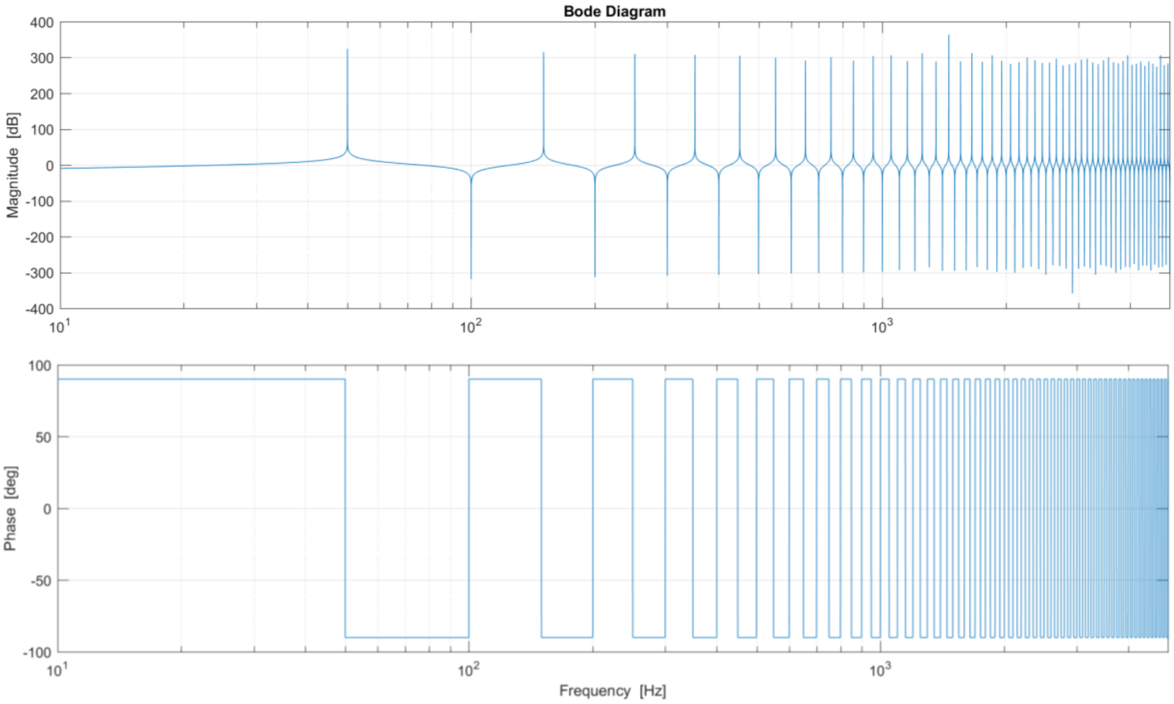

Fig. 2.37 Bode diagrams of the base scheme transfer function $G_{OHRC}^{(2)}$.

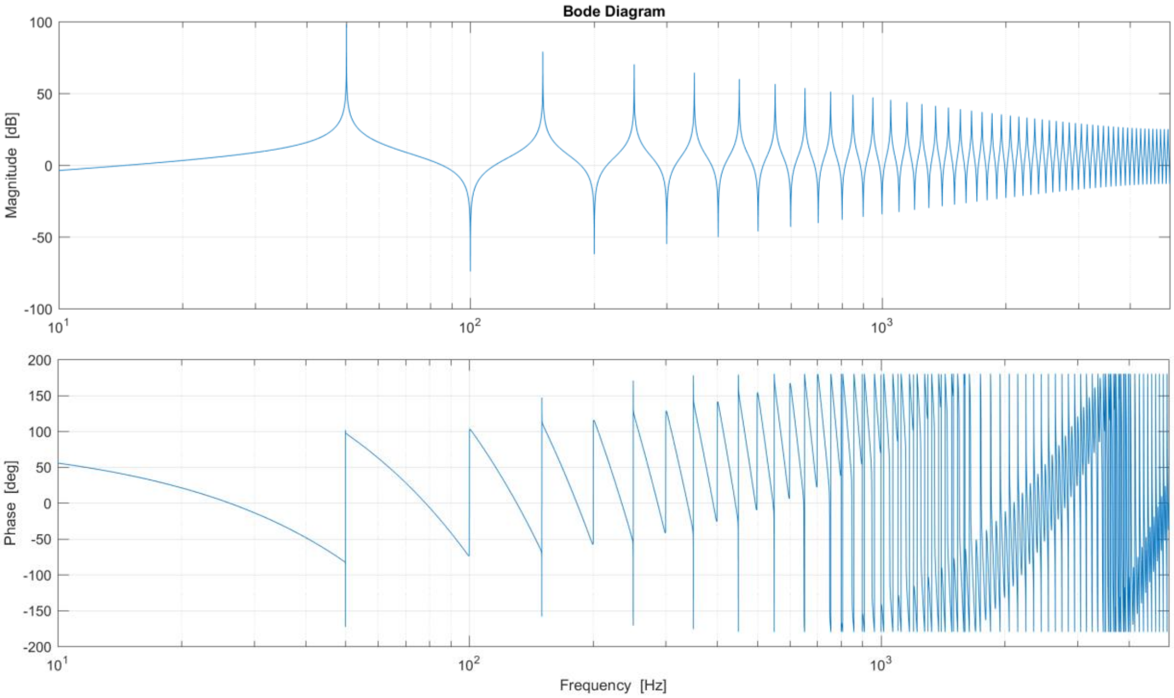

Fig. 2.38 Bode diagrams of the transfer function $G_{OHRC}^{(2)}$ stabilized.

D. *Implemented Current Control*

The whole current control scheme is shown in Fig 2.39.

The regulation of the fundamental component of the current is obtained with a resonant controller which has been tuned as explained in section 2.1.C, while the harmonic compensation has been achieved by the means of the repetitive controllers.

To discretize the repetitive controller, it is assumed that the sampling period is an integer fraction of the fundamental period T_p:

$$e^{-sT_p} = e^{-s(NT_s)} \Rightarrow Z\left(e^{-s(NT_s)}\right) = z^{-N}, \qquad N = \frac{T_p}{T_s} \tag{2.54}$$

where N represents the number of samples stored by the digital processor. For the different repetitive controllers the samples stored are as follow:

$$\begin{aligned} N_{FHRC}^{(1)} &= \frac{T_1}{T_s} = 200 \\ N_{FHRC}^{(2)} &= \frac{2T_1}{T_s} = 400 \\ N_{OHRC}^{(1)} &= \frac{T_1}{2T_s} = 100 \\ N_{OHRC}^{(2)} &= \frac{2T_1}{2T_s} = 200 \end{aligned} \tag{2.55}$$

Due to high number of samples required by the FHRC of the second topology, it has not been possible to test this configuration with the available laboratory setup.

The value of the series gain k_s has been settled to 5Ω for the first topology of repetitive and 2Ω for the second topology, while the coefficient for the filter *Q(s)* has been chosen C_0=0.9 and C_1=0.05 for all the different configurations. The phase lead compensation has been set to $4T_s$.

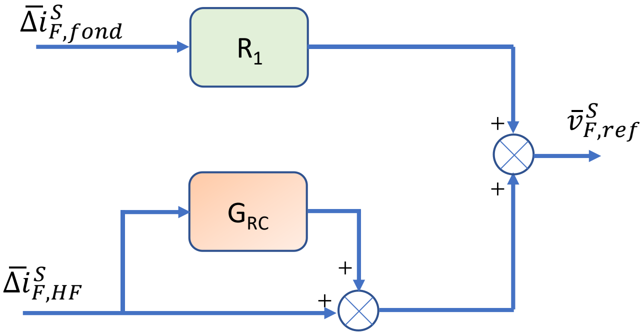

Fig 2.39. Implemented current control.

E. *Experimental Results*

The same laboratory setup used to test the multi-resonant current controller in the section 2.1.E has been used to test the developed repetitive control.

Since the control of the DC-link voltage is still based on a resonant controller, the following experimental results will show just the harmonic compensation achieved with the different types of repetitive controllers.

- *Full Harmonic Repetitive Control – Topology 1 (FHRC)*

Fig. 2.40 shows the transient due to the harmonic compensation achieved for this configuration. In particular, from the top of the figure to the bottom, one can see the waveforms of the power grid phase voltage and current, load current and filter currents.

Fig. 2.41 shows the power factor correction of the power grid current.

In Fig. 2.42 and Fig. 2.43, a closer look to the waveform of the power grid current and the related spectrum confirms the superior behavior of the repetitive control in terms of harmonic compensation.

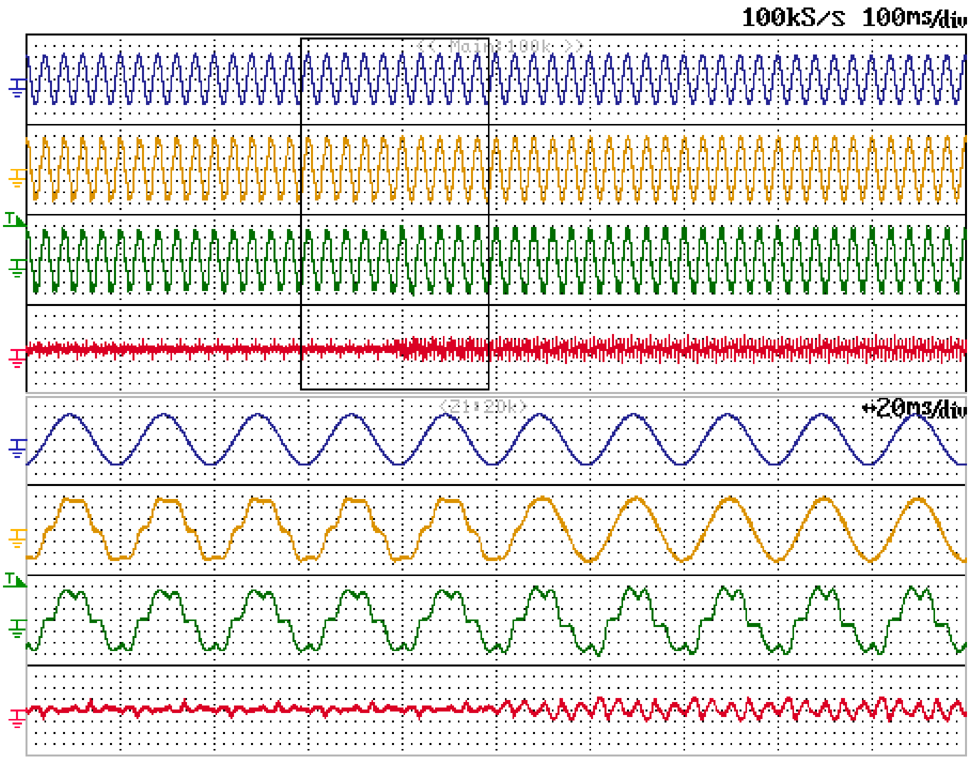

Fig. 2.40 Transient of the power grid phase voltage and current, load current and filter currents due to the activation of the harmonic compensation. Scale: current (2 A/div), voltage (40 V/div). *Full Harmonic Repetitive Control – Topology 1*

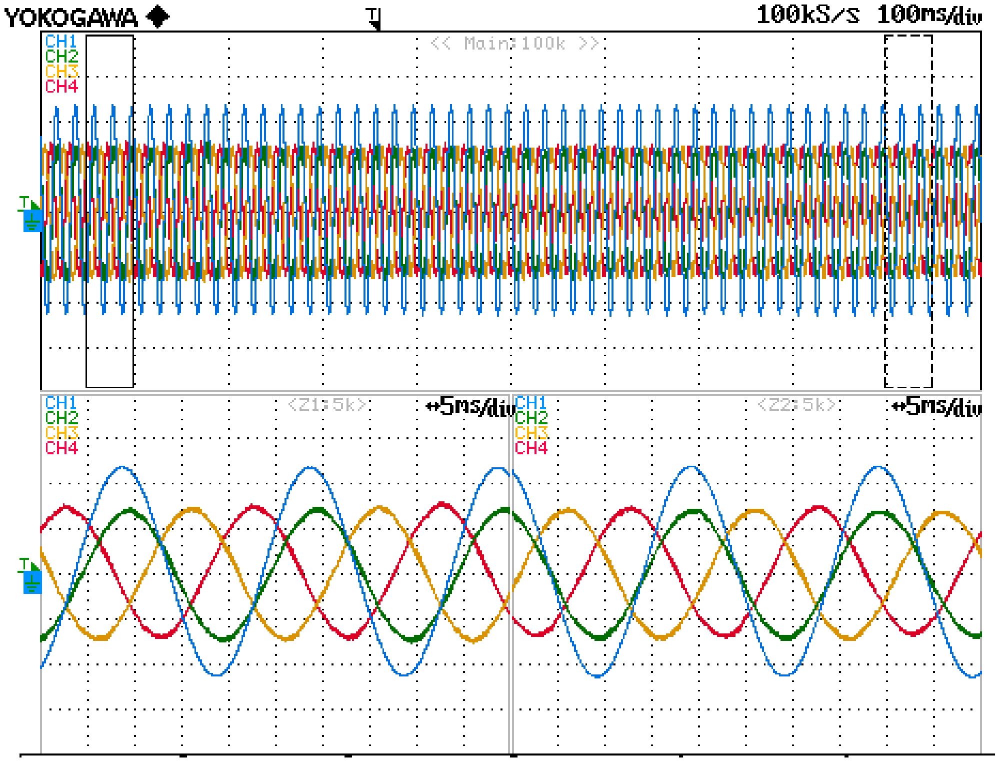

Fig. 2.41 Power factor correction. Scale: current (2 A/div), voltage (40 V/div). *Full Harmonic Repetitive Control – Topology 1*

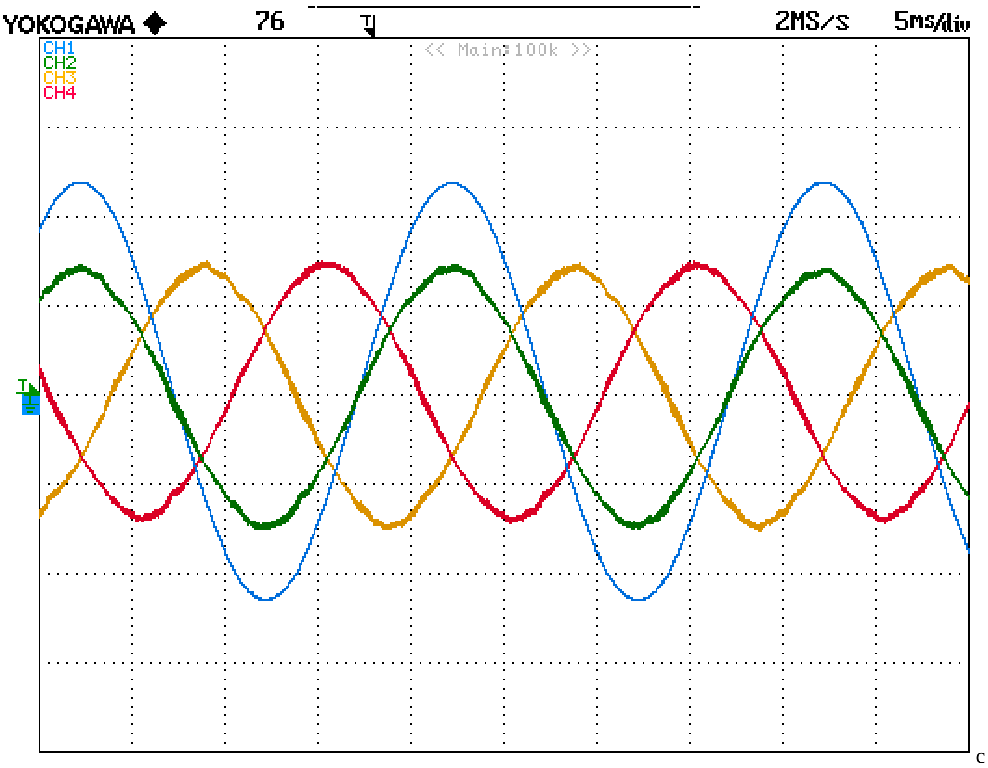

Fig. 2.42 Waveform of the grid currents and fundamental component of the phase voltage when the APF is on. Scale: current (2 A/div), voltage (40 V/div). *Full Harmonic Repetitive Control – Topology 1*

This result is confirmed by the value of the THD that drops from the starting value of 21.56% when the RC is off, to a value of 2,73% when it is on.

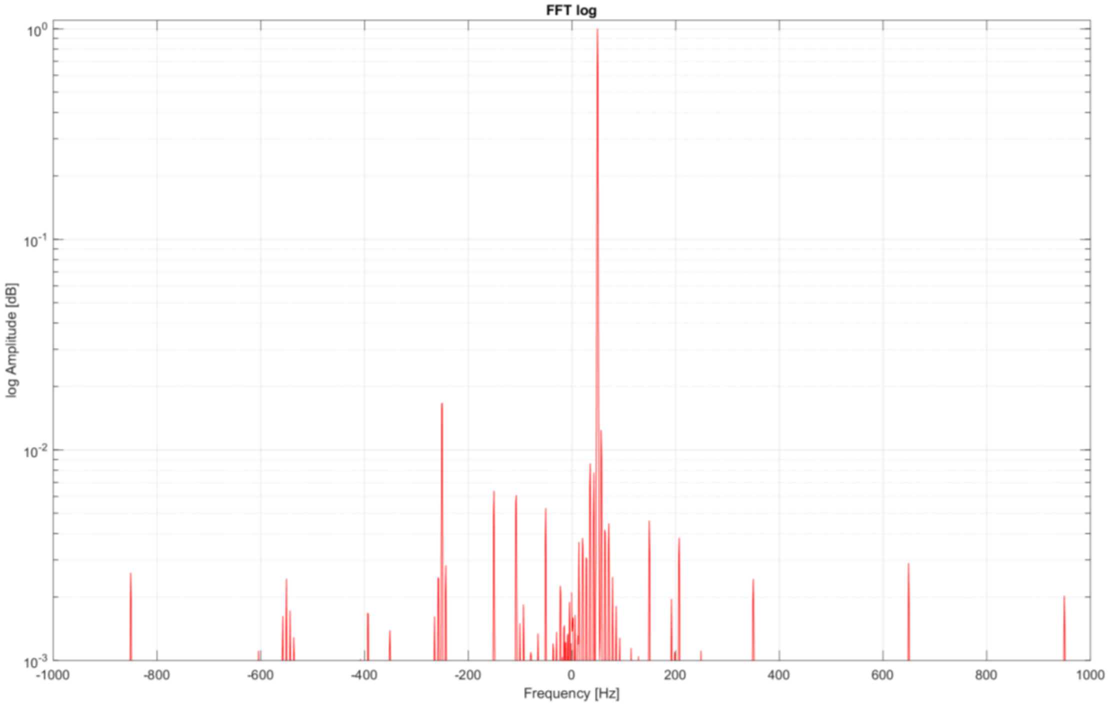

Fig. 2.43 Normalized spectra of the grid currents when the APF is on.
Full Harmonic Repetitive Control – Topology 1

- *Odd Harmonic Repetitive Control – Topology 1 (OHRC)*

Fig. 2.44 shows the transient of the power grid phase voltage and current, load current and filter currents after the activation of the harmonic compensation for the OHRC case. The same transient is shown in Fig. 2.45 while in Fig. 2.46 there is the waveform of the power grid current, when the power factor is unity. The spectrum of the currents after the compensation is shown in Fig. 2.47, with a THD of 2,29%.

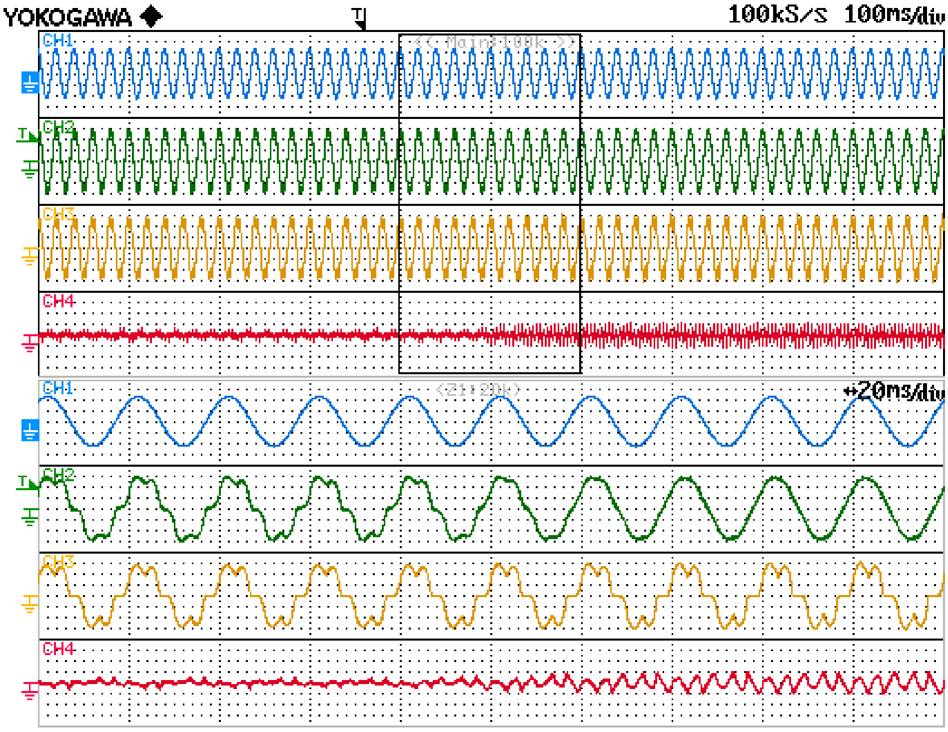

Fig. 2.44 Transient of the power grid phase voltage and current, load current and filter currents due to the activation of the harmonic compensation. Scale: current (2 A/div), voltage (40 V/div). *Odd Harmonic Repetitive Control – Topology 1*

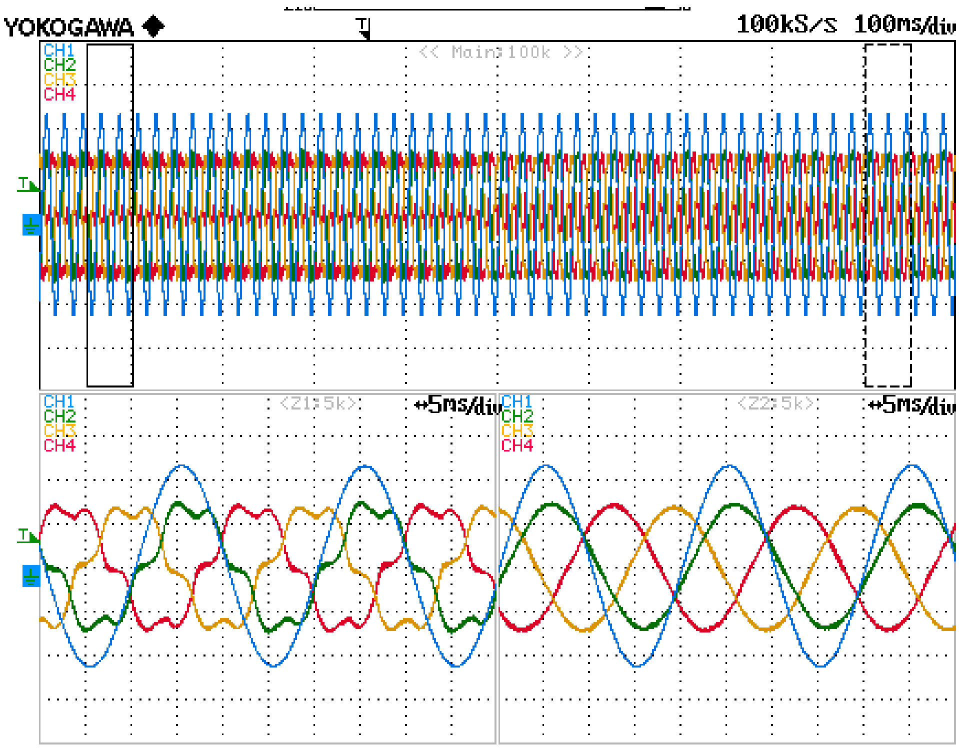

Fig. 2.45 Transient of the power grid phase voltage and filter currents due to the activation of the harmonic compensation. Scale: current (2 A/div), voltage (40 V/div). *Odd Harmonic Repetitive Control – Topology 1*

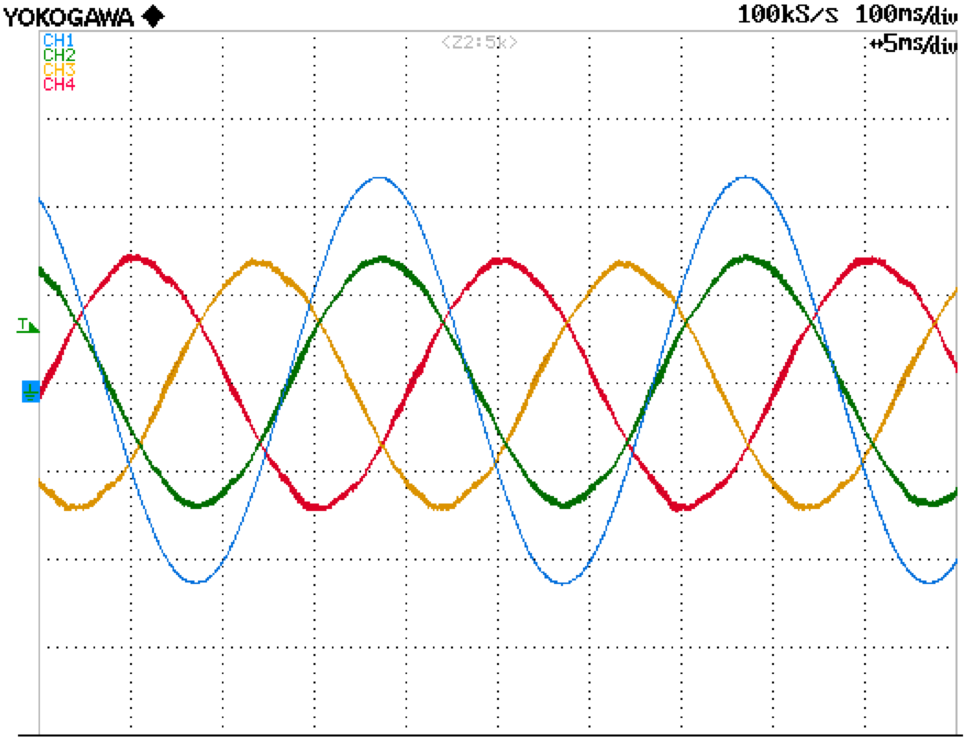

Fig. 2.46 Waveform of the grid currents and fundamental component of the phase voltage when the APF is on. Scale: current (2 A/div), voltage (40 V/div).
Odd Harmonic Repetitive Control – Topology 1

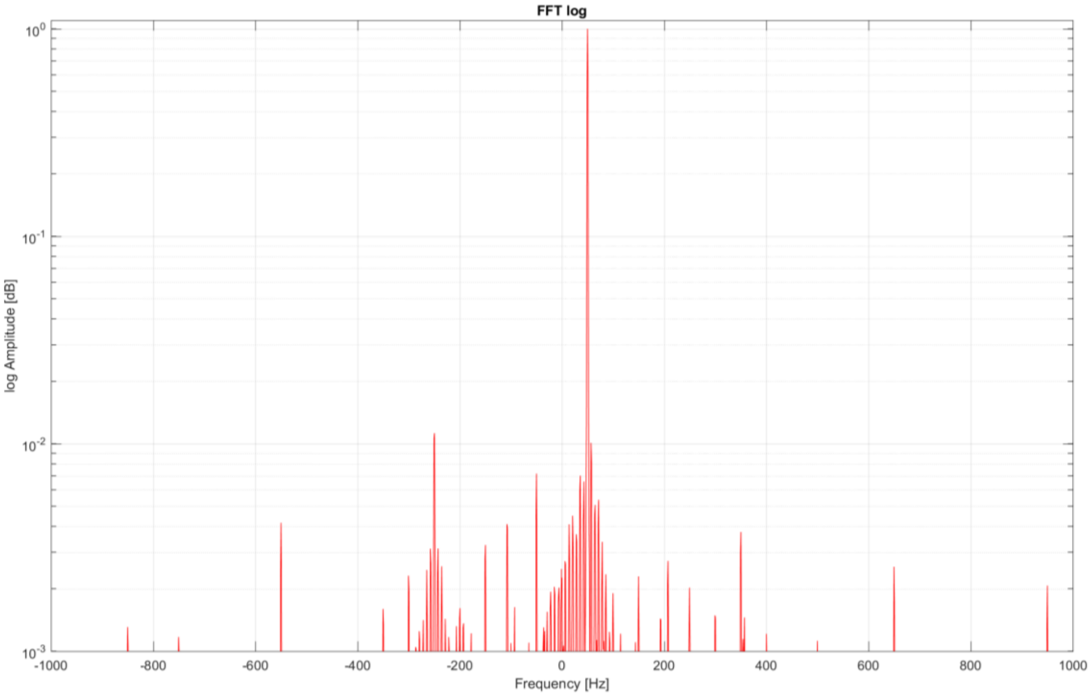

Fig. 2.47 Normalized spectra of the grid currents when the APF is on.
Odd Harmonic Repetitive Control – Topology 1

- *Odd Harmonic Repetitive Control – Topology 2 (OHRC)*

Fig. 2.48 shows the transient of the power grid phase voltage and current, load current and filter currents after the activation of the harmonic compensation, while Fig. 2.49 focuses just on the power grid currents.

Finally, the grid currents with unity power factor are shown in Fig. 2.50 and the harmonic spectrum in Fig. 2.51.The THD for this configuration drops to 2,21%.

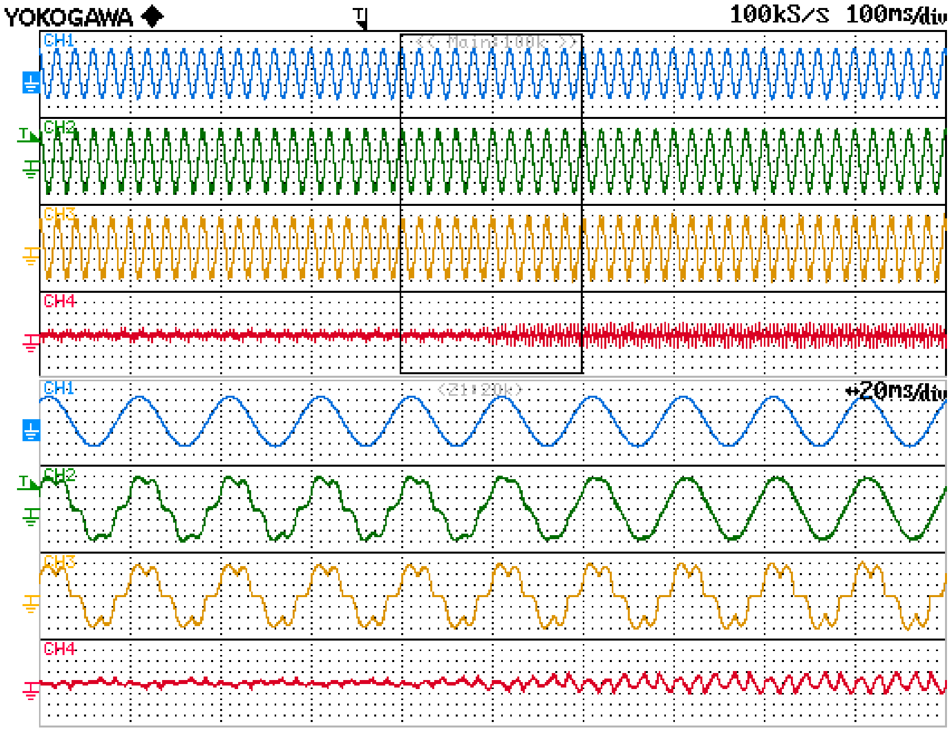

Fig. 2.48 Transient of the power grid phase voltage and current, load current and filter currents due to the activation of the harmonic compensation. Scale: current (2 A/div), voltage (40 V/div). *Odd Harmonic Repetitive Control – Topology 2*

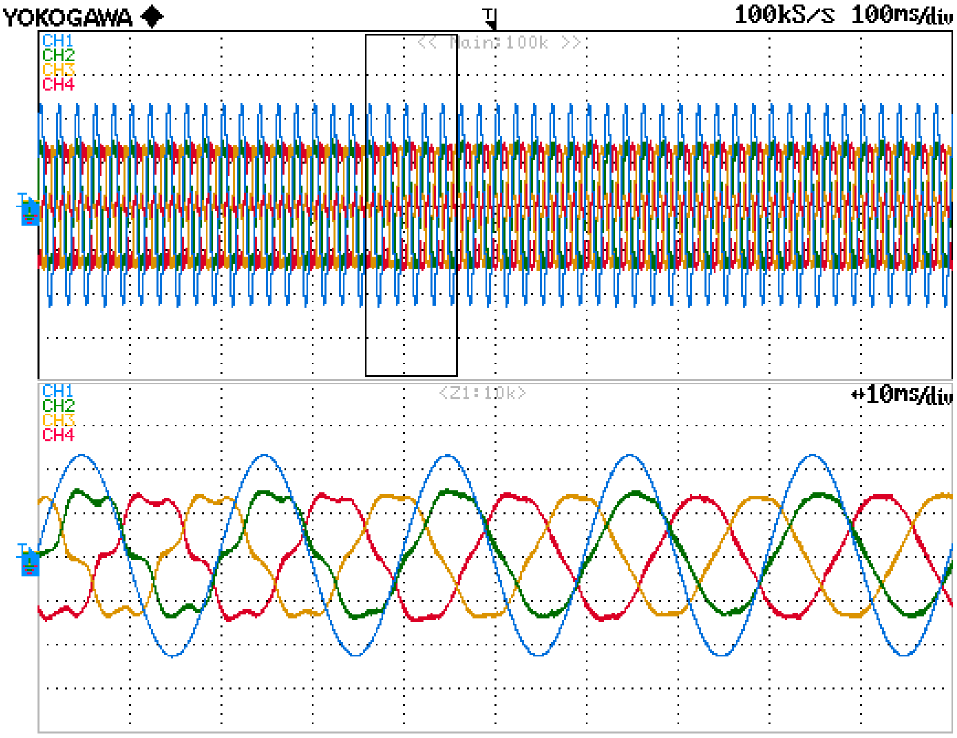

Fig. 2.49 Transient of the power grid phase voltage and filter currents due to the activation of the harmonic compensation. Scale: current (2 A/div), voltage (40 V/div). *Odd Harmonic Repetitive Control – Topology 2*

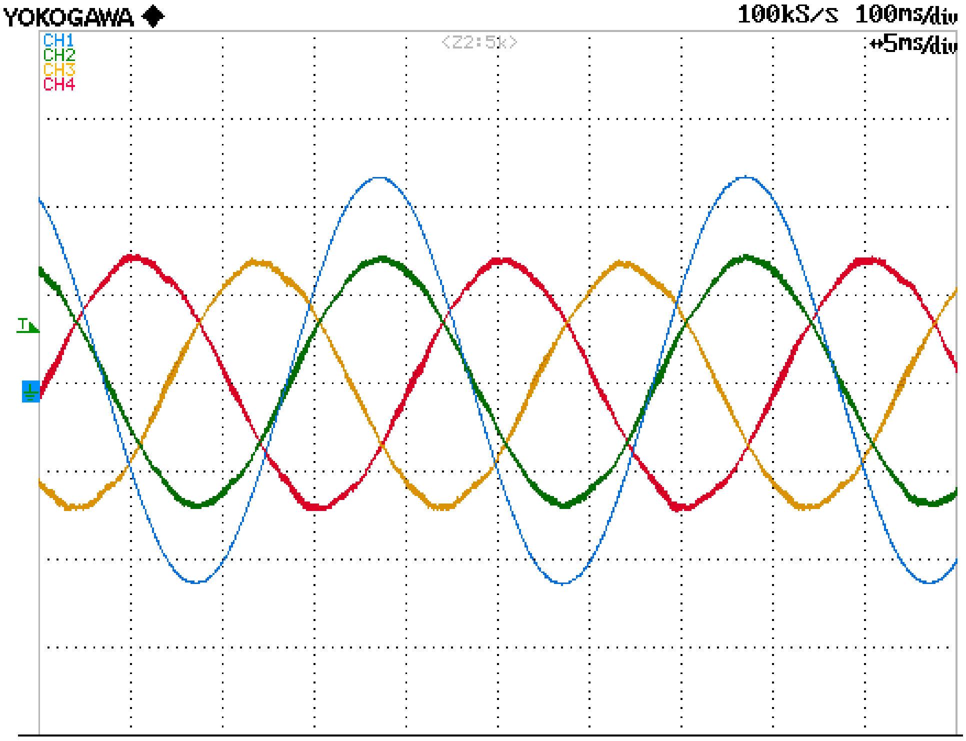

Fig. 2.50 Waveform of the grid currents and fundamental component of the phase voltage when the APF is on. Scale: current (2 A/div), voltage (40 V/div).
Odd Harmonic Repetitive Control – Topology 2

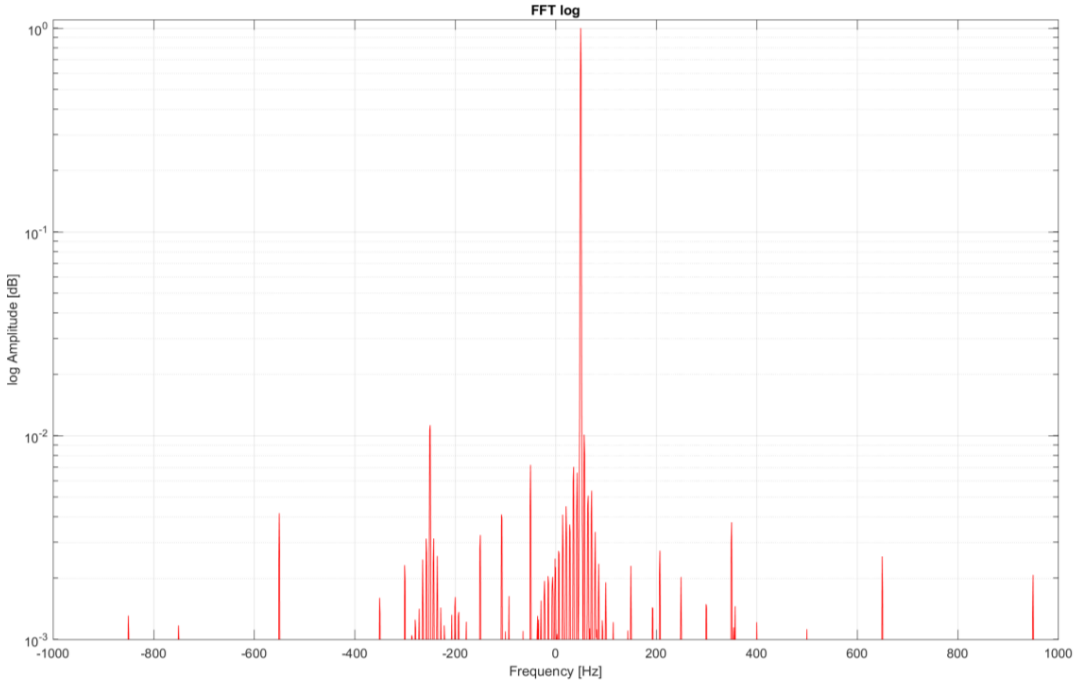

Fig. 2.51 Normalized spectra of the grid currents when the APF is on.
Odd Harmonic Repetitive Control – Topology 2

F. *Effects of the Delay Compensation*

The effects of the phase lead $T_d = nT_s$ on the harmonic compensation has been evaluated. The FHRC topology 1 has been used for this evaluation and the results are shown in TABLE 3.

TABLE 3 – DELAY COMPENSATION

n	***THD***
0	*Unstable*
0.5	*Unstable*
1	*Unstable*
1.5	3.72
2	3.15
2.5	2.81
3	2.66
3.5	2.70
4	2.73
4.5	2.51
5	2.83

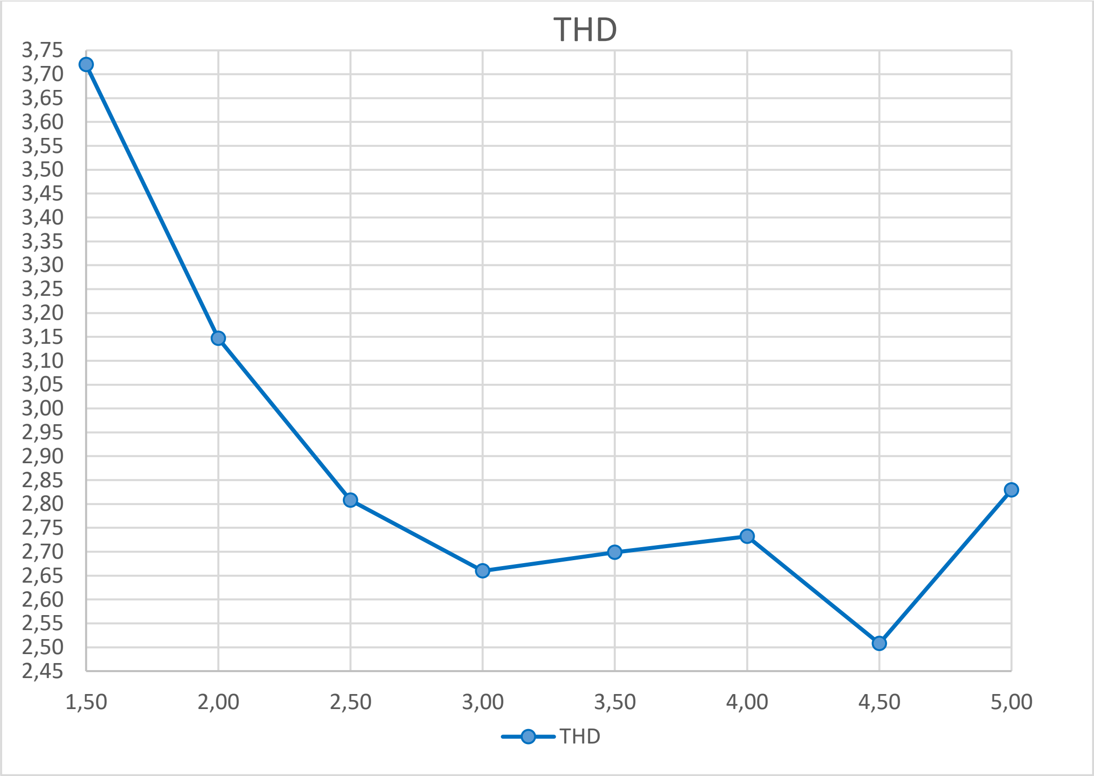

Fig. 2.52 THD for different value of the delay compensation.
Full Harmonic Repetitive Control – Topology 1

This configuration proved to be unstable for a delay compensation T_d below one sample time T_s and above five, while it keeps an almost constant behavior, in terms of THD, from 3 to 4.5. The oscillations of the THD are mostly due to random fluctuations of the grid voltage.

Fig. 2.52 shows the trend of the THD as function of the delay compensation.

2.3 CONSIDERATIONS

In this chapter, the resonant and repetitive current controllers have been studied and tested. The experimental results have shown good performance in terms of harmonic compensation for both. The THD of the grid currents are shown in TABLE 4.

TABLE 4 – THD COMPARISON

Current Controller	***THD***
Resonant	2,60%
FHRC– Topology 1	2,73%
OHRC– Topology 1	2,29%
OHRC– Topology 2	2,21%

Both resonant and repetitive current controllers are able to keep the THD of the grid currents below 3% starting from a THD of 21,56% occurring without harmonic compensation.

The similar results are easier to understand if the frequency response of the two regulators are taken into account. The resonant controller presents peaks at frequencies from the third to the nineteenth harmonics, while the repetitive control allows one to compensate all the harmonics of the fundamental one through a feedback loop of the reference signal delayed by a fundamental period or less, depending on the topology used. Thus, the latter should compensate harmonics of higher order up to the Shannon frequency of the control system, implying better performance compared to the resonant control. However, the zero-phase filter used to stabilize the repetitive controller has been designed to have a cut-off frequency around 1 kHz, making therefore the compensation of high order harmonics less effective.

Further considerations can be made on the implementation of the two controllers. The repetitive controller requires a memory effort to store all the needed samples in a buffer, but the computational burden is quite small, compared to the one required by the array of resonant controllers. It is then possible to increase the switching frequency and to reduce the current ripple.

On the other hand, the features of selectivity provided by the resonant controllers has two advantages over nonselective solutions, such as the repetitive control. Firstly, the stability of the system can be enhanced because the gains of the regulators can be adjusted depending on the frequency of the cancelled harmonics. Secondly, in the case of voltage overmodulation or current saturation, the control system can choose which harmonics have to be compensated without compromising the overall performance. This topic is widely investigated in the next chapter.

Chapter 3

ADAPTATIVE VOLTAGE SATURATION FOR AN APF

A problem that has been investigated in this PhD work is the exploitation of the DC-link voltage of the APF when the reduction of the high frequency harmonics is performed by an array of resonant controllers. Since the output voltage of the APF is obtained as a sum of several contributions, one for each harmonic component of the current disturbance, if the magnitude of the output voltage is greater than the maximum admissible voltage, the entire converter runs the risk of an uncontrolled reduction of performance, because the effect of voltage saturation on the compensation of each harmonic is unpredictable.

3.1 OPERATION OF AN APF UNDER CONSTRAINTS

A. *Current and Voltage Constraint*

The mathematical model of an APF has been already studied in Section 1.1. To complete the mathematical model, the voltage and current constraints have to be taken into account.

In fact, the performance of an APF is limited by the rated current $I_{F,max}$ of the converter and the available voltage $V_{F,max}$ of the floating DC-link. These constraints can be expressed by the following inequalities:

$$\left|\bar{i}_F\right| \le I_{F,max} \tag{3.1}$$

$$\left|\bar{v}_F\right| \le V_{F,\max} \tag{3.2}$$

where $V_{F,max}$ is equal to $0.57E_F$ if space vector modulation is used.

If the current control is achieved by the means of an array of resonant controllers, as shown in “Implemented Multi-Resonant Current Control”, the output voltage vector of the APF consists in the sum of outputs of each resonant controller and can be written as follows:

$$\bar{v}^S_{F,ref} = \sum_{k=1,\dots,n} \bar{v}^S_{Fk,ref} \ , \tag{3.3}$$

where $\bar{v}^S_{Fk,ref}$ (k=1, …, n) is the contribution to the output voltage produced by the kth regulator.

The output voltage given by (3.3) should comply with (3.2), so the *k*th regulator must exploit only a fraction of the DC-link voltage at disposal. Consequently, the output voltage of each proportional-resonant regulator is constrained by a saturation block, whose equation can be written as follows:

$$\overline{v}^{S}_{Fk,ref} = c_k \overline{v}^{S}_{Fk,req}\,,\ (k{=}1,\ \ldots,\ n) \qquad (3.4)$$

where c_k is a positive coefficient not greater than one, and $\overline{v}^{S}_{Fk,req}$ is the voltage requested by the *k*th resonant controller without saturation constraints. To analyze this problem, in practical applications, it is necessary to distinguish between the fundamental component and the high frequency component of voltage $\overline{v}_F$. While the latter is used to reduce the distortion of the load currents, the former is necessary to control the average active and reactive powers and, consequently, the converter stability.

Let's consider the operation of an APF through a graphical analysis of the space vectors of the voltage applied and the current injected by it. The current absorbed by the filter is given by the equation of the voltage drop across the decoupling inductance L_F (1.4). In steady state condition and by neglecting the drop on the resistance R_F, (1.4) becomes

$$\overline{v}_G - \overline{v}_F = j\omega L_F \overline{i}_F\,. \qquad (3.5)$$

In Fig. 3.1 some working condition are shown.

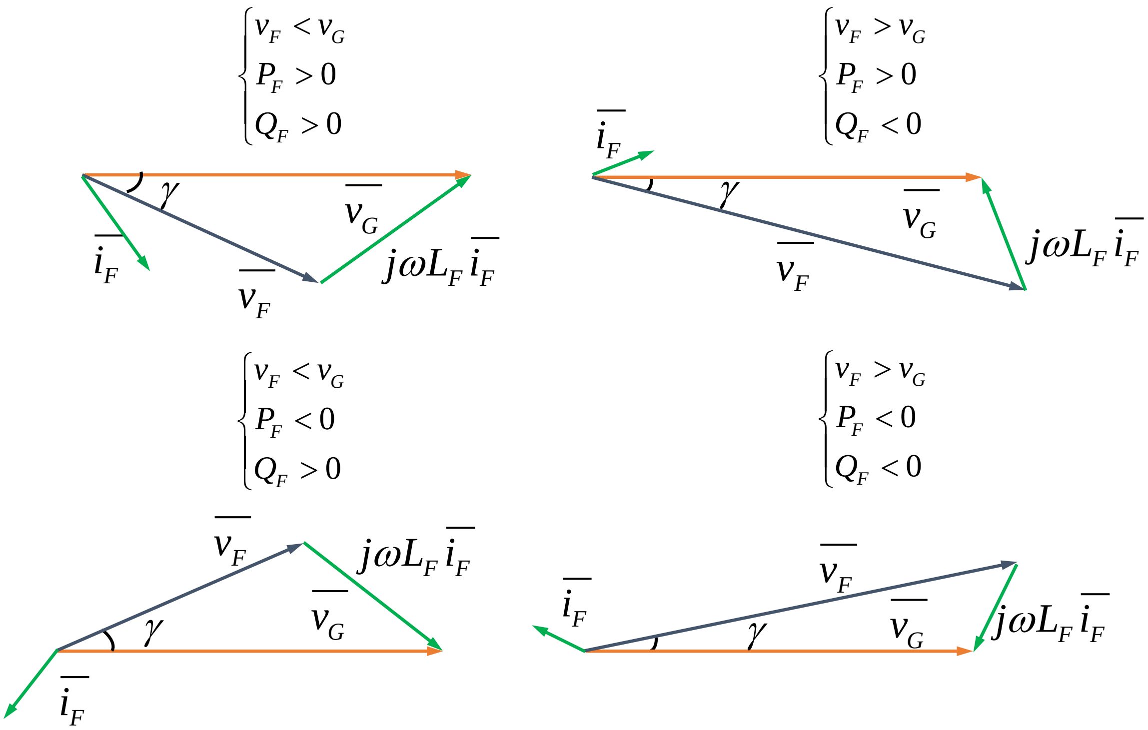

Fig. 3.1 Example of different working condition for an APF

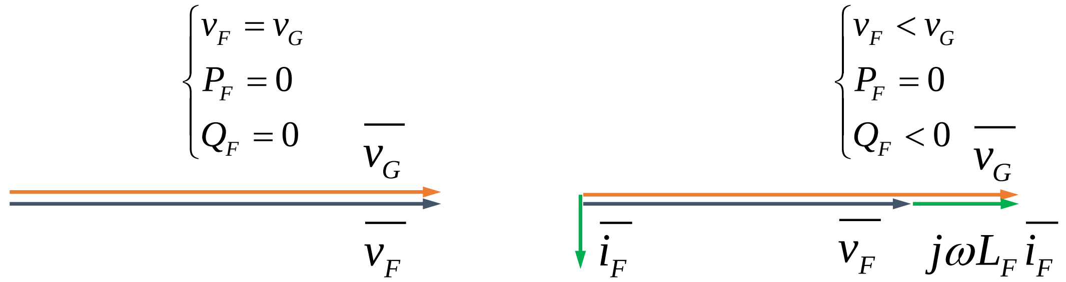

Fig. 3.2. Available voltage on the DC-link sufficient to nullify the filter current a) and available voltage not sufficient b)

To nullify the current injected in the power grid, it is necessary to apply a voltage output equal to the power grid voltage as shown in Fig. 3.2(a). If the voltage available on the DC-link is lower than the phase to phase peak voltage of the power grid, then it is not possible to nullify the current $\overline{i}_F$. In this case, it is still possible control the active power exchanged but not the reactive one. The value of the reactive current absorbed depends on the difference between the grid and the APF voltage, as shown in Fig. 3.2(b).

In this condition the APF in unable to work, therefore, the first goal of the control system is to ensure stable operation of the APF and, only later, to improve the quality of the line currents.

The allocation of the DC-link voltage to each regulator should privilege the control of the fundamental component of the filter current, in order to ensure the basic operation of the converter, while the harmonic currents should be compensated with the residual voltage that is not used to control the fundamental component. As a consequence, coefficient c_1 is normally equal to 1, provided that the magnitude of the fundamental voltage is below $V_{F,\max}$. Conversely, the other coefficients c_k may be lower than 1, depending on whether the available DC-link voltage is sufficient or not to synthesize the resulting total voltage $\overline{v}_{F,ref}^{S}$.

B. *Anti-Windup Technique*

In case of saturation it is necessary to tackle the problem of wind-up, which may arise due to the integral action of the regulators. If the wind-up problem is not properly managed or it is partially treated, the system may become unstable.

Among the possible solutions to the problem of wind-up, the basic one is to consider all regulators as a whole. Once the magnitude of $\overline{v}_F^S$ exceeds the admissible voltage, it is necessary to sum a feedback signal to the input error (back-calculation), shown in Fig. 3.3(a).

Unfortunately, the choice of the feedback gain to ensure the system stability is not always simple and it has to be updated if the set of compensated harmonics changes.

A possible remedy is to treat the wind-up problem of each regulator independently of the others, Fig. 3.3(b). This solution is more flexible, but the number of back-tracking gains to be tuned increases, and the maximum voltage $V_{k,max}$ has to be chosen for each regulator.

In digital control systems, it is possible to invert the discrete-time equation of the regulator and re-calculate the input error as a function of the saturated output, Fig. 3.4. This solution avoids the problem of choosing the back-tracking gains.

The previous technique can be improved by calculating automatically $V_{k,max}$ depending on the operating conditions. In addition $V_{k,max}$ should be dynamically changed in such a way that the compensation of the most significant current harmonics is privileged.

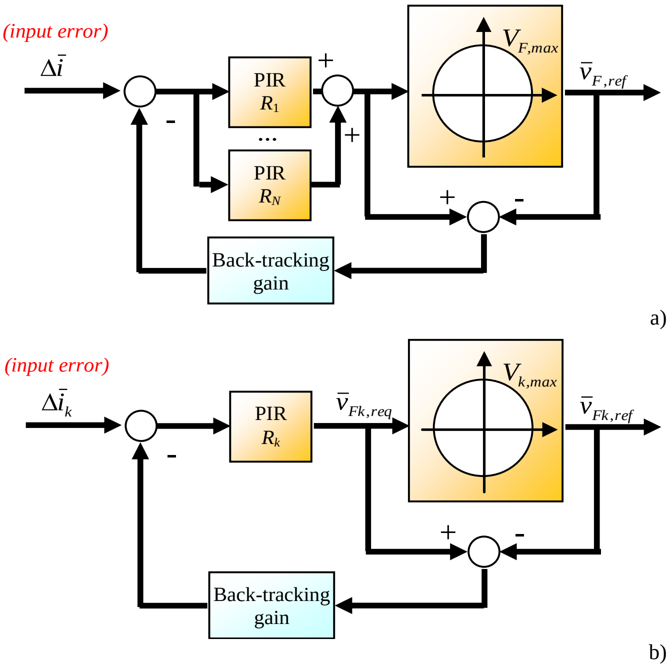

Fig. 3.3. Anti-windup configurations with back-tracking of the saturation signal for the whole array of PR controllers a) and separately for each PR controller b)

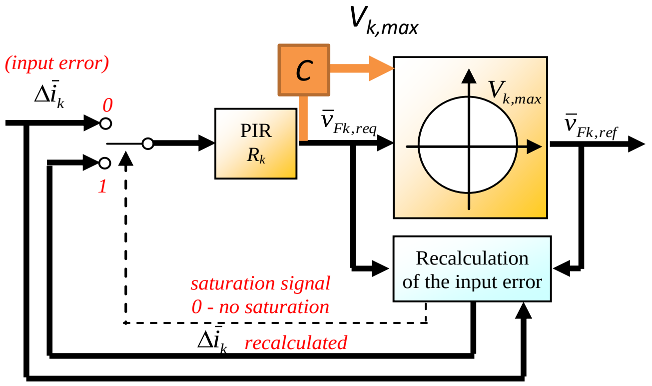

Fig. 3.4. Anti-windup Anti-windup configurations for proportional resonant controllers. With recalculation of the input error.

Consequently, $V_{k,max}$ should be chosen in proportion to the corresponding voltage request, so that the regulators involved in the cancellation of high currents are less penalized:

$$V_{k,\max} = c_k \left|\bar{v}^{s}_{Fk,req}\right| \tag{3.6}$$

and this proportion is decided through the coefficient c_k already defined in (3.4)

Different strategies can be used for the repartition of the available voltage among the regulators and for the selection of the coefficients c_k.

3.2 SATURATION STRATEGIES

A. *Strategy 1*

The output $\overline{v}^{S}_{Fk,req}$ of each regulator R_k has to be limited to values with a magnitude not greater than the quantity $V_{k,max}$. The resulting equation of the saturation block is as follows:

$$\overline{v}^{s}_{Fk,ref}=\begin{cases} V_{k,\max}\dfrac{\overline{v}_{Fk,req}}{\left|\overline{v}_{Fk,req}\right|} & if\ \left|\overline{v}_{Fk,req}\right|>V_{k,\max} \\ \overline{v}_{Fk,req} \end{cases} \tag{3.7}$$

Under the assumption that the magnitude of $\overline{v}_{F1,req}$ is less than $V_{F,max}$, to satisfy (3.2), it is sufficient that the upper bounds $V_{k,max}$ (k=1, 2, …, N) are chosen so that

$$\sum_{k\in N,k\neq 1} V_{k,max}\leq V_{F,max}-\left|\overline{v}^{s}_{F1,ref}\right| \tag{3.8}$$

The simplest choice for $V_{k,max}$ is to assume an equal repartition of the residual voltage among all regulators,

$$V_{k,max}=\frac{V_{F,max}-\left|\overline{v}^{s}_{F1,ref}\right|}{N-1}. \tag{3.9}$$

However, this choice does not consider that the voltage request for the voltage harmonics is usually not uniform, because some current harmonics may be more prominent than the other, so $V_{k,max}$ is chosen as in (3.6). By substituting (3.6) in (3.8), considering it as an equality, it is possible to find a unique value for the coefficient c_k,

$$c=\frac{V_{F,\max}-\left|\overline{v}^{S}_{F1,ref}\right|}{\sum\limits_{k\in 2,\dots,N}\left|\overline{v}^{S}_{Fk,req}\right|}. \tag{3.10}$$

As a consequence of this saturation strategy, the control system tends to ensure higher voltage margin to the regulators that are more overloaded, while the performance of the fundamental controller is preserved.

It is worth to make some considerations about this strategy. As shown in (3.3), the total output voltage $\overline{v}^{S}_{F,ref}$ is composed of several contributes, rotating at different frequencies, meaning therefore that its magnitude is not constant on a period of the fundamental and it can be lower or higher than the upper voltage limit $V_{F,max}$, as shown in Fig. 3.5(a) and (b) respectively, where for sake of simplicity, the total output voltage is composed just by the

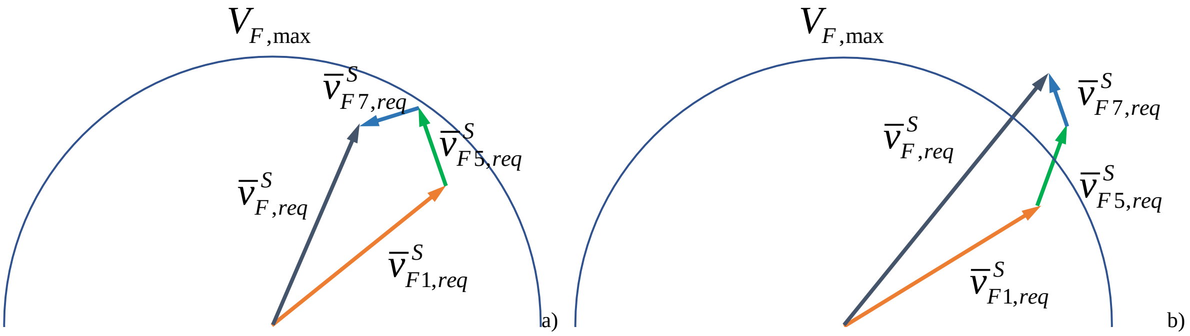

Fig. 3.5. Space vector representation of the total output voltage under the upper voltage limit a) and above it b)

first, the fifth and the seventh harmonics.

The strategy 1 however, limits the output for the whole period, since it considers the worst case, when the harmonics sum up in phase, making the harmonics compensation less effective. This concept can be mathematically expressed by considering that the value of c in (3.10) can be also obtained from the following triangular inequality:

$$\begin{aligned}&\left|\overline{v}^S_{F1,ref}+\sum_{k=2,\dots,n}\overline{v}^S_{Fk,ref}\right|\le\left|\overline{v}^S_{F1,ref}\right|+\sum_{k=2,\dots,n}\left|\overline{v}^S_{Fk,ref}\right|\le\\&\le\left|\overline{v}^S_{F1,ref}\right|+c\sum_{k=2,\dots,n}\left|\overline{v}^S_{Fk,req}\right|\le V_{F,\max}\end{aligned}\tag{3.11}$$

B. *Strategy 2*

Coefficients c_k are assumed equal to each other, as in Strategy 1. Let us call this common value c'. This quantity differs from c, defined for Strategy 1, because it is calculated without the simplification introduced by the triangular inequality, but it considers also the phases of the resonant controller outputs. Substituting (3.3)-(3.4) in (3.2), and considering c_k=c', leads to the following inequality:

$$\left|\overline{v}^S_{F1,ref}+\sum_{k=2,\dots,n}\overline{v}^S_{Fk,ref}\right|=\left|\overline{v}^S_{F1,ref}+c'\sum_{k=2,\dots,n}\overline{v}^S_{Fk,req}\right|\le V_{F,\max}\,. \tag{3.12}$$

Squaring both sides, one obtains:

$$a_2\left(c'\right)^2+2a_1c'+a_0\le 0\,. \tag{3.13}$$

where a_0, a_1 and a_2 are defined as follows:

$$a_0=\left|\overline{v}^S_{F1,ref}\right|^2-V^2_{F,\max}\,. \tag{3.14}$$

$$a_1 = \overline{v}^S_{F1,ref} \cdot \sum_{k=2,\dots,n} \overline{v}^S_{Fk,req} \,. \tag{3.15}$$

$$a_2 = \left| \sum_{k=2,\dots,n} \overline{v}^S_{Fk,req} \right|^2 . \tag{3.16}$$

Inequality (3.12) admits an explicit interval of solutions for c' if its discriminant is positive, as shown in (3.17). A sufficient condition to find a solution is that $\left|\overline{v}^S_{F1,ref}\right|$ is lower than $V_{F,\max}$:

$$\left(\overline{v}^S_{F1,ref} \cdot \sum_{k=2,\dots,n} \overline{v}^S_{Fk,req}\right)^2 + \left[V^2_{F,\max} - \left(\overline{v}^S_{F1,ref}\right)^2\right] \left|\sum_{k=2,\dots,n} \overline{v}^S_{Fk,req}\right|^2 \geq 0 \,. \tag{3.17}$$

The maximum value of c' that satisfies (3.12) is

$$c' = \frac{\sqrt{a_1^2 - a_2 a_0} - a_1}{a_2} \,. \tag{3.18}$$

It is worth noting that c' is a time-variant quantity because coefficients a_1 and a_2 depend on the phase angle of the voltage vectors $\overline{v}^S_{Fk,req}$, as can be seen from (3.14)-(3.15).

C. *Strategy 3*

A further improvement can be applied to the saturation algorithm if it is considered that, during the fundamental period, some harmonic components contribute to the total output voltage by increasing its magnitude, others by decreasing it, depending on the phase they sum up. The latter don't need to be limited, since they usefully contribute to reduce the total output voltage requested. This feature can be evaluated by considering the derivative of the total output voltage magnitude with respect to the voltage harmonic under evaluation:

$$\frac{\partial \left|\overline{v}^S_{F,req}\right|}{\partial \overline{v}^S_{Fk,req}} = \frac{\partial \left|\overline{v}^S_{F1,ref} + \sum_{k=2,\dots,n} \overline{v}^S_{Fk,req}\right|}{\partial \overline{v}^S_{Fk,req}} \,. \tag{3.19}$$

In particular, it is necessary to evaluate the sign of (3.19), to understand if the *k*th harmonic is contributing to increase the magnitude of the total output voltage. It is then equivalent to consider the square of $\left|\overline{v}^S_{F,req}\right|$, given by the following expression:

$$\frac{\partial\left(\left(\overline{v}_{F1,ref}^{S}\right)^{2}+\sum_{k=2,\dots,n}\left(\overline{v}_{Fk,req}^{S}\right)^{2}+2\overline{v}_{F1,ref}^{S}\cdot\sum_{k=2,\dots,n}\overline{v}_{Fk,req}^{S}+\sum_{h=2,\dots,n}\overline{v}_{Fh,req}^{S}\cdot\sum_{k=2,\dots,n}\overline{v}_{Fk,req}^{S}\right)}{\partial\overline{v}_{Fk,req}^{S}}\,. \tag{3.20}$$

Developing the last derivative and considering the contribute of the first harmonic greater than the ones of higher harmonics, one finds:

$$\frac{\partial\left|\overline{v}_{F,ref}^{S}\right|^{2}}{\partial\overline{v}_{Fk,req}^{S}}\simeq 2\left|\overline{v}_{Fk,ref}^{S}\right|+2\left|\overline{v}_{F1,ref}^{S}\right|\left|\overline{v}_{Fk,ref}^{S}\right|\cos\left(\psi_{k}\right). \tag{3.21}$$

where ψ_k represents the relative phase of the *k*th harmonic respect the fundamental one.

The harmonics whose relation (3.21) gives a negative value, do not need to be saturated.

Let us call N_n the set of indexes of the vectors that give a negative or null contribution to the magnitude of the output voltage, and N_p the set of the indexes of the vectors that give a positive contribution.

The coefficient c_k is assumed equal to 1 if $k \in N_n$. For the remaining vectors ($k \in N_p$), c_k is assumed equal to the maximum value of c'' that verifies the following inequality:

$$\left|\overline{v}_{F1,ref}^{S}+\sum_{k\in N_n}\overline{v}_{Fk,req}^{S}+c''\sum_{k\in N_p}\overline{v}_{Fk,req}^{S}\right|\leq V_{F,\max}\,. \tag{3.22}$$

Using the same procedure adopted for Strategy 2, one can calculate the explicit expression of c'', which is as follows:

$$c''=\frac{\sqrt{b_1^2-b_2b_0}-b_1}{b_2}\,. \tag{3.23}$$

where

$$b_0=\left|\overline{v}_{F1,ref}^{S}+\sum_{k\in N_n}\overline{v}_{Fk,req}^{S}\right|^{2}-V_{F,\max}^{2}\,. \tag{3.24}$$

$$b_1=2\left(\overline{v}_{F1,ref}^{S}+\sum_{k\in N_n}\overline{v}_{Fk,req}^{S}\right)\cdot\sum_{k\in N_p}\overline{v}_{Fk,req}^{S}\,. \tag{3.25}$$

$$b_2=\left|\sum_{k\in N_p}\overline{v}_{Fk,req}^{S}\right|^{2}. \tag{3.26}$$

A value for coefficient c'' exits if the discriminant $b_1^2 - b_2 b_0$ is positive or zero, and the denominator b_2 is different from zero. The former condition is verified if $\left|\overline{v}_{F1,ref}^{S}\right|$ is lower than $V_{F,\max}$, the latter is verified because b_2 is usually a positive number different from zero.

A graphical analysis of difference between strategy 2 and 3 can be useful to highlight the benefits introduced by the evaluation of the relation (3.21) in the saturation algorithm.

Let us consider the same condition used before, when the total output voltage is composed by the first, the fifth and the seventh harmonics. In Fig. 3.6(a) the same condition of requested voltage over the boundary is limited by strategy 2 in Fig. 3.6(b) and strategy 3 in Fig. 3.6(c).

In strategy 2, all the high frequency harmonics, fifth and seventh in this case, are reduced by the same factor given by (3.18), so that the output voltage $\left|\overline{v}_{F,ref}^{S}\right|$ is brought inside the voltage limit imposed by $V_{F,\max}$, while the fundamental harmonic is unaffected as explained. Strategy 3, instead, reduces just the harmonics whose contribute increases the total output

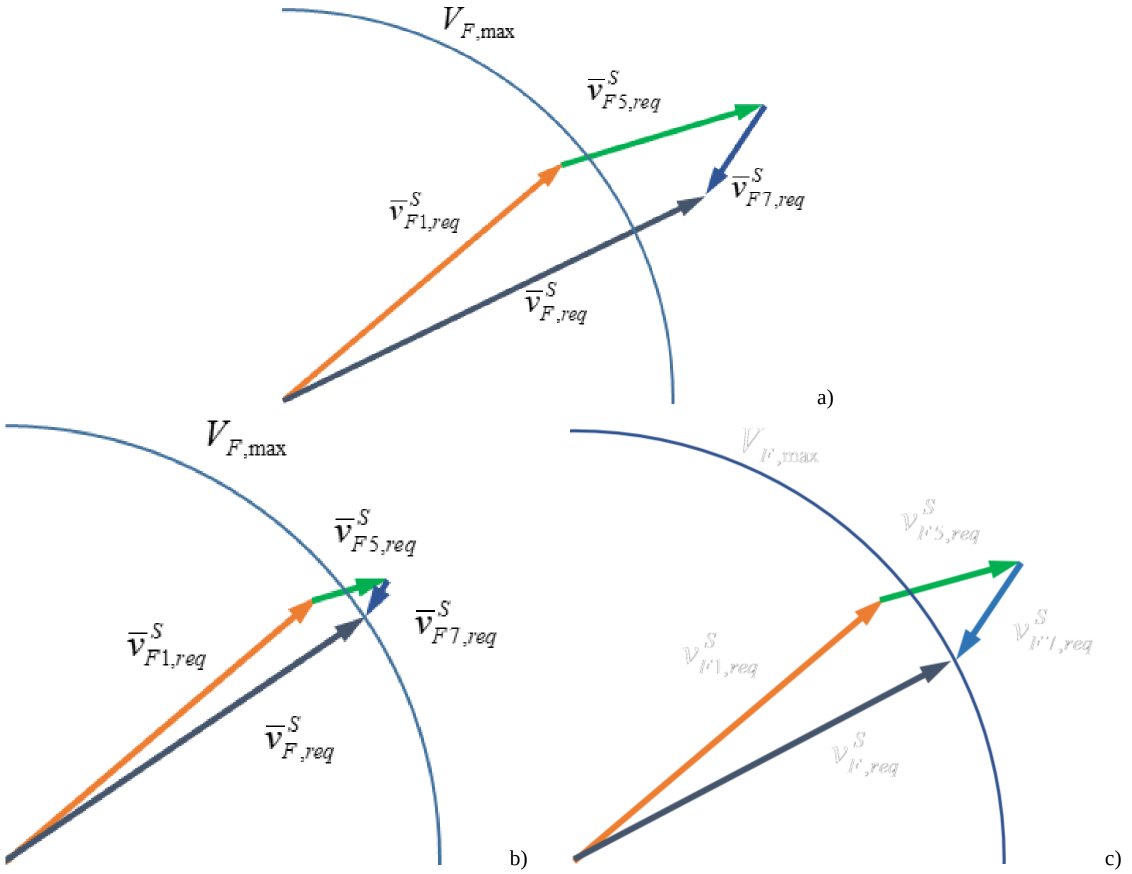

Fig. 3.6. Space vector representation of the total output voltage over the voltage limit a) constrained by strategy 2 b) and by strategy 3 c).

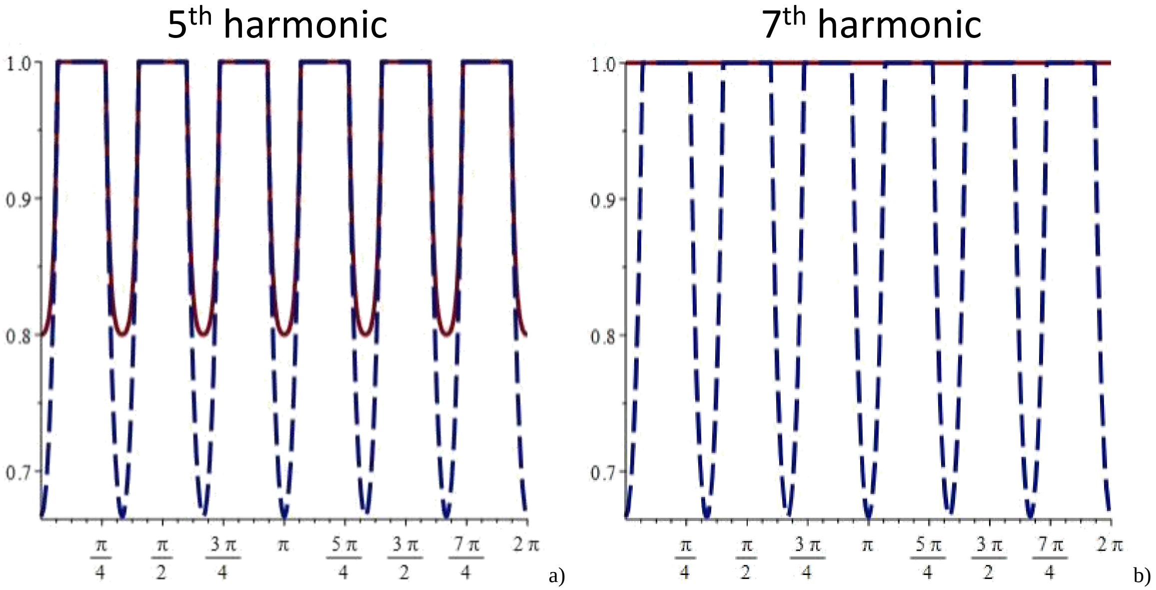

Fig. 3.7. Normalized magnitude of 5th a) and 7th b) harmonics as function of fundamental phase with the second strategy, blue dash line, and the third strategy, red solid line.

voltage according to (3.21), which in Fig. 3.6(a) is just the fifth harmonic. Due to the fact that the seventh harmonic is not reduced by strategy 3, all “its magnitude” contributes to reduce $\left|\bar{v}^{S}_{F,ref}\right|$, hence the reduction of the fifth harmonic has to be less consistent to bring the total voltage inside the constraint.

This can be also be appreciated in Fig. 3.7, where the magnitude of the fifth and seventh harmonics, normalized to the corresponding unconstrained request, are plotted as function of the phase over a fundamental period. The 7th harmonic, which is not reduced by strategy 3 (red solid line) in Fig. 3.7(b), allows one to have a further voltage margin, compared with strategy 2 (blue dash line), which can be allocated for the other harmonics that need to be saturated, as the 5th harmonic, Fig. 3.7(a).

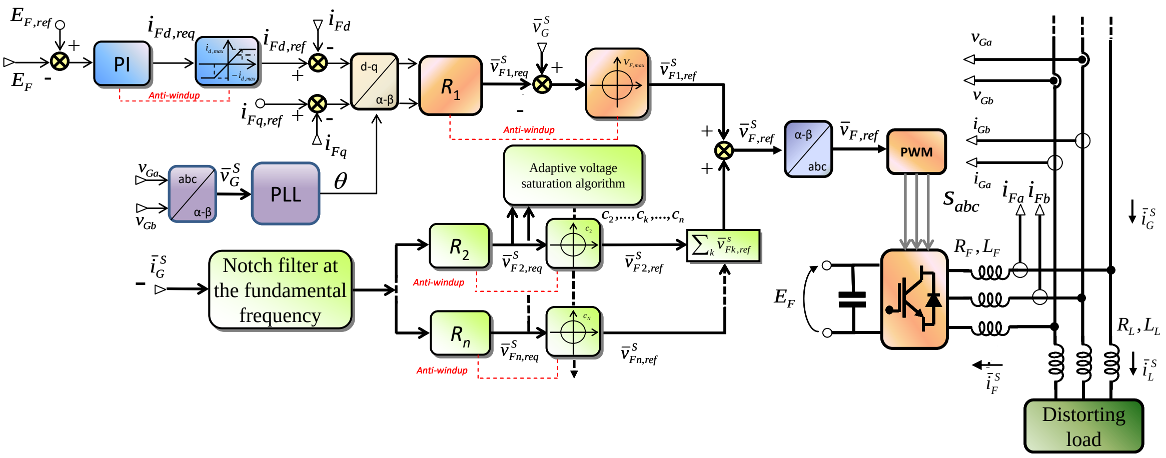

Fig 3.8. APF control scheme with adaptative voltage saturation.

D. *Experimental Results*

By using the same laboratory setup as for all the grid connected applications covered so far, some experimental results have been obtained. The parameters of the drive are listed in TABLE 2. The control system of the filter includes an array of proportional-resonant regulators to cancel the odd harmonics of the grid current from the 3rd one up to the 19th one and is shown in Fig 3.8.

Fig 3.9 shows the behavior of the grid currents for Strategies 1, 2, and 3, when the DC-link voltage is not sufficient to generate the requested compensation voltage. The grid currents are shown in the upper part of all figures. In the lower part, there are two sub-figures showing the details of the current waveforms without and with voltage saturation. Initially, the APF operates in normal conditions, and the THD of the grid current is just below 3%. Afterwards, a reduction by 15% in the DC-link voltage is caused to force the saturation of the voltage regulators. As can be seen, a distortion of the grid current appears. However, the effect of the reduction in the voltage level depends on the saturation strategy.

Although Strategy 1 ensures that the coefficient *c* is constant over time, the resulting current is visibly distorted, and its waveform is nearly trapezoidal.

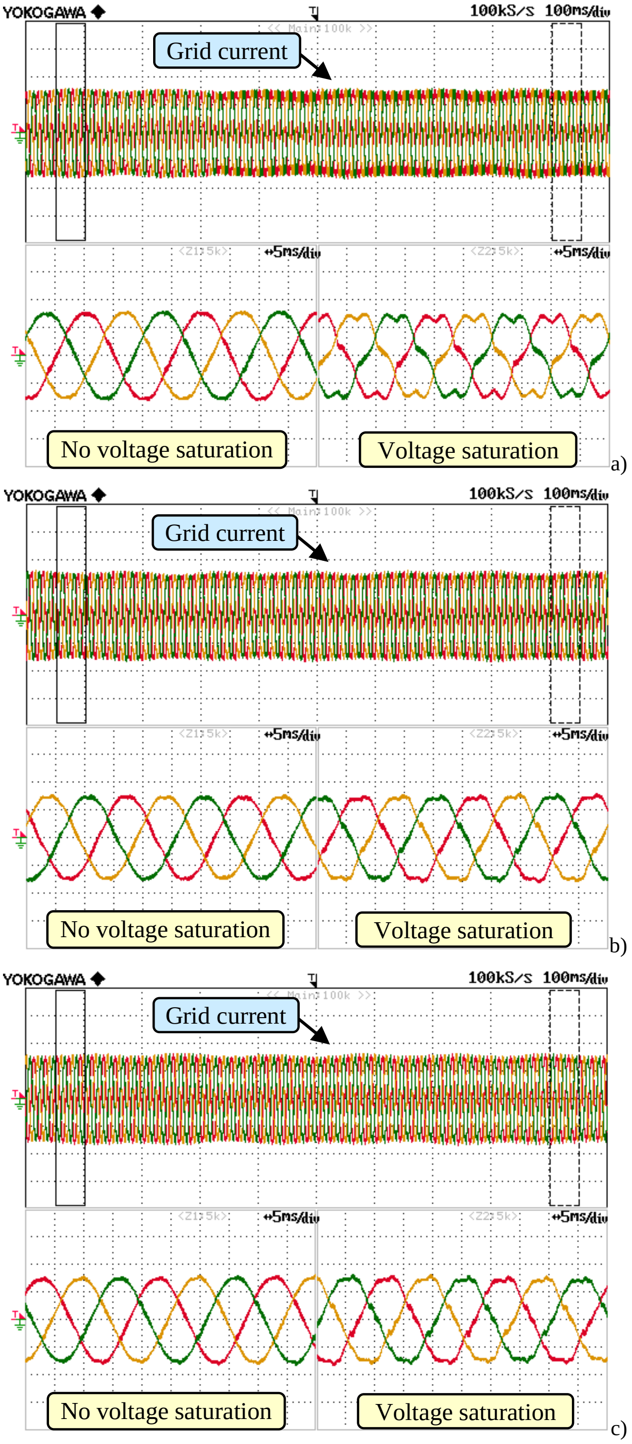

Fig 3.9. Waveforms of the grid current when the requested voltage is greater than the available voltage. a) Strategy 1. b) Strategy 2. c) Strategy 3. Scale: current (2 A/div).

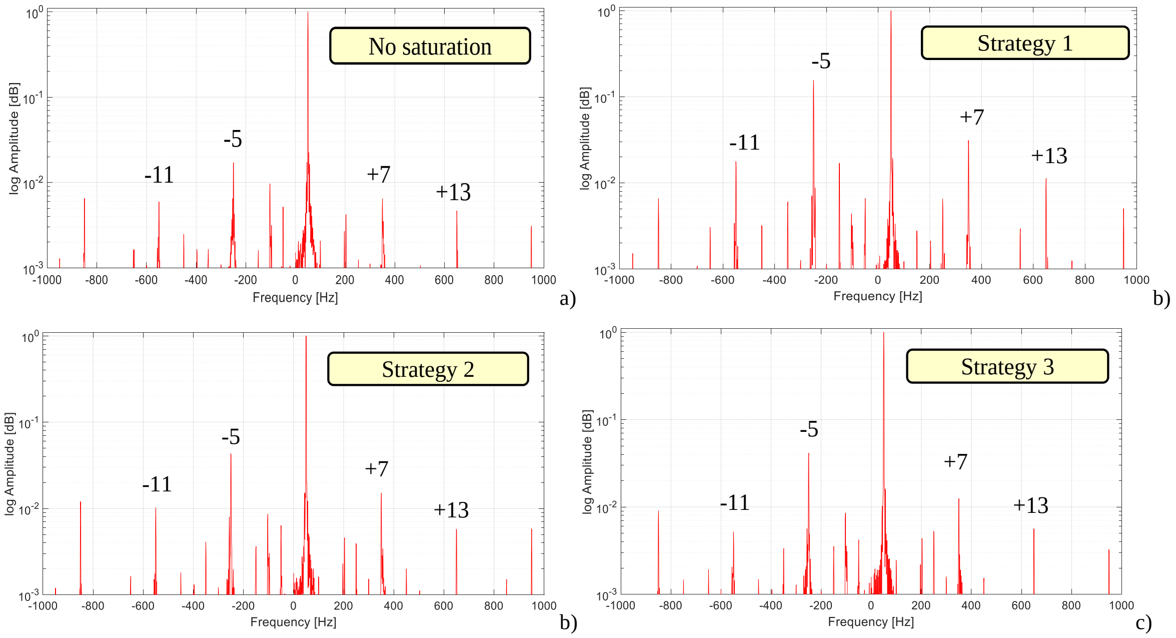

Fig 3.10. Waveforms of the grid current when the requested voltage is greater than the available voltage. a) Strategy 1. b) Strategy 2. c) Strategy 3. Scale: current (2 A/div).

Conversely, Strategy 2 and 3 exhibit better performance and the distortion of the grid current is less perceptible. Overall, all strategies ensure a stable operation of the converter.

Fig 3.10 shows the spectrum of the space vector of the grid current in different operating conditions. If the total output voltage is below the saturation threshold, the current harmonics are negligible, as shown in Fig 3.10 (a). Conversely, if the DC voltage becomes 85% of the rated value, some harmonics with orders -5, +7, -11, and +13 appear in the grid current.

Comparing Fig 3.10. 4(b) and 4(c) leads to the conclusion that the amplitude of the harmonics generated by Strategy 2 is always lower than that of the harmonics generated by Strategy 1. In addition, Strategy 3 seems better than Strategy 2 because the harmonics with orders -5 and -11 have smaller amplitude.

The curves of Fig 3.11 show the THD of the grid current when the DC-link voltage further decreases from 85% to 80% of the rated voltage. The THD of Strategies 2 and 3 does not change appreciably as long as the DC-link voltage is greater than 85% of the rated voltage, but below this threshold value, the performance reduction is more significant. Conversely, Strategy 1 sees a linear increase in the THD as long as the DC-link voltage decreases.

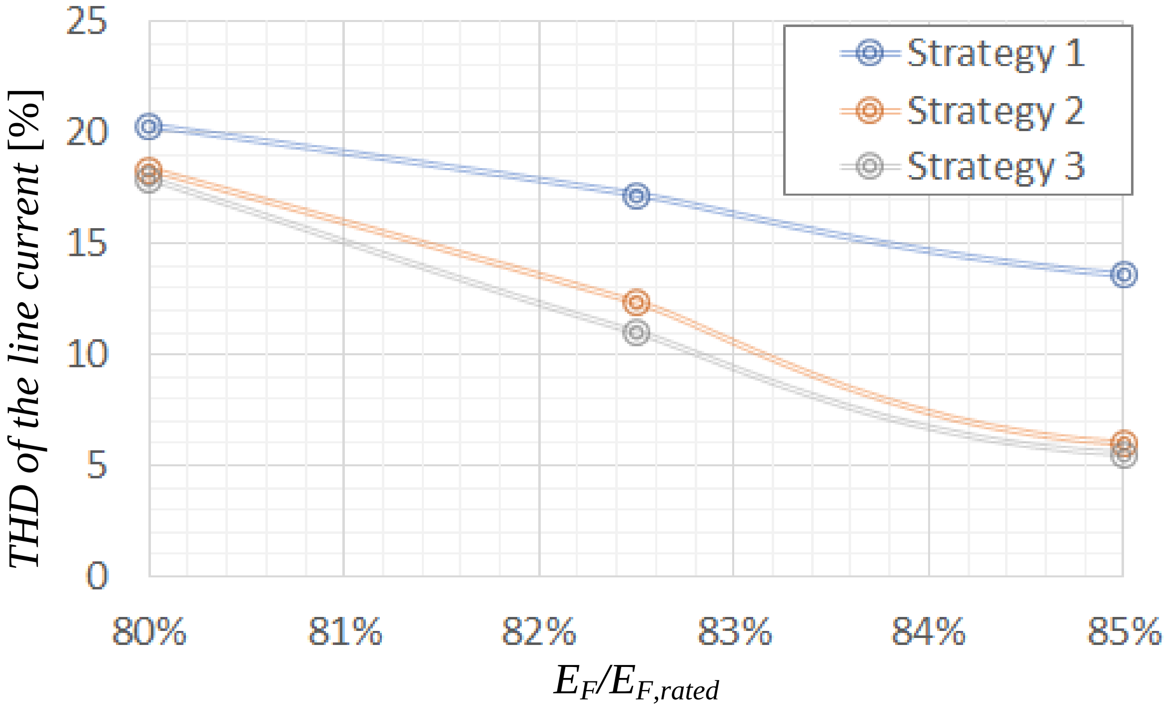

Fig 3.11. THD of the grid currents when the DC-link voltage decreases causing voltage saturation.

Part II

OPEN-END WINDING MOTORS

Chapter 4

OPEN-END WINDING MOTORS DRIVE

4.1 INTRODUCTION

High performance electric machines require the use of permanent magnets in somarium-cobalt or neodymium-iron-boron, i.e. based on rare-earth elements [20] - [21]. Although the 17 chemical elements belonging to the "rare-earths" are widespread throughout the Earth's crust, deposits with sufficient concentration for exploitation are few in number. This shortage makes uncertain not only the future of the green economy and consumer electronics, but also of the renewable energies. Until the 1950s, most of the rare earths came from India and Brazil, then the dominance of exports was led by South Africa until the 1980s, when for a short time the US became the major producers. With the new millennium, China has taken a turnaround in the rare earth market, dropping prices to become virtually a monopolist and today they cover 95% of world production. However, in recent years, China has imposed on its rare earth industry increasingly stringent production and export ceilings, behind the official objective of protecting the environment, causing the explosion of prices of many minerals, which have increased tenfold the levels of 2010, before falling again. Although the Chinese decisions have been severely criticized by the World Trade Organization (WTO), it is undeniable that the growing use has made rare earths a first-rate geostrategic importance, turning them into an inescapable political lever. To date, rare earths are on the list of "critical raw materials" compiled by the European Commission in 2014. A recent report by the European Commission's Joint Research Center examined the rare metal requirements of the 6 low-carbon technologies on which European Strategic Energy Technology Plan (SET-Plan) is founded: nuclear, wind, solar, CO2 capture, biomass energy and electricity grids. The JRC study showed that 5 metals (indium, gallium, tellurium, neodymium and dysprosium) will have supply problems, putting at risk technological sectors such as photovoltaics, electric traction and wind power. The JRC recommends, first of all, to promote the search for alternative solutions for the most efficient use of these elements. One of the salient aspects highlighted by the European Commission is the forecast for the development of demand for rare earths in the coming years. The spread of electric cars could drive the demand for rare earths to double-digit growth levels.

For these reasons, the scientific community has considered new configurations of electric drives for high speed applications that do not rely on permanent magnets.

Some special configurations of electric drives, based on wound rotor induction machines, have already been investigated. It has been verified that the performance of the machine improves if it is fed from stator and rotor sides by two separate inverters. The rotor-side inverter allows compensating the rotor reactive power and introduces an additional degree of freedom in the control scheme [22]- [23]- [24]. Furthermore, if the rotor-side inverter is floating, it can be embedded in the rotor without using shaft brushes [25], which may limit the speed range. The same principle can be applied to squirrel-cage rotor induction machines with open-ended stator windings. Initially, the open-end configuration was developed for permanent-magnet synchronous machines to reduce the current ripple in high-speed applications [26]- [27]- [28], but later it was considered also for induction machines. The stator phases can be fed by inverters located at both sides of the stator windings, and the energy may come from a common dc link, from two separate dc links, or from a dc link and a floating bridge, as shown in Fig 4.1. Although all these topologies may be suitable for specific applications, this PhD work focuses only on the last one, because it avoids the

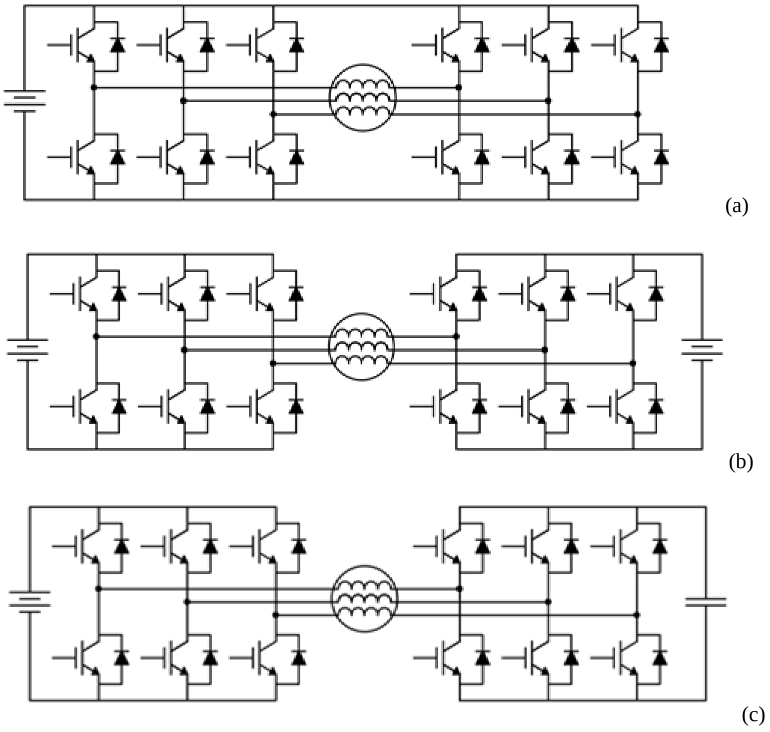

Fig 4.1. Schemes based on dual inverters for open winding machines.

problem of the circulation of the zero-sequence current and does not need separate dc sources, which may be not available. In [29] and [30], it is shown that the floating inverter offers many other benefits, such as the compensation of the reactive power of zero-sequence currents.

The voltage boost can improve the motor operation and extend the speed range. In [31], the floating inverter is used to increase the total voltage applied to an integrated starter-generator for automotive applications.

The analysis of the torque capability of the motor is presented in [32], which is focused specifically on the field-weakening speed range, whose extension is proved dependent on the voltage of the secondary DC-link bus.

As regards to the low speed range, in [33], the multilevel behavior of the dual inverter system is analyzed and a modulation technique that uses the redundant switching states to control the voltage of the floating capacitor is developed. The efficiency of the system is analyzed in [34].

After focusing on the control problem, discussed in [29]- [31], [33], and [34], the international research has tried to introduce some changes in the topology of the drive or exploiting the multilevel structure of the converters. The control of the floating bridge to generate a multilevel stator voltage is also investigated in [35] and [36]. Other solutions, based on three-level flying capacitor inverters, are proposed in [37] and [38] to improve the current quality. In [39], a square wave controller is proposed for high-speed applications to overcome the limitations of traditional pulse-width modulators. The research community has recently also explored some unconventional solutions. In [40], the analysis is focused on a structure that is similar to that shown in Fig 4.1(c), but it includes a ground connection originating from the middle point of the secondary dc-bus, so zero-sequence currents are allowed to circulate. Finally, in [41], the feasibility of a multiphase drive is assessed with positive results.

4.2 MATHEMATICAL MODEL FOR AN OPEN-END WINDING MOTOR

A. *Machine and Floating Bridge Capacitor Equations*

With reference to Fig. 4.2, the voltage applied to the motor is:

$$\overline{v}_S = \overline{v}_A - \overline{v}_B \tag{4.1}$$

where $\overline{v}_S$, $\overline{v}_A$ and $\overline{v}_B$ are the voltage space vectors of motor, inverter A and inverter B respectively.

The mathematical model of an electrical motor, in a d-q reference frame aligned generally with the rotor flux, independently for the type of motor, can be written as follows:

$$v_{Sd} = R_S i_{Sd} - \omega \varphi_{Sq} + \frac{d\varphi_{Sd}}{dt} \tag{4.2}$$

$$v_{Sq} = R_S i_{Sq} + \omega \varphi_{Sd} + \frac{d\varphi_{Sq}}{dt} \tag{4.3}$$

$$\varphi_{Sd} = L_{Sd} i_{Sd} + \varphi_e \tag{4.4}$$

$$\varphi_{Sq} = L_{Sd} i_{Sq} \tag{4.5}$$

$$T = \frac{3}{2} p \left(j \overline{\varphi}_S \right) \cdot \overline{i}_S . \tag{4.6}$$

where ω is the angular frequency of the rotor speed in electric radians, *p* is the number of pole pairs, v_{Sd} and v_{Sq} are the d-q components of the stator voltage vector $\overline{v}_S$, i_{Sd} and i_{Sq} are the d-q components of the stator current vector $\overline{i}_S$, φ_{Sd} and φ_{Sq} are the d-q components of the stator flux vector $\overline{\varphi}_S$, φ_e is the excitation flux, *T* is the electromagnetic torque, L_{Sd} and L_{Sq} are the stator inductances along d and q axes respectively, R_S is the stator resistance and "·" is the dot product, defined as the sum of the products of the corresponding d and q components of the first and second vector.

If the inverter losses are neglected, the rate of change of the electromagnetic energy stored in the floating capacitor *C* is equal to the instantaneous power exchanged by inverter B:

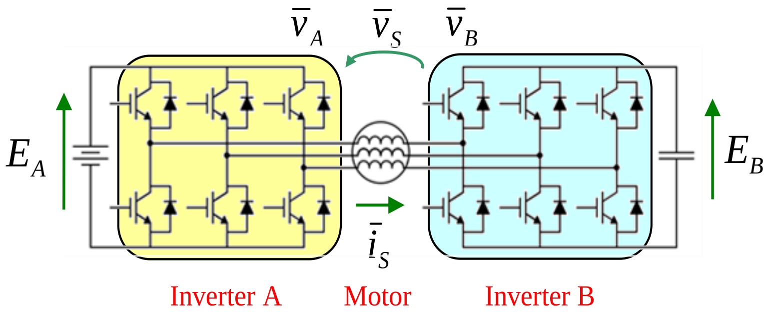

Fig. 4.2. Schematic diagram of the open-end winding motor fed by inverter A and inverter B with a floating capacitor.

$$\frac{d}{dt}\left(\frac{1}{2}CE_B^2\right)=\frac{3}{2}\overline{i}_S\cdot\overline{v}_B \tag{4.7}$$

where E_B is the DC-link voltage of inverter B.

It is useful to express $\overline{v}_B$ as the sum of two components, v_B^p and v_B^q, respectively parallel and orthogonal to $\overline{i}_S$, which can be rewritten as follows:

$$\overline{v}_B=\left(v_B^p+jv_B^q\right)\frac{\overline{i}_S}{\left|\overline{i}_S\right|}. \tag{4.8}$$

In this reference frame, (4.7) becomes:

$$\frac{d}{dt}\left(\frac{1}{2}CE_B^2\right)=\frac{3}{2}\left|\overline{i}_S\right|v_B^p \tag{4.9}$$

which shows that the electromagnetic energy stored in the floating capacitor C, and consequently its voltage, depends solely on the parallel component of $\overline{v}_B$ to the stator current.

At steady state the DC-link voltage of the floating capacitor bridge should be constant. Consequently, (4.9) leads to the conclusion that

$$v_B^p=0. \tag{4.10}$$

Equation (4.10) means that the voltage vector $\overline{v}_B$ at steady state is orthogonal to the stator current vector. By substituting (4.10) in (4.8), it is possible to find the following steady-state expression of $\overline{v}_B$:

$$\overline{v}_B=v_B^q\frac{j\overline{i}_S}{\left|\overline{i}_S\right|}. \tag{4.11}$$

Therefore, orthogonal component v_B^q is a degree of freedom that can be used to control the reactive power of the drive. The use of the variable v_B^q, instead of the vector $\overline{V}_B$, allows reducing the complexity of the optimization problem.

B. *Voltage and Current Constraints*

The torque capability of the drive is limited by the rated thermal current of the machine and the rated current of the inverters. For the sake of simplicity it is assumed that the maximum current of the converters and the machine is represented by only one value, I_{max}.

$$\left|\overline{i}_S\right| \le I_{\max} . \tag{4.12}$$

In addition, at high speed, the machine behavior is limited by the available voltage of inverters A and B, i.e,

$$\left|\overline{v}_A\right| \le V_{A,\max} \tag{4.13}$$

$$\left|\overline{v}_B\right| \le V_{B,\max} \tag{4.14}$$

where the upper bounds $V_{A,max}$ and $V_{B,max}$ depend on the dc-bus voltages E_A and E_B and on the modulation strategies of the inverters. If space vector modulation or pulse-width modulation with third-harmonic injection are used, the maximum voltages are

$$V_{A,\max} = \frac{E_A}{\sqrt{3}} \tag{4.15}$$

$$V_{B,\max} = \frac{E_B}{\sqrt{3}} . \tag{4.16}$$

Voltage E_A is fixed by the input power source. Conversely, E_B is a design choice, which may be equal or even greater than E_A, depending on the blocking voltage of the switches of converter B.

In the following, it is assumed that E_B is much greater than E_A, to take advantage of the voltage boost that the floating inverter can provide. The ratios E_B/E_A=2 and E_B/E_A=0.5 produce a symmetric set of voltage vectors. For example, Fig. 4.3 shows the set of voltage vectors in the stator reference frame that may be generated by inverters A, B and the dual inverter system when E_B=2E_A (the superscript "^{S}" identifies variables in the stator reference frame). The vertexes of the hexagons represent the admissible voltage vectors. As can be

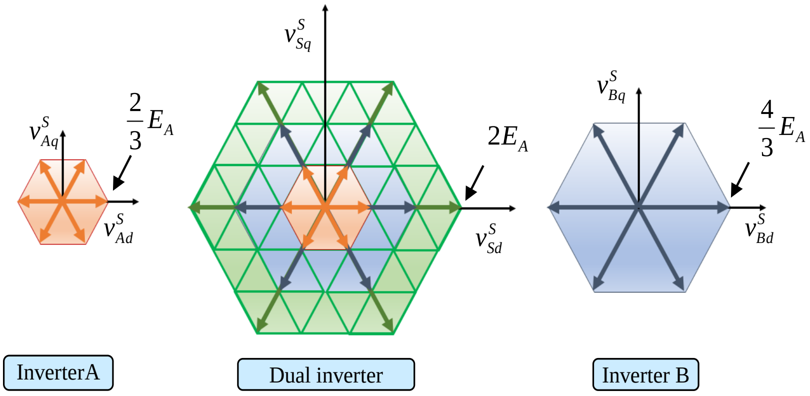

Fig. 4.3. Voltage vectors, in the stator reference frame, generated by inverter A, the dual inverter system and inverter B when E_B is $2E_A$.

seen, as regards the dual inverter system, they are equally distributed and the resulting grid of configurations is the same that can be found for a 4-level multiphase inverter fed by a total DC link voltage equal to $3E_A$. A similar distribution of vectors can be found if E_B is equal to 0.5 E_A. However, in this case, the voltage boost would be limited, to the detriment of the performance, since the maximum stator voltage is half the previous one.

4.3 OPTIMIZATION OF THE DRIVE PERFORMANCE

A. *Optimization of the Mechanical Power*

The optimal control strategy of the drive should maximize the mechanical power delivered to the load and extend the constant-power speed range as much as possible.

The power balance of the drive is defined by the following expressions:

$$\bar{S}_S = \bar{S}_A - \bar{S}_B = P_S + jQ_S \tag{4.17}$$

$$P_S = P_A - P_B \tag{4.18}$$

$$Q_S = Q_A - Q_B \tag{4.19}$$

where $\bar{S}_S$, $\bar{S}_A$ and $\bar{S}_B$ are the apparent powers of the electrical motor, inverter A and inverter B respectively, P_S , P_A and P_B are respectively the active power of the electrical motor, inverter A and inverter B while Q_S, Q_A and Q_B the respective reactive power values. Equation (1.19) shows that it is possible to nullify the reactive power of inverter A through the reactive power flow of inverter B.

The active and reactive powers flowing through inverter A are equal to:

$$P_A = \frac{3}{2}\overline{v}_A \cdot \overline{i}_S \tag{4.20}$$

$$Q_A = \frac{3}{2}\overline{v}_A \cdot j\overline{i}_S \,. \tag{4.21}$$

Under the assumption that the converter losses are negligible, at steady state, the active power of inverter A is equal to the sum of Joule losses P_{Joule}, iron losses, P_{iron}, and the mechanical power delivered to the load, P_{mech}.

$$P_A = P_{Joule} + P_{iron} + P_{mech} \,. \tag{4.22}$$

The expression of the reactive power of inverter A can be found by combining (4.1) - (4.3), (4.11), (4.19) and (4.21).

$$Q_A = \frac{3}{2}\overline{v}_S \cdot j\overline{i}_S + \frac{3}{2}\overline{v}_B \cdot j\overline{i}_S \simeq \frac{3}{2}\left(j\omega\overline{\phi}_S\right) \cdot j\overline{i}_S + \frac{3}{2}v_B^q\left|\overline{i}_S\right| \,. \tag{4.23}$$

The first term in (4.23) is the reactive power exchanged by the motor, the second term is the reactive power exchanged by inverter B.

By squaring (4.20) and (4.21) and summing side by side, it turns out that

$$P_A{}^2 + Q_A^2 = \left(\frac{3}{2}\left|\overline{v}_A\right|\left|\overline{i}_S\right|\right)^2 . \tag{4.24}$$

In the field weakening speed region, v_A and i_S have to satisfy the constraints (4.12) - (4.13). Consequently, combining (4.22), (4.23) and (4.24), leads to the following inequality:

$$\left(P_{Joule} + P_{iron} + P_{mech}\right)^2 + Q_A^2 \le \left(\frac{3}{2}V_{A,\max}I_{\max}\right)^2 . \tag{4.25}$$

Inequality (4.25) shows that, to extend the range of the active power of inverter A, it is necessary to reduce its reactive power to a minimum.

Equating (4.23) to zero and solving for v_B^q leads to the following result:

$$v_{B,opt}^q = -\frac{\omega\overline{\phi}_S \cdot \overline{i}_S}{\left|\overline{i}_S\right|} \tag{4.26}$$

Combining (4.8), (4.9) and (4.26) allows finding the expression of $\overline{v}_B$ as a function of the rotor speed ω and of the motor state

$$\overline{v}_B = \left(\frac{d}{dt}\left(\frac{1}{3}CE_B^2\right) - j\,\frac{\omega\overline{\phi}_S \cdot \overline{i}_S}{\left|\overline{i}_S\right|}\right)\frac{\overline{i}_S}{\left|\overline{i}_S\right|}\,. \tag{4.27}$$

Equation (4.27) shows that $\overline{v}_B$ is orthogonal to the stator current at steady state. According to (4.14), $\overline{v}_B$ cannot be greater than $V_{B,max}$. In steady state condition, (4.27) is valid only if the following inequality is verified:

$$\frac{\left|\omega\overline{\phi}_S \cdot \overline{i}_S\right|}{\left|\overline{i}_S\right|} \leq V_{B,\max}\,. \tag{4.28}$$

If (4.28) is not satisfied, the expression for $\overline{v}_B$ becomes:

$$\overline{v}_B = j\left(\operatorname{sgn} v_{B,opt}^q\right)V_{B,\max}\,\frac{\overline{i}_S}{\left|\overline{i}_S\right|} \tag{4.29}$$

and the reactive power Q_A becomes different from zero and equal to:

$$Q_A = \frac{3}{2}\left(\ \omega\overline{\varphi}_S \cdot \overline{i}_S + \left(\operatorname{sgn} v_{B,opt}^q\right)V_{B,\max}\left|\overline{i}_S\right|\right). \tag{4.30}$$

In conclusion, choosing v_B^q according to (4.26) allows improving the performance of the drive because inverter A operates at unity power factor at any speed and its power capability can be fully exploited.

B. *Admissible Domain of the Stator Current*

Inequality (4.26) for inverter B can be rewritten as a function of the components i_{Sd} and i_{Sq} of the stator current vector by means of (4.4) - (4.5):

$$\begin{aligned} V_{B,\max} &\geq \frac{\left|\omega\overline{\phi}_S \cdot \overline{i}_S\right|}{\left|\overline{i}_S\right|} = \frac{\left|\omega(\varphi_{Sd} + j\varphi_{Sq})\cdot(i_{Sd} + ji_{Sq})\right|}{\left|\overline{i}_S\right|} = \\ &= \frac{\left|\omega(\varphi_{Sd}i_{Sd} + \varphi_{Sq}i_{Sq})\right|}{\left|\overline{i}_S\right|} = \frac{\left|\omega\left(\left(L_{Sd}i_{Sd} + \varphi_e\right)i_{Sd} + \left(L_{Sq}i_{Sq}\right)i_{Sq}\right)\right|}{\left|\overline{i}_S\right|} = \\ &= \frac{\left|\omega\left(L_{Sd}i_{Sd}^2 + \varphi_e i_{Sd} + L_{Sq}i_{Sq}^2\right)\right|}{\left|\overline{i}_S\right|}. \end{aligned} \tag{4.31}$$

It is useful to express the stator inductance along the d-q axes as a function of the magnetic anisotropy factor δ

$$\delta = \frac{L_{Sq}}{L_{Sd}}. \tag{4.32}$$

By substituting (4.32) in (4.31), the following expression can be found:

$$\frac{\left|\omega\left(L_S\left(i_{Sd}^2 + \delta i_{Sq}^2\right) + \varphi_e i_{Sd}\right)\right|}{\sqrt{i_{Sd}^2 + i_{Sq}^2}} \le V_{B,\max}. \tag{4.33}$$

Similarly, in steady state operating conditions, if the voltage drop due to the stator resistance is neglected, (4.13), combined with (4.1) - (4.5) and (4.27), leads to the following inequality for inverter A:

$$\begin{aligned}
V_{A,\max} &\ge \left| j\omega\bar{\varphi}_S + \bar{v}_B \right| = \left| j\omega\bar{\varphi}_S - j\,\frac{\omega\bar{\varphi}_S \cdot \bar{i}_S}{\left|\bar{i}_S\right|}\,\frac{\bar{i}_S}{\left|\bar{i}_S\right|} \right| = \\
&= \left|\omega\left((\varphi_{Sd} + j\varphi_{Sq}) - \frac{(\varphi_{Sd} + j\varphi_{Sq})\cdot(i_{Sd} + j i_{Sq})}{\left|\bar{i}_S\right|}\,\frac{(i_{Sd} + j i_{Sq})}{\left|\bar{i}_S\right|} \right)\right| = \\
&= \left|\omega\left((\varphi_{Sd} + j\varphi_{Sq}) - \frac{(\varphi_{Sd} i_{Sd} + \varphi_{Sq} i_{Sq})(i_{Sd} + j i_{Sq})}{\left|\bar{i}_S\right|^2} \right)\right| = \\
&= \frac{|\omega|}{\left|\bar{i}_S\right|^2}\left|\left((\varphi_{Sd} i_{Sq} - \varphi_{Sq} i_{Sd}) i_{Sq} + j(\varphi_{Sq} i_{Sd} - \varphi_{Sd} i_{Sq}) i_{Sd}\right)\right| =
\end{aligned}$$

$$\begin{aligned}
&= \frac{|\omega|}{\left|\bar{i}_S\right|^2}\sqrt{\left((\varphi_{Sd} i_{Sq} - \varphi_{Sq} i_{Sd})^2 i_{Sq}^2 + (\varphi_{Sq} i_{Sd} - \varphi_{Sd} i_{Sq})^2 i_{Sd}^2\right)} = \\
&= \frac{|\omega|}{\left|\bar{i}_S\right|^2}\sqrt{\left((\varphi_{Sd} i_{Sq})^2 + (\varphi_{Sq} i_{Sd})^2 - 2(\varphi_{Sd} i_{Sq})(\varphi_{Sq} i_{Sd})\right)\left|\bar{i}_S\right|^2} = \frac{|\omega|}{\left|\bar{i}_S\right|}\sqrt{(\varphi_{Sd} i_{Sq} - \varphi_{Sq} i_{Sd})^2} = \\
&= \frac{|\omega|}{\left|\bar{i}_S\right|}(\varphi_{Sd} i_{Sq} - \varphi_{Sq} i_{Sd}) = \frac{|\omega|}{\left|\bar{i}_S\right|}\left(\left(L_S i_{Sd} + \varphi_e\right) i_{Sq} - \left(\delta L_S i_{Sq}\right) i_{Sd}\right)
\end{aligned}$$

which leads to the following expression for the voltage constraint of inverter A:

$$\frac{\left|\omega i_{Sq}\right|}{\left|\bar{i}_S\right|}\left(\left(1-\delta\right) L_S i_{Sd} + \varphi_e\right) \le V_{A,\max}. \tag{4.34}$$

It is worth noting that (4.34) is proportional to the torque expression, given by (4.6) by means of (4.4) – (4.5) and (4.32):

$$T = \frac{3}{2} p i_{Sq} \left(\left(1-\delta\right) L_S i_{Sd} + \varphi_e \right). \tag{4.35}$$

Therefore, combining equations (4.34) and (4.35) one comes to following equality:

$$\frac{3}{2} V_{A,\max} \left| \bar{i}_S \right| \geq \frac{3}{2} T \omega \tag{4.36}$$

which confirms that, if Joule and iron losses are neglected and constraint (1.14) is satisfied, the electrical apparent power available at the AC side of inverter A is entirely used to generate active power at the motor output.

C. *Resulting Speed Ranges*

Equation (4.36) is valid for each rotor speed ω for which (4.28) is satisfied. In nominal condition it becomes:

$$\frac{3}{2} V_{A,\max} I_{\max} = \frac{3}{2} T_{\max} \omega_{base} . \tag{4.37}$$

In the same working condition, for a single inverter system, the relation between the electrical power delivered by the inverter and the electrical output power of the motor is:

$$\frac{3}{2} V_{A,\max} I_{\max} \cos \varphi_{base} = \frac{3}{2} T_{\max} \omega'_{base} \tag{4.38}$$

where φ is the phase shift between inverter AC output voltage and the current flowing in the stator windings.

Since the maximum torque T_{max} value is not affected by the dual inverter configuration with a floating bridge, from (4.37) and (4.38) it is possible to find the relation between the base speeds of the single and dual inverter configuration:

$$\omega'_{base} = \omega_{base} \cos \varphi_{base} \tag{4.39}$$

which shows that the base speed of a single inverter drive is lower than that of a dual inverter drive and proportional to the input power factor at the base speed.

Above the base speed the available voltage is not sufficient to compensate the back electromagnetic force and it is therefore necessary to weaken the stator flux. As consequence it is not possible to produce the maximum torque, which starts to decrease as the rotor speed increases. This speed range, above the base speed, is characterized by a nearly constant power level working condition.

Inequality (4.25) shows that, if iron losses are neglected, the constant power speed range is maintained as long as the current is at a maximum and the reactive power of inverter A is zero. While the maximum current working condition depends on the control strategy used for the electrical motor available, the maximum speed achievable by the proposed drive when the inverter A operates at unity power factor can be found independently to the of motor.

If the current components i_{Sd}, i_{Sq} are rewritten in polar form,

$$i_{Sd} = I_{max} \cos\alpha \tag{4.40}$$

$$i_{Sq} = I_{max} \sin\alpha \tag{4.41}$$

the expression for the maximum speed with inverter A at unity power factor is obtained by substituting (4.40) and (4.41) in (4.33)

$$\omega_{pow} = \frac{V_{B,max}}{\left| L_S I_{\max} \left(\cos^2\alpha + \delta \sin^2\alpha \right) + \varphi_e \cos\alpha \right|} . \tag{4.42}$$

Above the rotor speed given by (4.42), it is still possible to accelerate by losing the unity power factor condition. The maximum speed is reached when the torque, hence the mechanical power, reaches zero. In this condition, combining (4.25) and (4.30), by neglecting the joule and iron losses, the reactive power can be rewritten as follows:

$$\left| Q_A \right| = \frac{3}{2} \left| \omega \bar{\phi}_S \cdot \bar{i}_S + \left(\operatorname{sgn} v^q_{B,opt} \right) V_{B,\max} \left| \bar{i}_S \right| \right| = \left(\frac{3}{2} V_{A,\max} I_{\max} \right) . \tag{4.43}$$

Substituting (4.4), (4.5), (4.40) and (4.41) in (4.43) leads to the following expression for the maximum speed of a dual inverter drive:

$$\omega_{\max} = \frac{V_{A,max} + V_{B,max}}{\left| L_S I_{\max} \left(\cos^2\alpha + \delta \sin^2\alpha \right) + \varphi_e \cos\alpha \right|} . \tag{4.44}$$

Equation (4.44) shows how the maximum speed for the dual inverter drive is obtained when $\bar{v}_A$ and $\bar{v}_B$ are summed with the same phase, hence the resulting vector $\bar{v}_S$ is orthogonal to the current space vector $\bar{i}_S$.

Chapter 5

INDUCTION MOTOR WITH OPEN-END WINDINGS

Although induction machines are not as efficient as PM machines and the torque density is lower, their robustness, cost and overload capability are appealing in mass-production applications [21]. Since the lower performance of induction motors in comparison to PM motors partially depends on the lower power factor, the improvement in performance achieved by adopting an open-ended stator winding is gaining more attention.

5.1 SYSTEM MODEL

A. Machine Equations and Admissible Stator Current Domain

The model of the induction machine can be described by the following equations written in a reference frame synchronous with the d-axis aligned to the rotor flux:

$$\bar{v}_S = R_S \bar{i}_S + j\omega\bar{\phi}_S + \frac{d\bar{\phi}_S}{dt} \tag{5.1}$$

$$\varphi_{Sd} = \sigma L_S i_{Sd} + \frac{M}{L_R}\varphi_{Rd} \tag{5.2}$$

$$\varphi_{Sq} = \sigma L_S i_{Sq} \tag{5.3}$$

$$\varphi_{Rd} = \frac{M}{1+\tau_R s} i_{Sd} \tag{5.4}$$

$$\varphi_{Rq} = 0 \tag{5.5}$$

$$T = \frac{3}{2} p \frac{M}{L_r} i_{Sq}\varphi_{Rd} \tag{5.6}$$

where p is the pole pairs number, ω is the angular frequency of the rotor flux vector, $\bar{v}_S$ is the stator voltage, $\bar{i}_S$ is the stator current, $\bar{\varphi}_S$ is the stator flux vectors, L_S and M are the self- and mutual inductances, τ_R is the rotor time constant , φ_{Rd} and φ_{Rq} are the d-q components of the rotor flux and σ is the leakage coefficient, defined as:

$$\sigma = 1 - \frac{M^2}{L_S L_R} . \tag{5.7}$$

It can be seen that the induction mathematical model (5.1) – (5.6) is equal to the one expressed by equations (4.2) – (4.6) for a generic electrical motor if the following equality are assumed:

$$L_{Sd} = L_{Sq} = \sigma L_S \tag{5.8}$$

$$\varphi_e = \frac{M}{L_R} \varphi_{Rd} . \tag{5.9}$$

However, φ_{Rd} is a low-pass function of i_{Sd} as written in (5.4), making the model more complicated in comparison to permanent magnet machines.

Some simplification can be made to this model by considering the steady state condition. Equations (5.2), (5.4) and (5.6) become:

$$\varphi_{Sd} = L_S i_{Sd} \tag{5.10}$$

$$\varphi_{Rd} = M i_{Sd} \tag{5.11}$$

$$T = \frac{3}{2} p L_S \left(1 - \sigma\right) i_{Sq} i_{Sd} . \tag{5.12}$$

The mathematical model of the induction machine at steady state can be found by replacing in (4.2) – (4.6) the following relationships:

$$L_{Sd} = L_S \tag{5.13}$$

$$L_{Sq} = \sigma L_S \tag{5.14}$$

$$\varphi_e = 0 . \tag{5.15}$$

It can be seen that the model of the induction motor (5.1) – (5.6) is equivalent with that of a salient machine.

It is straightforward to find the voltage constraints for inverter A and inverter B for an induction motor with open-end windings by substituting (5.13) – (5.15) in (4.33) and (4.34):

$$L_S \frac{\left| \omega \left(i_{Sd}^2 + \sigma i_{Sq}^2 \right) \right|}{\sqrt{i_{Sd}^2 + i_{Sq}^2}} \le V_{B,\max} \tag{5.16}$$

$$L_S\left(1-\sigma\right)\frac{\left|\omega i_{Sd} i_{Sq}\right|}{\sqrt{i_{Sd}^2+i_{Sq}^2}} \le V_{A,\max}\,. \tag{5.17}$$

The expression (5.17) of the voltage limit for inverter A is valid as long as (5.16) is verified, otherwise (5.17) should be replaced by the following inequality,

$$\left| j\omega\bar{\phi}_S + j(\operatorname{sgn} v_{B,opt})V_{B,max}\frac{\bar{i}_s}{\left|\bar{i}_s\right|}\right| \le V_{A,max}\,. \tag{5.18}$$

B. *Drive Performance Improvements*

Fig. 5.1 graphically shows the meaning of the inequalities (5.16) - (5.17) for two values of ω, ω_{base} and ω_{pow}, which represent the initial and final speeds of the constant power speed range.

As long as the angular frequency increases, inequality (5.16) produces a set of curves, similar to hyperbolae in Fig. 5.1(a), which tend to become smaller. These curves are referred to as "voltage limit A" in Fig. 5.1.

Similarly, (5.17) generates a set of curves, formed by two lobes, which becomes smaller as long as the angular frequency increases. These curves are referred to as "voltage limit B" in Fig. 5.1.

For the sake of correctness, in Fig. 5.1(b), (5.16) has been replaced by (5.18) for operating states that do not satisfy (5.17). Consequently, the constant-voltage hyperbolae of inverter A have been replaced by closed curves.

Overall, the admissible operating states in Fig. 5.1(b) and Fig. 5.1(c) are those in the dashed areas, satisfying the voltage constraints (5.18) and (5.17), and not exceeding the rated magnetizing current $I_{Sd,rated}$.

The graphical representation of Fig. 5.1 can be used to identify the operating conditions corresponding to the maximum torque capability, since a constant-torque curve in the i_{Sd} - i_{Sq} plane is represented by a hyperbola. The closer the hyperbola is to the origin, the lower the torque.

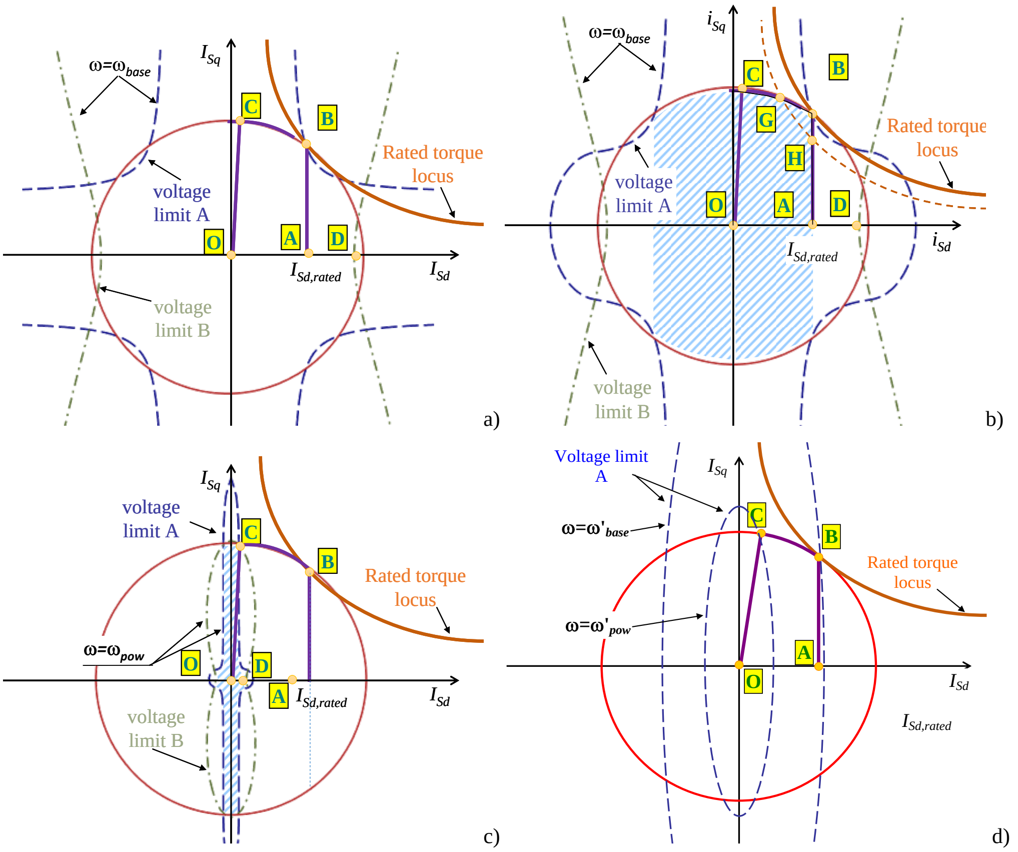

Fig. 5.1. Representation of the motor operating conditions in the plane i_{Sd}-i_{Sq} for a dual inverter drive (a)-(b)-(c) and a single inverter drive (d). (a) The voltage constrain of inverter A is plotted without considering (30) and ω=ω_{base} (b) The voltage constraint of inverter A is plotted considering (30) and ω=ω_{base}. (c) The voltage constraint of inverter A is plotted considering (30) and ω=ω_{pow}.

For example, Fig. 5.1(b) represents the admissible operating conditions (dashed area constrained by the current limit, the voltage limits of inverters A and B, and the limit of the magnetizing current) when the speed is equal to the base speed. Two different torque loci are represented. The first one, drawn in solid line, passes through point B, and the second one, drawn in dashed line, passes through points G and H. In the operating conditions represented by the points of arc G-H the torque has the same value. It can be easily understood that the torque locus passing through G-H is generated by a torque value that is lower than that of the torque passing through B. Following this line of reasoning, it can be proved that the maximum torque at the base speed is produced when the drive operates in point B (rated torque).

Analyzing Fig. 5.1 it is possible to conclude that the motor operation can be divided in three speed ranges.

Below the base speed, the maximum torque is represented by point B (region I). The motor performance is limited by I_{max} and the rated magnetizing current $I_{Sd,rated}$. It is straightforward to find the expression of the base angular frequency combining (4.37) and (5.12), which is as follows:

$$\omega_{base} = \frac{V_{A,max}}{L_S\left(1-\sigma\right)\sqrt{I_{max}^2 - I_{Sd,rated}^2}} \frac{I_{max}}{I_{Sd,rated}} . \tag{5.19}$$

As long as the speed increases, the operating point corresponding to the maximum torque moves from B to C (region II). However, the position of point C is a function of $V_{B,\mathrm{max}}$. In fact, considering (4.12), (5.16) and (5.17) as equalities, and solving the resulting set of equations, one can find the coordinates of point C. If the current components i_{Sd}, i_{Sq} are rewritten in polar form as in (4.40) and (4.41), the resulting equation is:

$$\frac{1}{\tan\alpha} + \sigma\tan\alpha = \frac{V_{B,max}}{V_{A,max}}\left(1-\sigma\right). \tag{5.20}$$

Under the assumption that α is near $\pi/2$, it is possible to find an asymptotic solution of (5.20), which turns out to depend only on the ratio $V_{B,max}/V_{A,max}$ and on the parameter σ.

$$\tan\alpha = \frac{i_{Sq}}{i_{Sd}} \cong \frac{1-\sigma}{\sigma}\frac{V_{B,max}}{V_{A,max}} . \tag{5.21}$$

Finally, the maximum speed in region II, ω_{pow}, can be found from equation (4.42), obtained for any kind of motor, imposing the relations given by (5.13)-(5.15) for the induction motor

$$\omega_{pow} = \frac{V_{B,max}}{L_S I_{max}\left(\cos^2\alpha + \sigma\sin^2\alpha\right)} \cong \frac{V_{B,max}}{\sigma L_S I_{max}} . \tag{5.22}$$

It is worth noting that, despite α depends on $V_{B,max}/V_{A,max}$, (5.22) shows that ω_{pow} is little sensitive to the variation of $V_{A,max}$, and can be extended as desired by increasing $V_{B,max}$.

Above ω_{pow}, (region III), the speed is too high and the voltage is not sufficient to inject the maximum current in the motor while maintaining the unity power factor for inverter A. In Fig. 5.1 the operating states of region III are represented by segment C-O.

The base speed ω_{base} and the maximum speed of constant power speed range ω_{pow} can be used to find the rotor speed in electric radians ω_m by considering the rotor circuit equations:

$$0 = R_R \bar{i}_R + j\left(\omega - \omega_m\right)\bar{\varphi}_R + \frac{d\bar{\varphi}_R}{dt} \tag{5.23}$$

$$\bar{\varphi}_R = L_R \bar{i}_R + M \bar{i}_S \tag{5.24}$$

where L_R is the rotor self-inductance, $\bar{i}_R$ is the rotor current and $\bar{\varphi}_R$ the rotor flux.

In steady state condition it is straightforward to verify that

$$\omega_m = \omega - \frac{i_{Sq}}{\tau_R i_{Sd}}. \tag{5.25}$$

Substituting (5.19) and (5.22) in (5.25) one finds the following expression:

$$\omega_{m,base} = \frac{V_{A,max}}{L_S\left(1-\sigma\right)\sqrt{I_{max}^2 - I_{Sd,rated}^2}} \frac{I_{max}}{I_{Sd,rated}} \left(1 - \frac{L_S\left(1-\sigma\right)}{\tau_R} \frac{I_{max}}{V_{A,max}} \frac{I_{max}^2 - I_{Sd,rated}^2}{I_{max}^2}\right) \tag{5.26}$$

$$\omega_{m,pow} = \frac{V_{B,max}}{\sigma L_S I_{max}} \left(1 - \frac{L_S\left(1-\sigma\right)}{\tau_R} \frac{I_{max}}{V_{A,max}}\right) \tag{5.27}$$

where the slip for the two speeds, s_{base} and s_{pow} are highlighted and they are equal to

$$s_{base} = \frac{L_S\left(1-\sigma\right)}{\tau_R} \frac{I_{max}}{V_{A,max}} \frac{I_{max}^2 - I_{Sd,rated}^2}{I_{max}^2} \tag{5.28}$$

$$s_{pow} = \frac{L_S\left(1-\sigma\right)}{\tau_R} \frac{I_{max}}{V_{A,max}}. \tag{5.29}$$

For the sake of completeness, Fig. 5.1(d) shows the operating states of a single inverter drive under the same current and voltage constraints for inverter A. The constraint on the DC-link voltage is represented by an ellipse in i_{Sd} - i_{Sq} plane.

The subdivision of the admissible speed range into three parts is well-known for induction machines fed by a single inverter [42]- [43]. In Region I the operating states of the motor correspond to the points of segment A-B. At higher speeds, the size of the ellipse decreases and the operating point is forced to move from B to C, while the magnitude of the stator current remains constant (region II). In Region III the current progressively tends to zero as long as the speed increases.

The two paths ABCO of Fig. 5.1 (c) and (d) are similar, but there are some substantial differences. First of all, the angular frequencies ω'_{base} in point B and ω'_{pow} in point C are lower than ω_{base} and ω_{pow} given by (5.19) and (5.22), respectively.

$$\omega'_{base} = \frac{V_{A,\max}}{L_S\sqrt{\left(1-\sigma^2\right)I^2_{Sd,rated}+\sigma^2 I^2_{\max}}} \tag{5.30}$$

$$\omega'_{pow} = \frac{V_{A,\max}}{\sqrt{\frac{2}{1+\sigma^2}}\sigma L_S I_{\max}} . \tag{5.31}$$

Comparing (5.22) and (5.31) one concludes that the constant power range is roughly extended by a factor of $\sqrt{2}V_{B,\max}/V_{A,\max}$ in the dual inverter system, while from (5.19) and (5.30) it is possible to conclude that the base speed increases of a factor approximately equal to $\frac{I_{\max}}{\sqrt{I^2_{\max}-I^2_{Sd,rated}}}$.

5.2 CONTROL SCHEME 1 – BASE SCHEME

The control scheme of the open-ended induction machine fed by the dual-inverter system is shown in Fig. 5.2.

It is basically a rotor-field oriented vector control, whose performance is analyzed extensively in [44] and compared to other robust control schemes for field weakening operation in [45].

The control scheme requires estimating the phase angle θ and the components of the stator and rotor fluxes, but the type of state estimator is not essential for the understanding of the drive operation.

A. *Control of the Induction Machine*

The current references $i_{Sd,ref}$ and $i_{Sq,ref}$ are tracked by the PI controllers (a) and (b).

The speed is adjusted by PI controller (c), which generates the request for the torque-producing current $i_{Sq,req}$. The current reference $i_{Sq,ref}$ may be different from $i_{Sq,req}$, depending on effect of saturation block (d).

The signal $i_{Sq,max}$, which is used to generate the upper and the lower bounds of limitation block (d), is equal to $\sqrt{I^2_{\max}-i^2_{Sd}}$ in region I and II, and to tan(α)$I_{sd,ref}$ in region III.

To adjust the rotor flux, two nested control loops are used. The use of PI regulators operating in closed control loops reduces the need of an accurate knowledge of the machine parameters. The reference value of rotor flux is set by PI regulator (e) on the basis of voltage request of inverters A and B. If v_A is greater than $V_{A,max}$ or v_B is greater than $V_{B,max}$, the rotor flux is reduced. Conversely, if the voltage request is satisfied, the rotor flux is increased. Saturation block (f) ensures that the rotor flux cannot become lower than $\varphi_{R,min}$ or exceed the upper bound $\varphi_{R,max}$.

The value of $\varphi_{R,max}$ is calculated as the minimum between the rated rotor flux, $MI_{Sd,rated}$, and the function $\dfrac{V_{B,max}}{\omega}\dfrac{M}{L_S}$.

$$\varphi_{R,\max} = M \min\left\{ I_{Sd,rated}, \frac{V_{B,max}}{\omega L_S} \right\}. \tag{5.32}$$

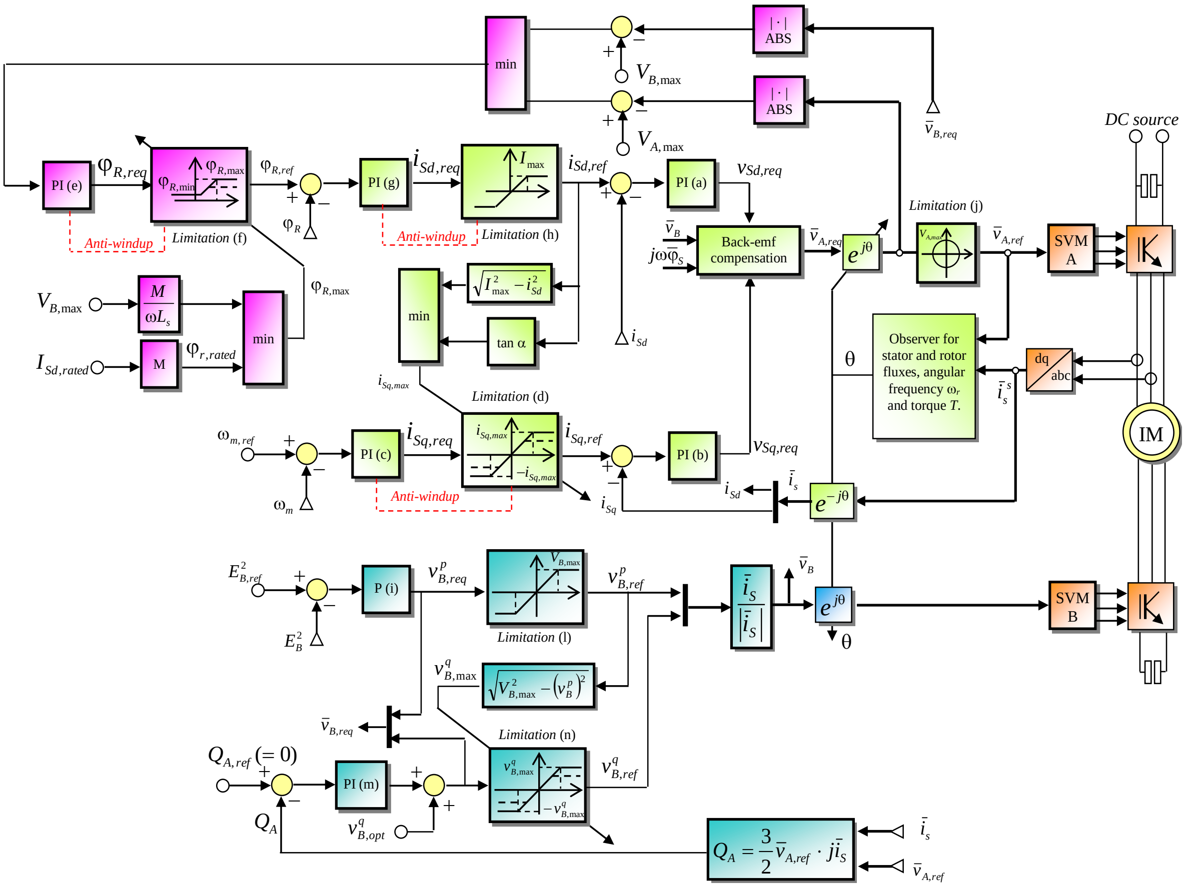

Fig. 5.2 . Block diagram of the RFO control scheme for the open-ended induction machine fed by the dual-inverter system.

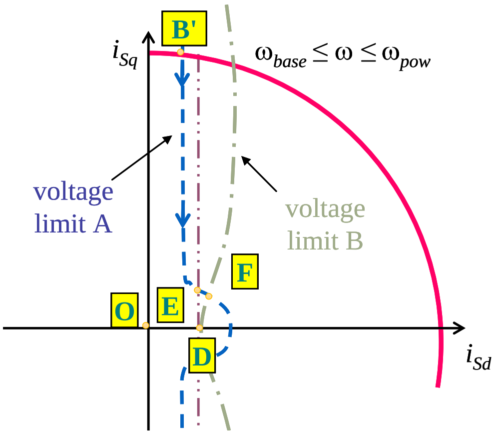

Fig. 5.3. Representation of the motor states when the torque is driven to zero, from point B' to point D, in region II.

The point of coordinates $\left(\frac{V_{B,max}}{\omega L_S}, 0\right)$ is point D in Fig. 5.1. Equation (5.32) is necessary to stabilize the dynamic performance of the drive when it operates at low torque values in the field weakening region or in case of regenerative braking. To illustrate this problem, Fig. 5.3 shows the behavior of the motor when the motor torque is driven to zero in region II. The operating point at the beginning of the transient is B', which corresponds to the maximum achievable torque at the current speed. As soon as the torque decreases, the voltage margin varies and PI(e) tries to increase the rotor flux. If φ_R is limited by (5.32), the stator current moves along the curve B'-E-D, which leads to a smooth transient of current i_{Sd}. Otherwise, if φ_R were unconstrained, the stator current would move along the curve B'-E-F-D, and the crossing of the sharp corner $E\hat{F}D$ would produce an undesired overshoot of i_{Sd}, which has to be avoided for the proper operation of the drive.

If the motor operates in region III or the current i_{Sq} is sufficiently very low, (28) is less strict than (29). In these operating conditions, the field weakening algorithm tries to keep v_B equal to $V_{B,max}$, i.e., the motor state moves on the segment C-O of Fig. 5.1.

To complete the description of the control scheme, it is worth noting that the voltage request $\overline{v}_{A,req}$ is obtained by adding to the output signals of the current regulators the stator back-electromotive force and the voltage at the input of the floating-capacitor bridge, i.e., $j\omega\overline{\varphi}_S + \overline{v}_B$ (feed-forward compensation).

B. *Control of the Floating Capacitor Bridge*

The control of the dc-link voltage E_B is done by proportional controller (i), which compares the actual voltage (squared) with the reference voltage $E_{B,ref}$ (squared). The voltage requested by the controller is

$$v_{B,req}^{p} = K_P^{(g)} \left(E_{B,ref}^2 - E_B^2 \right). \tag{5.33}$$

where $K_P^{(g)}$ is the proportional gain.

If this voltage is in the range [-$v_{B,max}$, $v_{B,max}$] defined by limitation block (l), which is necessary to avoid the over-modulation of inverter B, substituting (5.33) in (4.9), one finds that the capacitor voltage squared is driven by a first-order differential equation,

$$\frac{C_B}{2K_P^{(g)}} \frac{d}{dt} E_B^2 + E_B^2 = E_{B,ref}^2 . \tag{5.34}$$

whose time constant is $\frac{C_B}{2K_P^{(g)}}$.

The set-point for voltage $v_{B,req}^{q}$ should be equal to $v_{B,opt}^{q}$ given by (5.16), however the use of PI (m) ensures that inverter A operates at unity power factor also in presence of parameter or model uncertainties.

Finally, voltage vector $\bar{v}_B$ is generated according to (4.8).

C. *Remarks on the Control Scheme*

The field-weakening algorithm is not simply based on the reduction of the flux inversely to the speed, but it relies on the adaptive control of the flux level depending on the comparison of the requested voltage with the available voltage. In this way, the choice of the flux level is nearly optimal and does not depend on parameters, such as the resistance, which may vary during the motor operation. The control scheme can operate in the constant power speed range, and in the decreasing power speed range (region III) as well, a feature that is not available in other control schemes. As regards the power factor of inverter A, the control loop can compensate slight deviations of the control parameters from their nominal values, provided that this mismatching does not completely prevent the motor operation. In fact, the estimation of the reactive power of inverter A does not depend on the motor parameters, since it is measured as $\frac{3}{2}\bar{v}_{A,ref} \cdot j\bar{i}_S$. The misalignment of the reference frame does not affect the calculation of the dot product, only the nonlinearities of the inverter and the sensors have some influence.

D. *Experimental Results*

Some experimental tests have been carried out with a laboratory prototype to verify the feasibility of the proposed control scheme. The picture of the dual inverter prototype is shown in Fig. 5.4, while the parameters of the experimental setup are reported in TABLE 5

Fig. 5.5 shows the acceleration transient of the open-end winding induction motor when the final speed belongs to region II. As can be seen in Fig. 5.5(a), initially the stator current is different from zero and the motor is magnetized (point A in Fig. 5.1). The current i_{Sq} abruptly increases up to the maximum admissible value (point B) when the speed step is applied. As soon as the available voltage is not sufficient to inject the current, the signal at the input of PI (e) becomes negative and the rotor flux decreases, while the current i_{Sq} slightly increases to fully exploit the current limit of inverter A (points of arc B-C). Finally, when the acceleration torque is not needed any more, at the end of the transient, the current i_{Sq} decreases to the steady-state value.

Fig. 5.5(b) shows the behavior of the drive in the same operating conditions of Fig. 5.5(a).

TABLE 5 – IM-OEW PARAMETERS

P_{rated}	=	0.69	kW	R_S	=	1.0	Ω
$I_{S,rated}$	=	10	A_{peak}	R_R	=	1.2	Ω
$I_{Sd,rated}$	=	5.8	A_{peak}	L_S	=	0.112	H
$\omega_{m,rated}$	=	600	rpm	L_R	=	0.112	H
σ	=	0.127		M	=	0.102	H
J_m	=	0.03	Kg m^2	p	=	2	
E_A	=	150	V	E_B	=	300	V

However, the maximum rotor flux $\varphi_{R,max}$ is calculated as $MI_{Sd,rated}$ and not by means of (5.32).

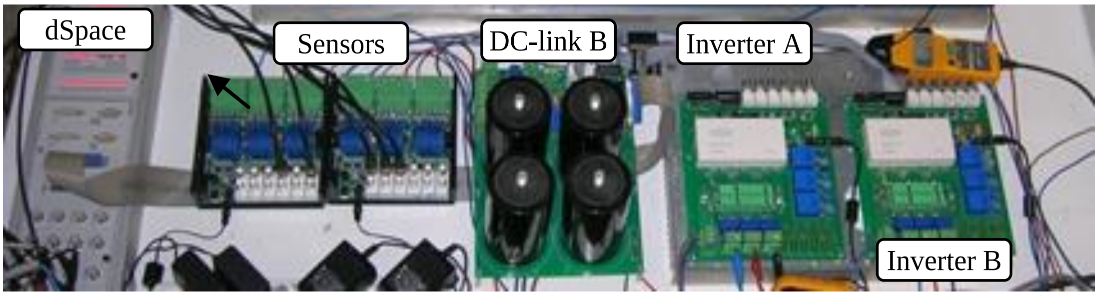

Fig. 5.4. Laboratory prototype of the dual inverter system that feeds an open-ended induction machine.

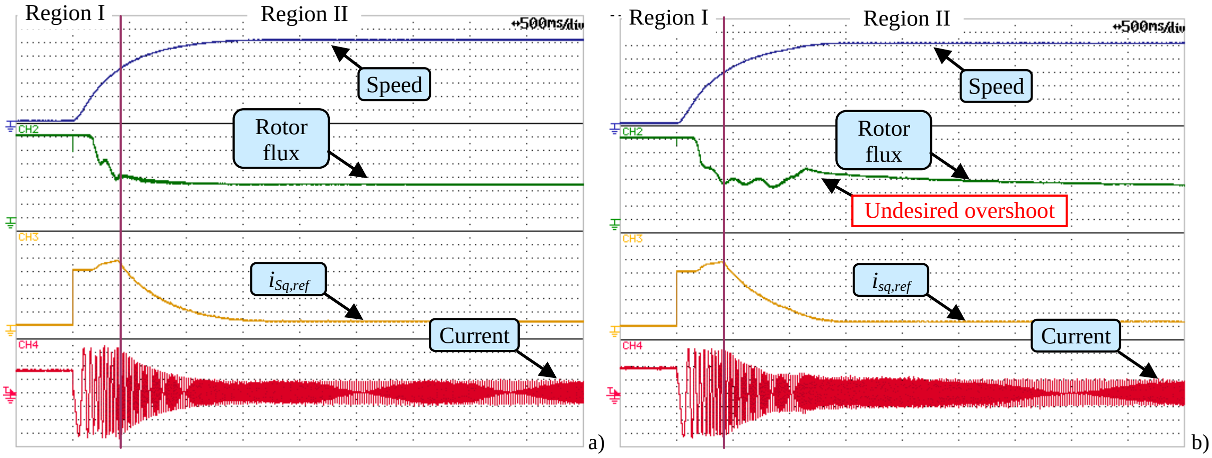

Fig. 5.5. Experimental results. Behavior of the open-ended induction motor during a speed transient from 0 to 1500 rpm, when (40) is used (a), or $\varphi_{R,max}$ is $MI_{Sd,rated}$ (b). Motor speed (250 rpm/div). Rotor flux (0.1 Wb/div). Current i_{Sq} (2 A/div). Line current (3 A/div).

As can be seen, the transient of the magnetizing current reveals an unexpected overshoot, which is avoidable if (5.32) is used, due to the crossing of the sharp corner $E\hat{F}D$ of Fig. 5.3.

Fig. 5.6 shows the behavior of the open-ended induction machine during an acceleration transient up to ten times the base speed (the end of the transient is not visible).

In Fig. 5.6a), region II and region III are clearly identified. In region II the amplitude of the motor current is constant, while it tends to decrease in region III.

In Fig. 5.6(b) it is possible to verify that the power factor of inverter A is unity in all operating conditions, despite the unavoidable changes that occur in the parameters during the

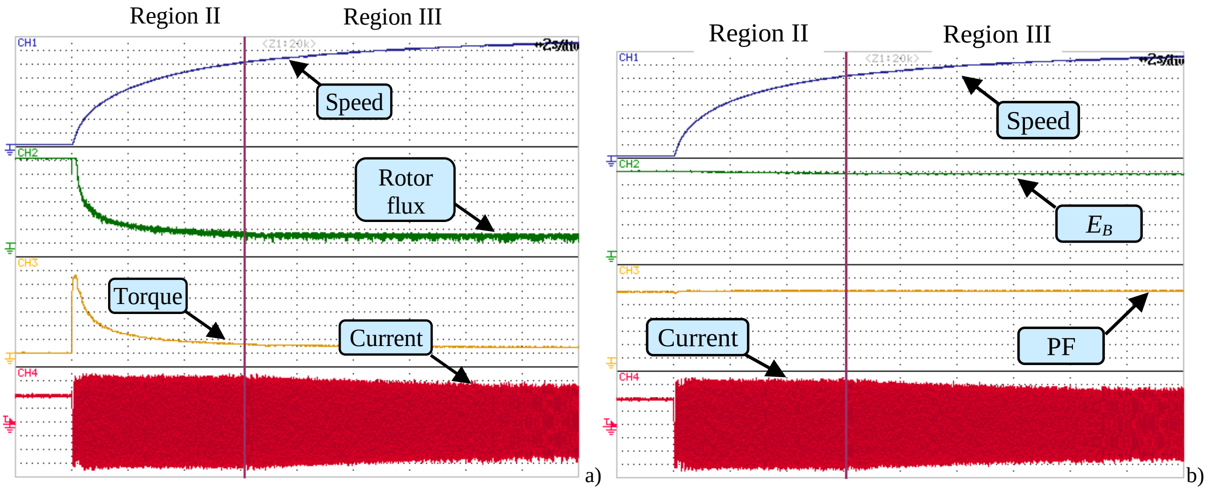

Fig. 5.6. Experimental results. Behavior of the open-ended induction motor during a speed transient from 0 to 5000 rpm. a) Motor speed (550 rpm/div). Rotor flux (0.1 Wb/div). Motor torque (2 Nm/div). Line current (3 A/div); b) Motor speed (550 rpm/div). DC-link voltage E_B (50 V/div). Power factor of inverter A (0.2 pu/div). Line current (3 A/div).

flux weakening, such as an increase in the inductances due to the reduction of the magnetic saturation, and the variation of the rotor resistance due to the high rotor frequency. Similarly, voltage E_B is correctly kept constant by the control system.

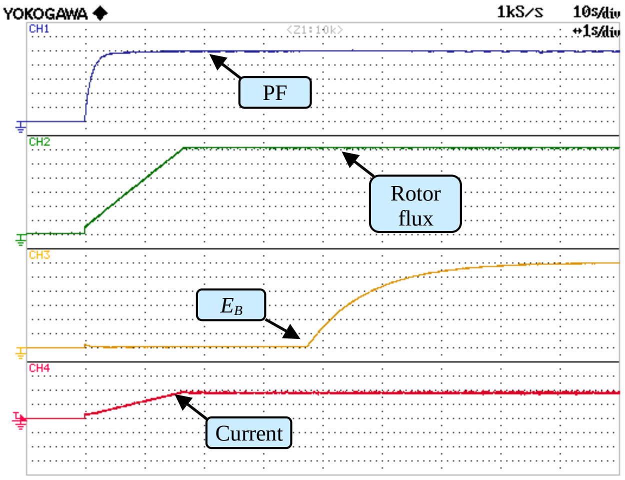

Fig. 5.7. Magnetization transient of the open-ended induction motor. Power factor (0.2 pu/div). Rotor flux (0.1 Wb/div). DC-link voltage E_B (50 V/div). Stator current (3 A/div).

Fig. 5.7 shows the magnetization transient at stand-still, during which the DC-link of inverter B is charged and the rotor flux reaches the rated value. As can be seen, firstly the motor is magnetized and the flux increases up to the rated value. Then, there is the progressive charge of the DC-link of inverter B.

Finally, Fig. 5.8 compares the torque and power capability of the dual inverter drive and the single inverter drive, measured at steady state, as a function of the normalized speed. The normalization weight is the base speed, i.e. the starting point of the field weakening speed range. As can be seen, the mechanical power of the dual inverter drive, is approximately constant, despite a progressive reduction that is presumably due to the increasing iron losses, which are not considered in the mathematical analysis. Overall, the mechanical power of the single inverter drive at high speed is significantly lower and during the test it was not possible to reach the same maximum speeds for both drives.

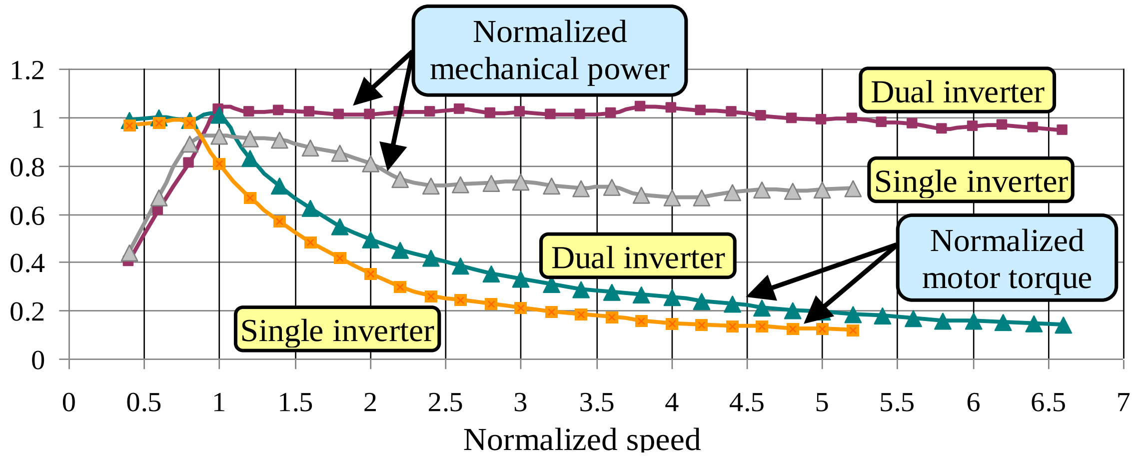

Fig. 5.8. Normalized values of the motor torque and mechanical power as a function of the normalized speed. The normalized weights are respectively the torque and the power at the base speed, 13 Nm and 0.69 kW, respectively. The base speed is 600 rpm

5.3 CONTROL SCHEME 2 – VARIABLE DC-LINK VOLTAGE

Since the losses of the secondary inverter are a drawback of the dual inverter topology, a control scheme with variable voltage of the DC link of the floating bridge has been investigated. Equation (4.27) shows that, in steady-state condition, inverter B has to generate a voltage that is substantially proportional to ω. Consequently, when ω is not high, there is no need to keep the DC-link voltage of inverter B at the rated value. Since the switching losses of inverter B are proportional to the voltage level, the reduction of E_B can be beneficial for the overall efficiency of the electric drive.

Fig. 5.9 shows the control scheme developed and highlights the changes introduced to the base scheme of Fig. 5.2. In addition to the control of the floating bridge voltage, the upper limit of the flux level is now just the magnetizing current $I_{Sd,rated}$ multiplied by the mutual inductance M.

In the control scheme of Fig. 5.2, due to the particular shape of the voltage constraint

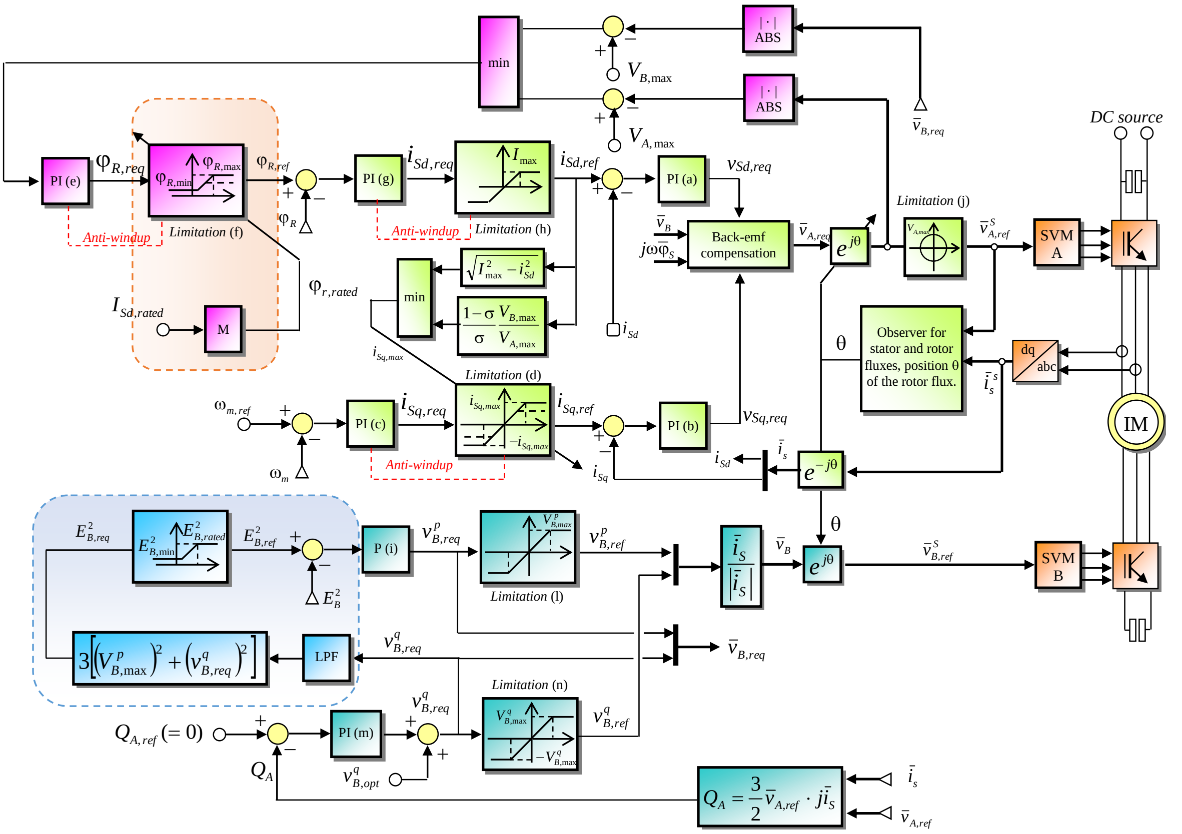

Fig. 5.9. Block diagram of the RFO control scheme for the open-ended induction machine fed by the dual-inverter system with variable voltage of the floating capacitor

curves, another upper value was imposed in order to avoid the sharp corner $E\hat{F}D$ illustrated in Fig. 5.3, which can be easily avoided in this new control scheme by simply adjusting the DC-link voltage reference.

A. *Control of the Floating Inverter*

With reference to Fig. 5.9, PI regulator (m) ensures that inverter A operates at unity power factor. The output of this regulator is the component $v^q_{B,ref}$ of $\bar{v}_B$ along the direction orthogonal to the stator current. To improve the dynamic performance, the value $v^q_{B,opt}$ given by (4.27), is added to the output of regulator (m). The saturation block (n) limits $v^q_{B,ref}$ so it remains in the range $[-V^q_{B,max}, V^q_{B,max}]$, where

$$V^q_{B,max} = \sqrt{\left(V_{B,max}\right)^2 - \left(V^p_{B,max}\right)^2} \,. \tag{5.35}$$

In (5.35) $V^p_{B,max}$ is a voltage margin that is necessary to ensure a satisfactory behavior in transient operation.

The DC-link voltage E_B is controlled by the proportional regulator (i), which compares the actual voltage (squared) with the reference voltage $E_{B,ref}$ (squared). The output of regulator (i) is $v^d_{B,ref}$, which is zero in steady-state operating conditions but can be used in transient operating condition to vary the DC-link voltage of inverter B.

However, the value of $E_{B,ref}$ can significantly change not only with the speed but also with the torque, and may be less intuitive than expected. Fig. 5.10 shows the boundaries of the

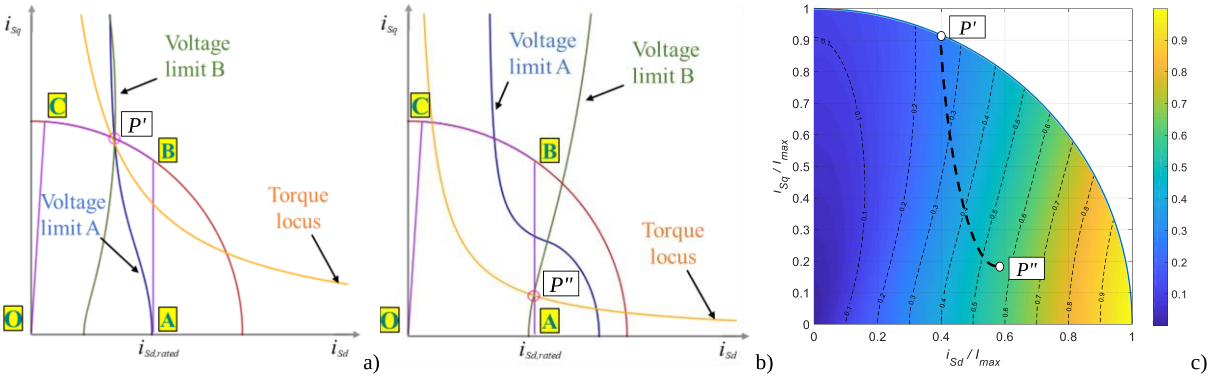

a) b) c)

Fig. 5.10. Representation of the motor operating conditions in the plane i_{Sd}-i_{Sq} for a dual inverter drive at ω=1.3ω_{base}. (a) The voltage constrains of inverter A and B are plotted at T=0.75 T_{base}. (b) The voltage constrains of inverter A and B are plotted at T=0.25 T_{base}. (c) Normalized contour plot of $v^q_{B,opt}$.

stator current vector resulting from voltage constraints (4.13) and (4.14) at an angular frequency of 1.3 ω_{base} for two different values of the electromagnetic torque. The different values of torque lead to different DC-link voltages of inverter B. In Fig. 5.10(a) the electromagnetic torque is 75% of the rated torque. The control system drives the motor to operate in point P', which is the intersection of the curves resulting from the operating constraints on the stator current and the voltage of inverter A. The DC-link voltage of inverter B is adjusted by the control system so that the power factor of inverter A is unity. In essence, E_B decreases until the corresponding constraint curve passes through point P' (20% of the rated voltage). In Fig. 5.10(b) the torque drops to 25% of the rated one. The control system increases the magnetizing current up to the rated value, and the operating point becomes P''. To preserve the unity power factor, the voltage of inverter B has to increase up to 50% of the rated value. This behavior is confirmed by Fig. 5.10(c), which depicts the contour plot of $v^q_{B,opt}$, expressed by (16) and normalized by $|\omega| L_S I_{max}$. To plot this figure, σ is assumed equal to 0.11. As can be seen, the trajectory of the machine state from P' to P'', namely from a high torque level to a low torque level, leads to higher values of $v^q_{B,opt}$ and to an increase in the DC-link voltage of inverter B.

B. *Experimental Results*

The same lab setup shown in Fig. 5.4 and defined by the parameters of TABLE 5 has been used to carry out the following tests.

Fig.5.11 illustrates the magnetization transient of the machine. Initially, the speed is zero. Then, the current i_{Sd} progressively increases while the machine is magnetized. Simultaneously, the DC link voltage of inverter B increases up to the value $V^p_{B,max}/\sqrt{3}$.

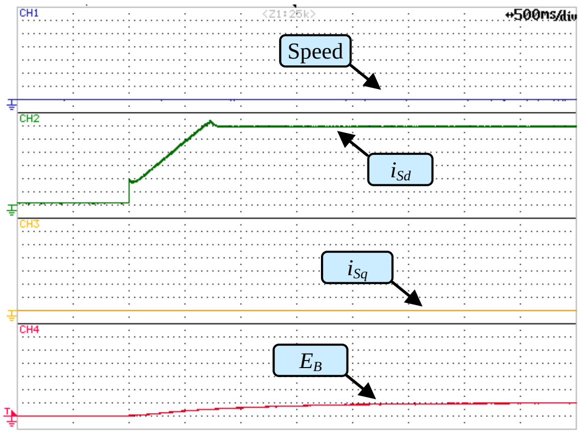

Fig.5.11. Experimental behavior of the open-ended induction motor during a magnetization transient. Speed (2000 rpm/div), i_{Sd} (2A/div), i_{Sq} (2A/div), DC-link voltage of inverter B (50 V/div).

Fig. 5.12 illustrates the behavior of the induction machine during a start-up transient from zero to five time the base speed. The motor current, whose initial frequency is very low, rapidly changes after the speed step

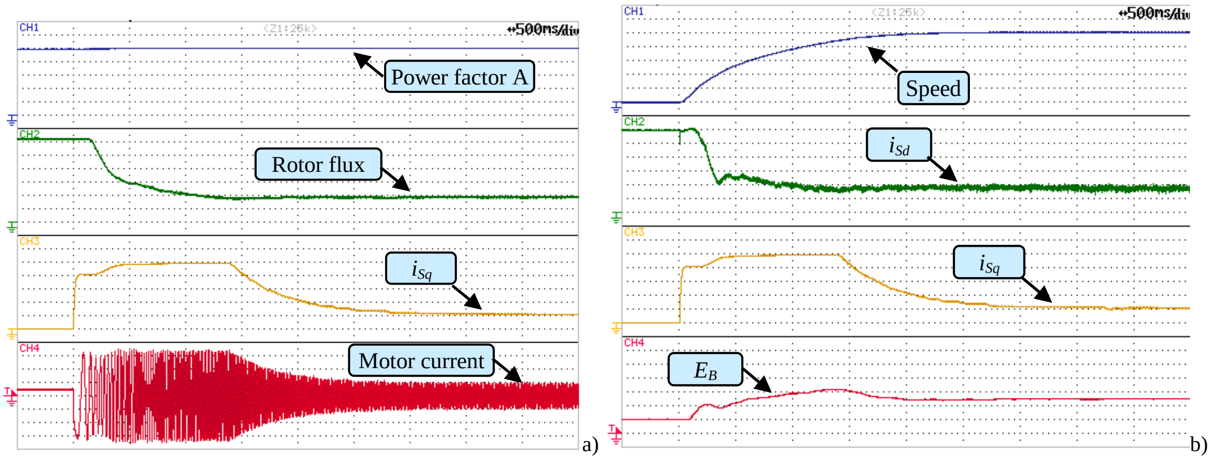

Fig. 5.12 Experimental behavior of the open-ended induction motor during a speed transient from zero to five time the base speed. a): power factor (0.2/div), rotor flux (0.1 Wb), i_{Sq} (2A/div), motor current (4 A/div). b): speed (500 rpm/div), i_{Sd} (2A/div), i_{Sq} (2A/div), DC-link voltage of inverter B (50 V/div).

command. The motor torque, proportional to i_{Sq}, rises to the maximum value, limited only by the inverter rated current. Then, i_{Sq} decreases due to the flux weakening operation.

Fig. 5.12 (a) shows that the power factor of inverter A is equal to 1 at any speed, while the rotor flux smoothly decreases with speed.

Fig. 5.12 (b) confirms that the DC-link voltage of inverter B changes depending on the motor operation. The value of E_B depends not only on the stator angular frequency ω but also on the components of the stator current. Consequently, as can be seen in Fig. 5.12 (b), the control system increases $E_{B,ref}$ when the machine has to deliver high torque values to the load.

Fig. 5.13 shows the contour maps of the floating bridge voltage and the ratio of the efficiency η_{opt} of the proposed drive to the efficiency of a similar drive that does not optimize the DC-link voltage of inverter B. In Fig. 5.13(a) it can be seen as the floating bridge voltage is higher for lower value of the torque, as explained in the example of Fig. 5.10(b). Fig. 5.13(b) shows that the efficiency improvement of the adaptive control of E_B is particularly significant around the rated torque and reaches 45% for the small-scale prototype. This notable result is unlikely to be obtained in industrial drives and is due to the low efficiency of the small-scale prototype, about 0.6, in the rated operating conditions. In flux weakening condition, although Fig. 5.13(a) shows a region when the voltage of inverter B is below the rated one, the efficiency improvement does not seem significant.

The efficiency of the drive is measured directly as a ratio of the output mechanical power to the input electrical power. Although the measurements can be inaccurate at low power levels, the results seem stable and repeatable in the rated operating conditions.

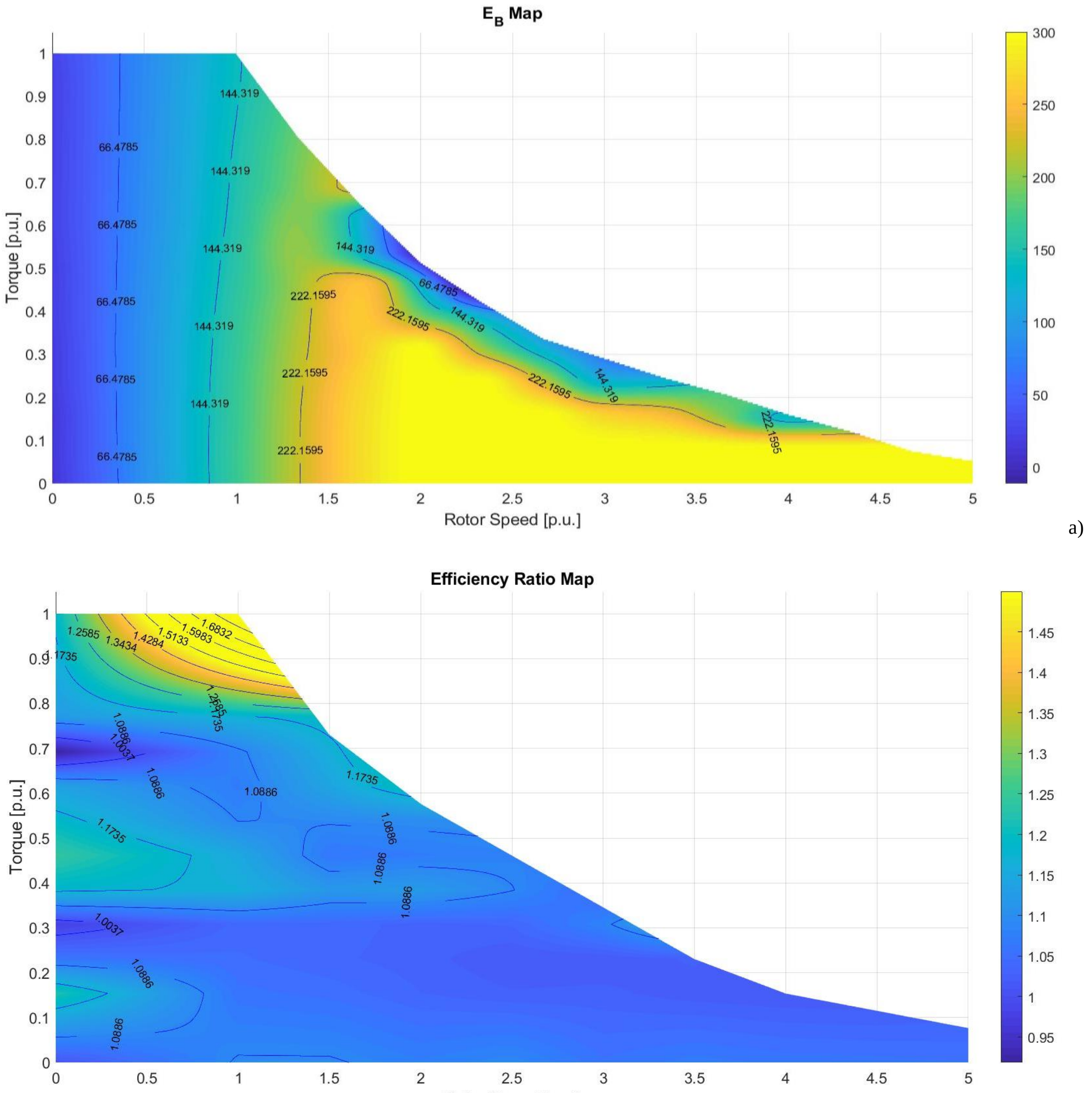

Fig. 5.13. Experimental results. a) Value of floating inverter voltage; b) ratio of the efficiency of the proposed drive to the efficiency of the same drive without optimizing the voltage of inverter B. Torque values are expressed in pu of the maximum torque, speed values are expressed in p.u. of the base speed.

5.4 CONTROL SCHEME 3 – OVERMODULATION OF THE PRIMARY INVERTER

The control scheme of the dual inverter drive can be further improved by adding to the primary inverter the capability of operating in voltage overmodulation conditions. The output power increases by about 15% and, contextually, the waveform of the stator current does not worsen as long as the secondary inverter, acting as a series active filter, can compensate the voltage distortion. The base control scheme of Fig. 5.2 modifies as shown in Fig. 5.14.

The maximum voltage that inverter A can produce in the linear modulation range is $\frac{E_A}{\sqrt{3}}$. This value corresponds to the radius of the circle inscribed in the hexagon shown in Fig. 5.15, which represents the domain of all admissible voltage vectors $\bar{v}_A$, expressed in terms of

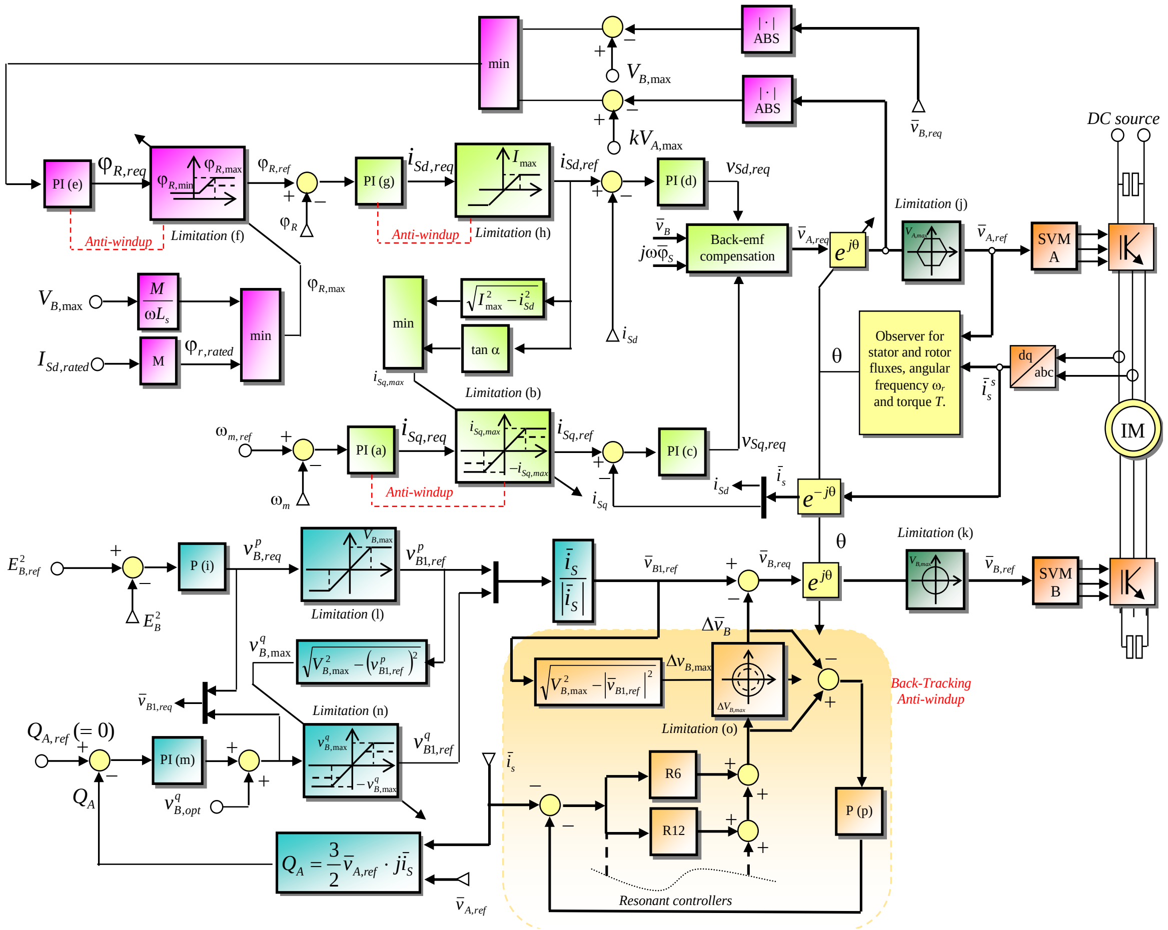

Fig. 5.14 . Block diagram of the RFO control scheme for the open-ended induction machine fed by the dual-inverter system, with the primary inverter operating in voltage overmodulation.

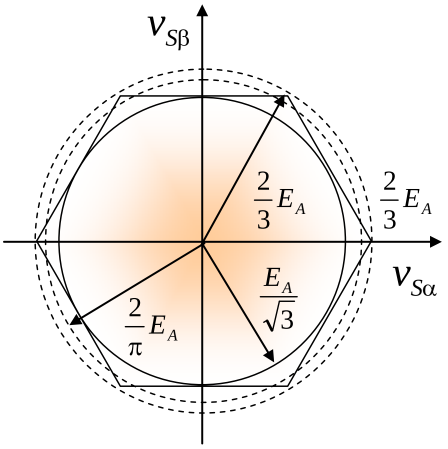

Fig. 5.15. Admissible voltage vectors of inverter A represented in the complex plane.

components $v_{S\alpha}$ and $v_{S\beta}$ in the stationary reference frame. The same figure shows that the magnitude of $\overline{v}_A$ could be greater than $\frac{E_A}{\sqrt{3}}$. When the phase angle of $\overline{v}_A$ is a multiple of 60°, the magnitude of $\overline{v}_A$ (average value over a switching period) can rise to $\frac{2}{3}E_A$. However, except for these angles, the magnitude of $\overline{v}_{A,req}$ must be scaled so that $\overline{v}_{A,ref}$ fits in the hexagonal shape. In this case, the magnitude of the fundamental component of $\overline{v}_A$ increases to $V_{A,\max}$, i.e., $\frac{2}{\pi}E_A$.

When the magnitude of the desired voltage, $\overline{v}_{A,req}$, is greater than $\frac{E_A}{\sqrt{3}}$, inverter A is said to operate in the overmodulation mode. When this happens, during each fundamental period, the resulting voltage vector $\overline{v}_A$ partially or totally moves on the sides of the hexagon. Consequently, the voltage is distorted by the irregular path of $\overline{v}_A$, which does not follow the same circular trajectory of $\overline{v}_{A,req}$.

The stator voltage can be written as follows:

$$\overline{v}_S = \overline{v}_A - \overline{v}_B = \left(\overline{v}_{A,req} - \Delta\overline{v}_A\right) - \overline{v}_B \tag{5.36}$$

where $\Delta\overline{v}_A$ is the resulting voltage disturbance, which reduces the requested voltage $\overline{v}_{A,req}$.

However, (5.36) shows that the voltage applied to the machine can still be undistorted if

$\bar{v}_B$ can compensate the term $\Delta\bar{v}_A$, provided that this new task does not interfere with the fundamental operation of inverter B, whose voltage can be rewritten as follows:

$$\bar{v}_B = \bar{v}_{B1} - \Delta\bar{v}_B . \tag{5.37}$$

where $\bar{v}_{B1}$ is the fundamental component, and $\Delta\bar{v}_B$ is the compensating term of $\Delta\bar{v}_A$.

The fundamental component $\bar{v}_{B1}$ is not disturbed if $\bar{v}_A$ has a magnitude lower than $\frac{2}{3}E_A$ because $\Delta\bar{v}_A$ does not contain a component at the fundamental angular frequency ω, but contains only components at frequencies multiples of 6*n*ω in the rotor reference frame.

A bank of *N* resonant controllers can be used to cancel the voltage harmonics that are generated when inverter A operates in the overmodulation range and the voltage vector $\bar{v}_A$ moves on the hexagonal boundary. The transfer function of the bank of resonant controllers is as follows:

$$R_{res} = \sum_{n=1}^{N} R_{6n} = \sum_{n=1}^{N} \frac{2K_n s}{s^2 + (6n\omega)^2} . \tag{5.38}$$

The resonant frequencies in (5.38) depend on the angular frequency of the rotor flux vector and are multiple of 6ω. Such a transfer function, in the stator reference frame, cancels the harmonic components of the phase currents at frequencies $(6n\pm1)\omega$, with $n = 1, 2, \dots, N$.

A. *Experimental Results*

Fig. 5.16 shows the behavior of the motor during a start-up transient. At the beginning, the motor current is equal to the magnetizing current. Then, the motor current increases quickly to satisfy the torque request. In the constant power speed range the amplitude of the stator current is nearly constant, afterwards it starts decreasing. The power factor and the DC-link voltage of inverter B remains constant over the entire speed range.

Fig. 5.17 depicts the waveforms of the voltages and currents of the dual inverter drive operating in the high speed region. Fig. 5.17(a) shows that the waveforms of $v_{A\alpha}$ and $v_{A\beta}$ are distorted when $\bar{v}_A$ moves on the border of the voltage hexagon, and Fig. 5.17(b) shows that the duty-cycle m_{A1} of the first leg of inverter A is nearly trapezoidal. As can be seen, voltage $\bar{v}_B$ develops a compensating component that balances the distorting harmonics of $\bar{v}_A$ and

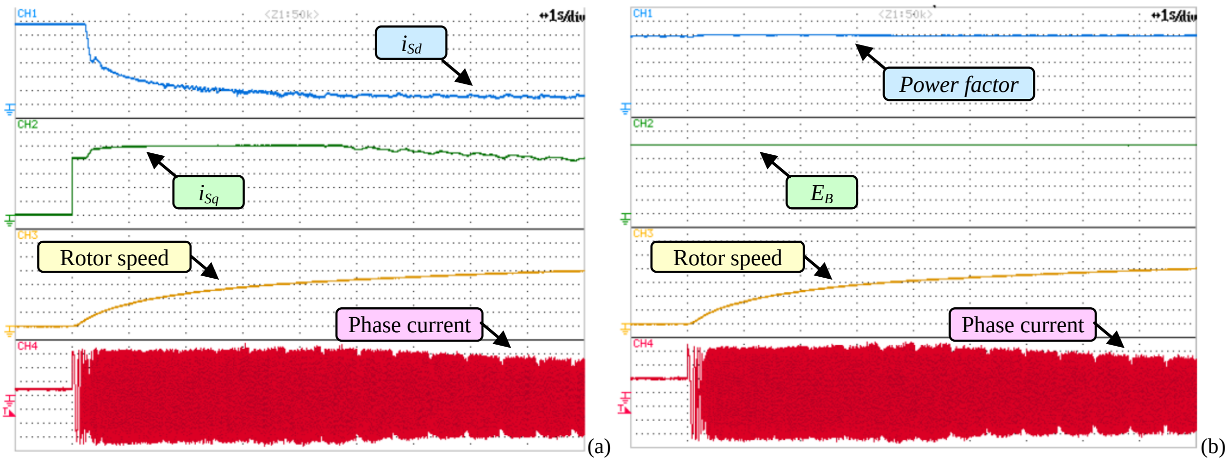

Fig. 5.16. Behavior of the open-ended induction motor during a speed transient from zero to five time the base speed. Current i_{Sd} (1A/div), i_{Sq} (2A/div), rotor speed (1000 rpm/div), phase current (3 A/div), power factor (0.2/div), rotor flux (0.1 Wb), voltage E_B (60 V/div).

ensures a sinusoidal stator voltage. This is indirectly demonstrated by the undisturbed waveform of the stator current shown in Fig. 5.17(b).

To appreciate the improvements in the performance due to the overmodulation algorithm, Fig. 5.18 shows the trends of the speeds for three different cases, namely the single-inverter system, the dual inverter system operating in the linear voltage range and the dual inverter system operating in overmodulation mode.

As a result, the dual inverter system provides a higher accelerating power in comparison to the single inverter system, so, after the same amount of time from the beginning of the transient, the speed of the former drive is notably greater than that of the latter. The overmodulation algorithm increases further the motor power approximately by a factor $\frac{2}{\pi}\sqrt{3}$

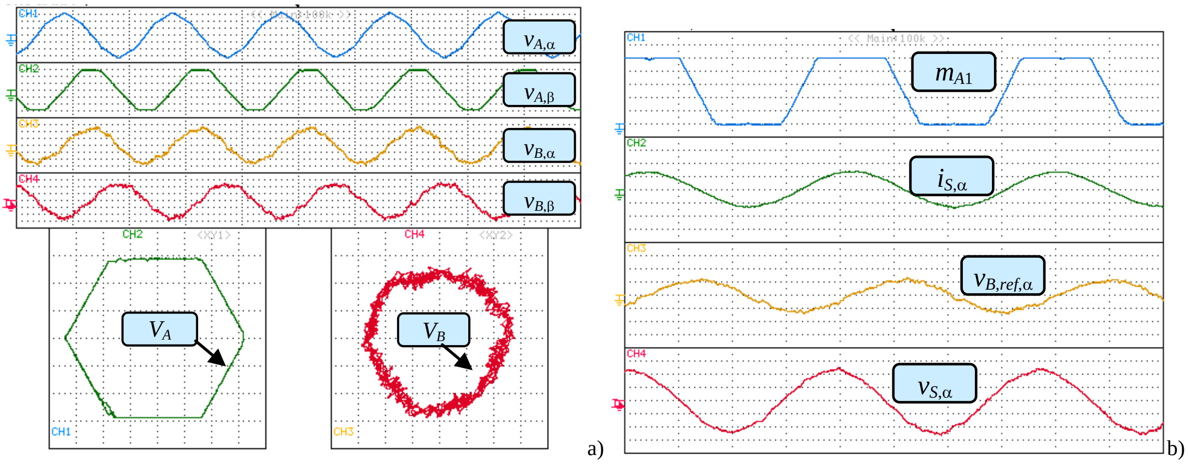

Fig. 5.17 Comparison of the speed trends during an acceleration transient for the dual inverter with and without overmodulation of the primary inverter, and a single inverter system feeding the same induction motor.

(≅ 1.10), and, consequently, the corresponding curve of the motor speed is above the other curves.

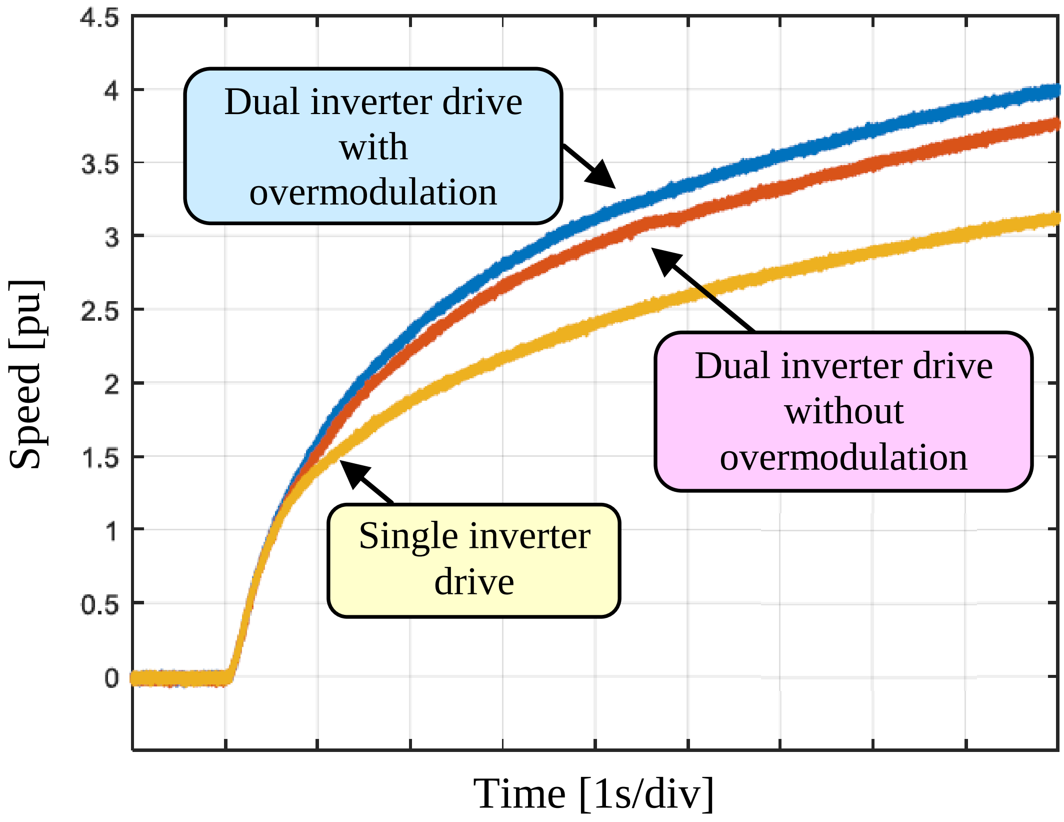

Fig. 5.18. Comparison of the speed trends during an acceleration transient for the dual inverter with and without overmodulation of the primary inverter, and a single inverter system feeding the same induction motor.

Chapter 6

SURFACE PERMANENT MAGNET SYNCHRONOUS MOTOR WITH OPEN-END WINDINGS

A high torque density makes Surface Permanent Magnet Synchronous Machines (SPMSMs) suitable for industrial applications, if they are not required to operate over a wide speed range. Interior Permanent Magnet Synchronous Machines (IPMSMs), which use ferrite magnets and compensate the resulting reduction in the flux level with the reluctance torque due to the rotor saliency, are preferred in spindle-drive applications.

Nevertheless, the use of a solid rotor core in SPMSMs has several advantages, such as simplifying the manufacturing process, better robustness and efficiency, and lower costs, so several solutions to widen the motor speed range have been developed and can be found in the literature. The simplest one is the use of a step-up converter to boost the DC-link of the main inverter. However, this topology requires adding some bulk inductors at the input of the converter and the boost ratio is generally not greater than two [46]. Other solutions include the use of two inverters to feed a motor with open-end windings [47]. Two separated DC-links can supply both sides of the stator windings and double the phase voltage. If two separated power sources are not available, the inverters can share the same DC-link [48]. However, this solution causes the problem of the common mode current that can circulate in the drive.

The control scheme of the configuration where the second inverter is a floating capacitor bridge has been analyzed in [49]. The modulation strategy of the dual inverter has been investigated in [50], where two different technologies (Si and SiC) have been adopted for the switches of the main inverter and the floating bridge, depending on the respective switching frequencies. Finally, some techniques to estimate the machine parameters have been proposed in [51].

6.1 SYSTEM MODEL

A. Mathematical Model and Admissible Domain of the Stator Current

The mathematical model of a SPM motor in a d-q reference frame with the d-axis aligned with the excitation field can be written as follows:

$$v_{Sd} = R_S i_{Sd} - \omega \varphi_{Sq} + \frac{d\varphi_{Sd}}{dt} \tag{6.1}$$

$$v_{Sq} = R_S i_{Sq} + \omega \varphi_{Sd} + \frac{d\varphi_{Sq}}{dt} \tag{6.2}$$

$$\varphi_{Sd} = L_S i_{Sd} + \varphi_e \tag{6.3}$$

$$\varphi_{Sq} = L_S i_{Sq} \tag{6.4}$$

$$T = \frac{3}{2} p \varphi_e i_{Sq} \tag{6.5}$$

where ω is the angular frequency of the rotor speed in electric radians, p is the number of pole pairs, T is the electromagnetic torque, v_{Sd} and v_{Sq} are the d-q components of the stator voltage vector $\bar{v}_S$, i_{Sd} and i_{Sq} are the d-q components of the stator current vector $\bar{i}_S$, φ_{Sd} and φ_{Sq} are the d-q components of the stator flux vector $\bar{\varphi}_S$, φ_e is the excitation flux, L_S and R_S are the stator inductance and resistance respectively.

This mathematical model is equal to the one expressed by (4.2)-(4.6) if $L_{Sd} = L_{Sq}$. Therefore, the saliency factor of a surface PM motor, δ, is equal to 1.

The voltage constraints of inverter A and inverter B in steady-state condition, given from (4.33) and (4.34) respectively, can be written for a PM motor with open-end stator windings as follow:

$$|\omega| \left(L_S \left|\bar{i}_S\right| + \varphi_e \frac{i_{Sd}}{\left|\bar{i}_S\right|} \right) \le V_{B,\max} . \tag{6.6}$$

$$\frac{\left|\omega i_{Sq}\right|}{\left|\bar{i}_S\right|} \varphi_e \le V_{A,\max} \tag{6.7}$$

Inequality (6.7) is valid as long as (6.6) is verified, otherwise $\bar{v}_B$ becomes the one in (4.29) and inverter A voltage constraint changes as shown in the following expression, obtained by substituting (4.29) in (4.1):

$$\left|\left(L_S+\frac{V_{B,\max}}{|\omega||\bar{i}_S|}\right)\bar{i}_S+\varphi_e\right|\le\frac{V_{A,\max}}{|\omega|}. \qquad (6.8)$$

The admissible domain of the stator current vector, resulting from the constraints of the inverter voltages and the stator current can be plotted in a complex plane, where the horizontal and vertical axes are respectively i_{Sd} and i_{Sq}, as shown in Fig. 6.1.

The admissible current vectors are those delimited by a circle with constant radius I_{max}. The curves coming from the voltage constraints (6.7) and (6.6), which tend to change as ω increases and depend on the values of the system parameters, identify the current vectors that can be injected into the machine at a given speed. It is worth noting that these curves are very different from those of a traditional SPM motor drive and have a non-null intersection, highlighted in blue, even at high speed. At a given speed, the maximum torque is generated when the stator current is the vector with the highest value of i_{Sq} in the admissible domain.

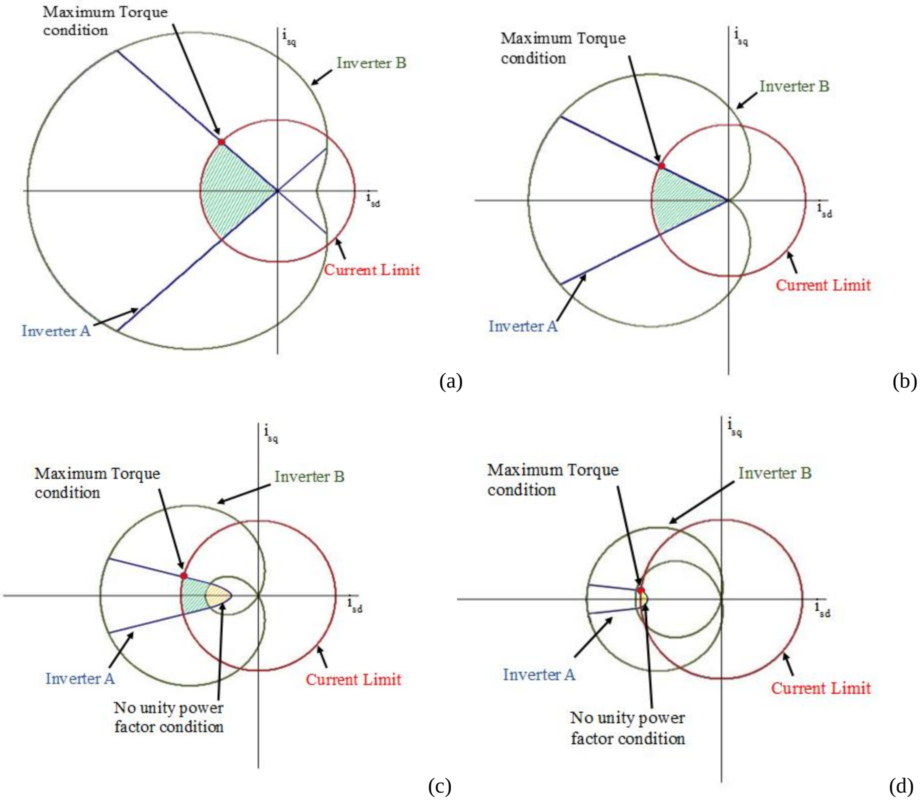

(a) (b)

(c) (d)

Fig. 6.1 . Representation of the voltage and current constraints in plane i_{Sd}-i_{Sq} for a SPM motor in dual inverter configuration. The voltage constrains are plotted at $\omega=1.45\cdot\omega_{base}$ (a); at $\omega=2.2\cdot\omega_{base}$ (b); $\omega=9\cdot\omega_{base}$ (c) and $\omega=11\cdot\omega_{base}$ (d).

When the speed is not excessive, this domain, obtained by intersecting the areas delimited by the three curves, is a circular sector, as shown in Fig. 6.1(a) and (b). However, at higher speeds, Fig. 6.1(c) shows the existence of another region, in which the power factor is not unity, which allows extending the speed range further.

B. *Resulting Speed Range*

The base speed ω_{base} of the dual inverter system can be calculated from (6.7) when i_{Sq} is equal to I_{max} and i_{Sd} is zero.

$$\omega_{base} = \frac{V_{A,\max}}{\varphi_e}. \tag{6.9}$$

The base speed ω'_{base} for the same motor fed by just one inverter can be found from (4.39).

In the dual inverter drive with a SPM motor, the maximum speed where the maximum power is delivered is when i_{Sq} is zero (no-load condition) and i_{Sd} is equal to $-I_{\max}$. (maximum demagnetization field) if the excitation flux φ_e exceeds the flux generated from the maximum current flowing on the stator inductance $L_S I_{max}$. Equation (4.42) provides the following result:

$$\omega_{pow} = \frac{V_{B,\max}}{\varphi_e - L_S I_{\max}}. \tag{6.10}$$

Furthermore, it is possible to increase the maximum speed of the drive above ω_{pow} by abandoning the unity power factor condition. When i_{Sq} is zero and i_{Sd} is equal to $-I_{max}$, the maximum speed turns out to be:

$$\omega_{pow} = \frac{V_{A,\max} + V_{B,\max}}{\varphi_e - L_S I_{\max}}. \tag{6.11}$$

If the DC-link voltage of inverter B is twice that of inverter A, the speed range of the dual inverter system is three times as wide as that of a single inverter drive.

The resulting speed ranges are shown in Fig. 6.2, which has been plotted under the assumptions that the voltage drops on the stator resistances and the iron losses are negligible. The parameters adopted to draw the curves are those of a low-power prototype used to carry out the experimental results. The parameters are listed in TABLE 6.

TABLE 6 – SPM-OEW PARAMETERS

P_{rated}	=	0.9	kW	R_S	=	0.24	Ω
$I_{S,rated}$	=	13	A_{peak}	L_S	=	0.0012	H
φ_e	=	0.0852	Wb	J_m	=	0.03	Kg m^2
$\omega_{m,rated}$	=	1600	rpm	J_C	=	0.19	Kg m^2
$E_{A,max}$	=	80	V	p	=	3	
C	=	160	μF	$E_{B,max}$	=	160V	

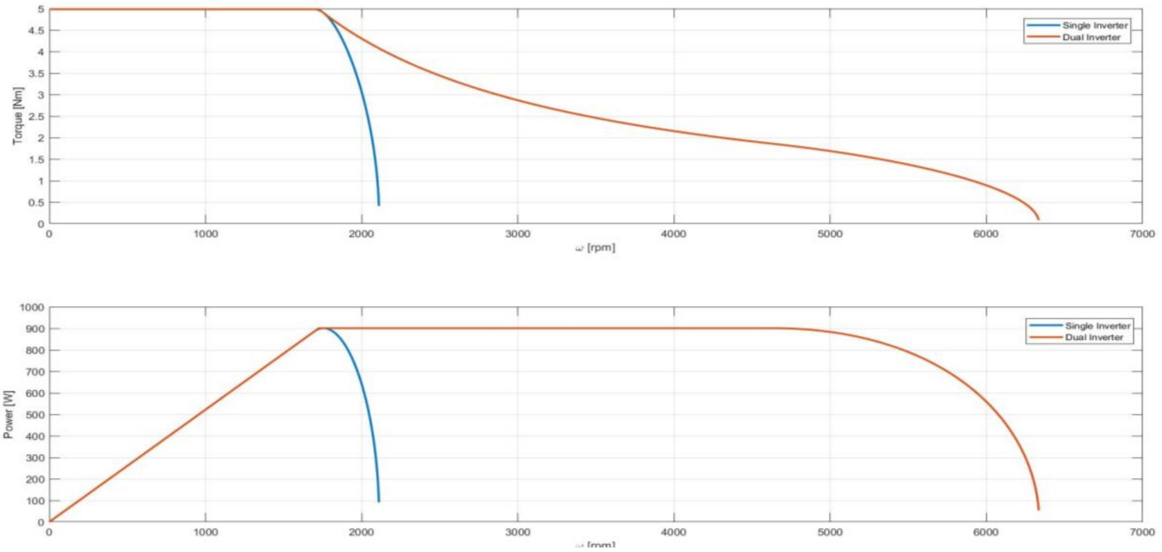

Fig. 6.2. Performance of the drive fed by the dual inverter (red) and by a single inverter (blue) systems.

6.2 CONTROL SCHEME

The control scheme shown in Fig. 6.3 can be divided into two parts. The first part concerns the control of the inverter A, which is connected to the power supply. It includes the control loops for speed, flux and stator currents. The aim of the second part is to control the DC voltage of the floating bridge and to compensate the reactive power of the motor.

A. *Control of Flux, Speed and Stator Currents*

PI regulators (a) and (b) control the d-q components of the stator currents. Feed-forward signals are added to the output of these regulators to compensate the back electromotive force of the motor and the voltage generated by inverter B. To reduce the effect of a mismatch in the machine parameters, a closed-loop flux weakening strategy is used to regulate the stator flux. PI regulator (c) defines the reference value of current i_{Sd} by comparing the voltage request of inverter A with $V_{A,max}$. If this request overcomes the admissible threshold, the control system reduces $i_{Sd,ref}$, thus decreasing the stator flux. Finally controller (d) chooses

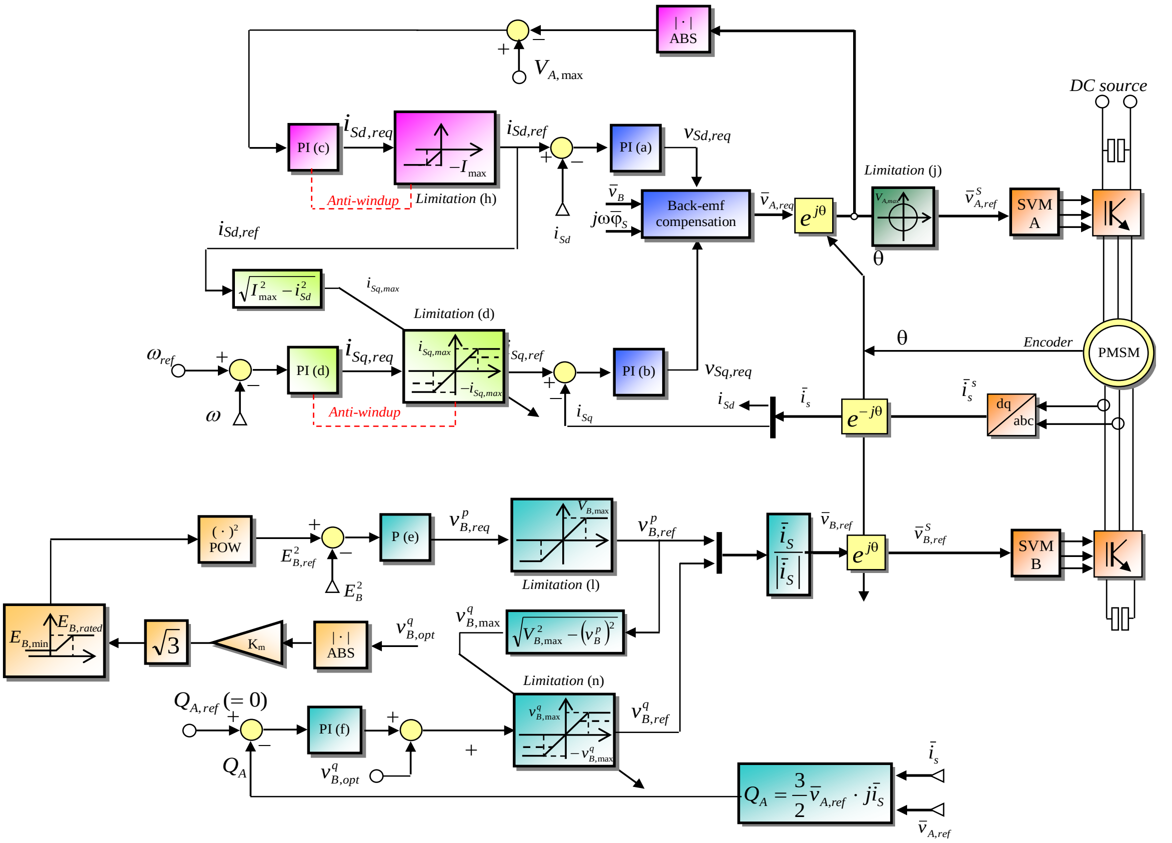

Fig. 6.3. Block diagram of the control scheme for the open-ended permanent magnet machine fed by the dual-inverter system.

the reference value $i_{Sq,ref}$ on the basis of the speed error. This value is bounded by the value $\sqrt{I_{\max}^2 - i_{Sd,ref}^2}$ in order to satisfy the current constraint in every operating condition.

B. *Control of the Floating Capacitor and of the Reactive Power*

Regulator (e) keeps the DC-link voltage E_B at the reference voltage $E_{B,ref}$, whose level is adjusted depending on the voltage resulting from (16), which is necessary to compensate the reactive power of inverter A. A coefficient greater than one is used to take into account that the transient voltage term in (17) can require a significant voltage margin. Since v_B^q is proportional to the motor speed, E_B tends to zero as long as the speed decreases, thus reducing the switching losses of inverter B. PI (f) ensures that inverter A operates at unity power factor by zeroing its reactive power Q_A. The feed-forward signal v_B^q given by (16) is added to the output of PI (f) to improve the dynamic performance. Both PI regulators (e) and (f) are implemented in the reference frame aligned with the stator current space vector.

C. *Experimental Results*

Some experimental results have been performed with a small laboratory prototype to verify the feasibility of the developed control scheme. The specifications of the control board can be found in [52]. The parameters of the drives are the same shown in TABLE 6. The measured signals have been acquired, transferred to a PC and plotted with Matlab.

Fig. 6.4 compares the behavior of a single inverter drive with the dual inverter drive during a start-up transient. As long as the rotor speed is below the base speed, to generate the maximum torque, the current i_{Sd} is zero and the current i_{Sq} is equal to the maximum value $I_{\max}$. The phase angle Φ between the stator current and voltage vectors is roughly constant

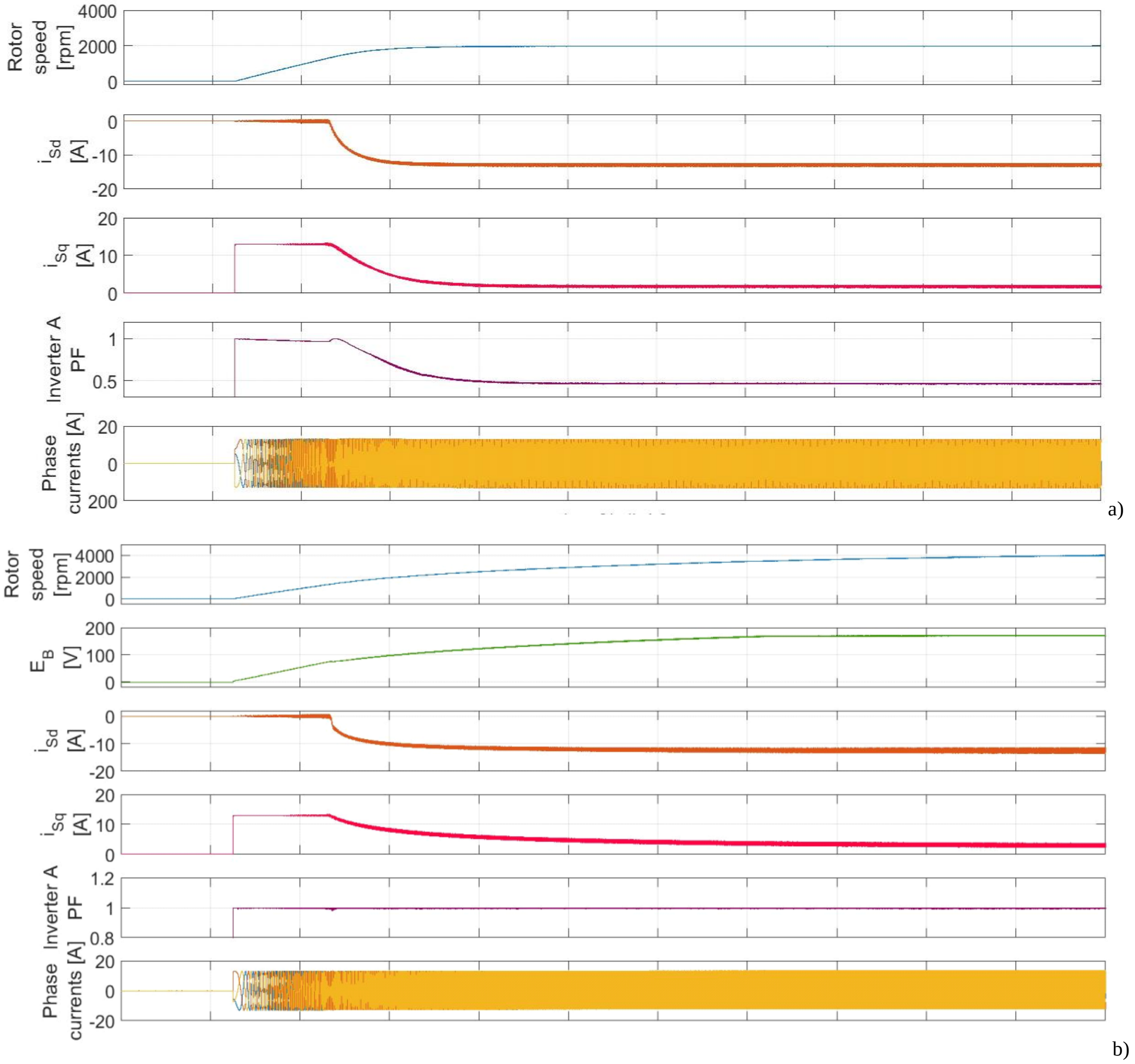

Fig. 6.4. Experimental behavior of the SPM motor during a speed transient from zero to the maximum speed in case of single inverter (a) and dual inverter (b). Time scale: 1s/div.

with speed and can be calculated as follows:

$$\tan \Phi = \frac{L_S I_{\max}}{\varphi_e}. \tag{6.12}$$

In the flux weakening region, the power factor of a single inverter drive rapidly decreases, thus limiting the overall performance.

Conversely, Fig. 6.4(b) shows that the compensation of the reactive power of inverter A allows producing higher torque values at high speed. The maximum speed achievable is

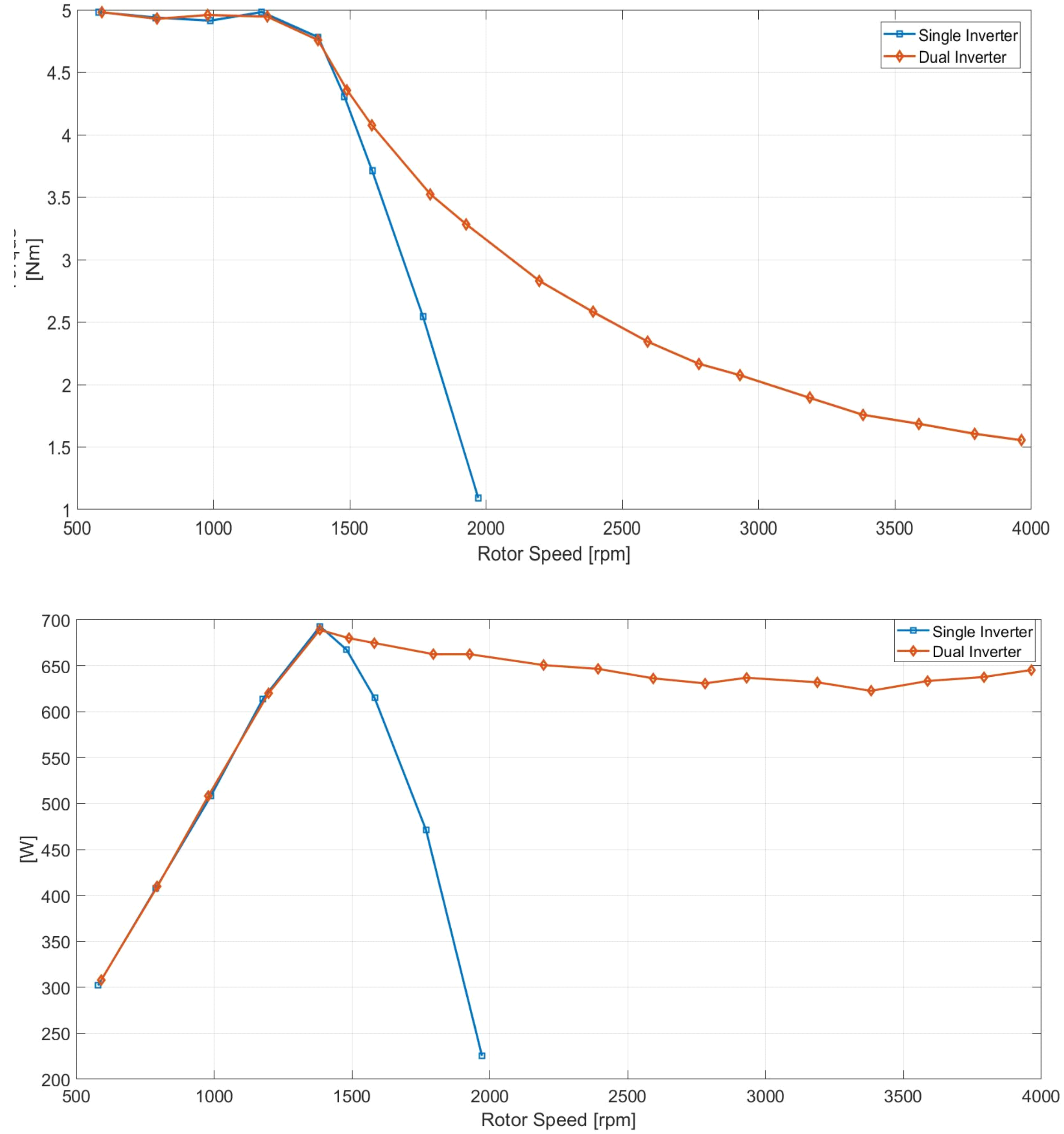

Fig. 6.5. Performance of the drive fed by the dual inverter (red) and by a single inverter (blue) systems.

proportional to the ratio $E_{B,\max}/E_{A,\max}$.

Fig. 6.5 compares the trend of the mechanical torque and the output power when the motor is fed by a single inverter and the dual inverter system, and the ratio $E_{B,max}/E_{A,max}$ is equal to 2. As can be seen, the dual inverter system allows obtaining a threefold increase in the maximum speed of the machine. As a result, the output power is almost constant in the entire flux weakening speed range.

6.3 OVERMODULATION OF THE PRIMARY INVERTER

A similar procedure used for the induction machine in open-end winding, which allows the inverter connected to the primary energy source to overmodulate, can be used for SPM synchronous machine in order to boost the performance of the drive. The harmonics generated by overmodulation can be compensated with the floating bridge inverter by the means of the same set of resonant controllers in the synchronous reference frame written in (5.38). Therefore, the control scheme modifies as shown in Fig. 6.6.

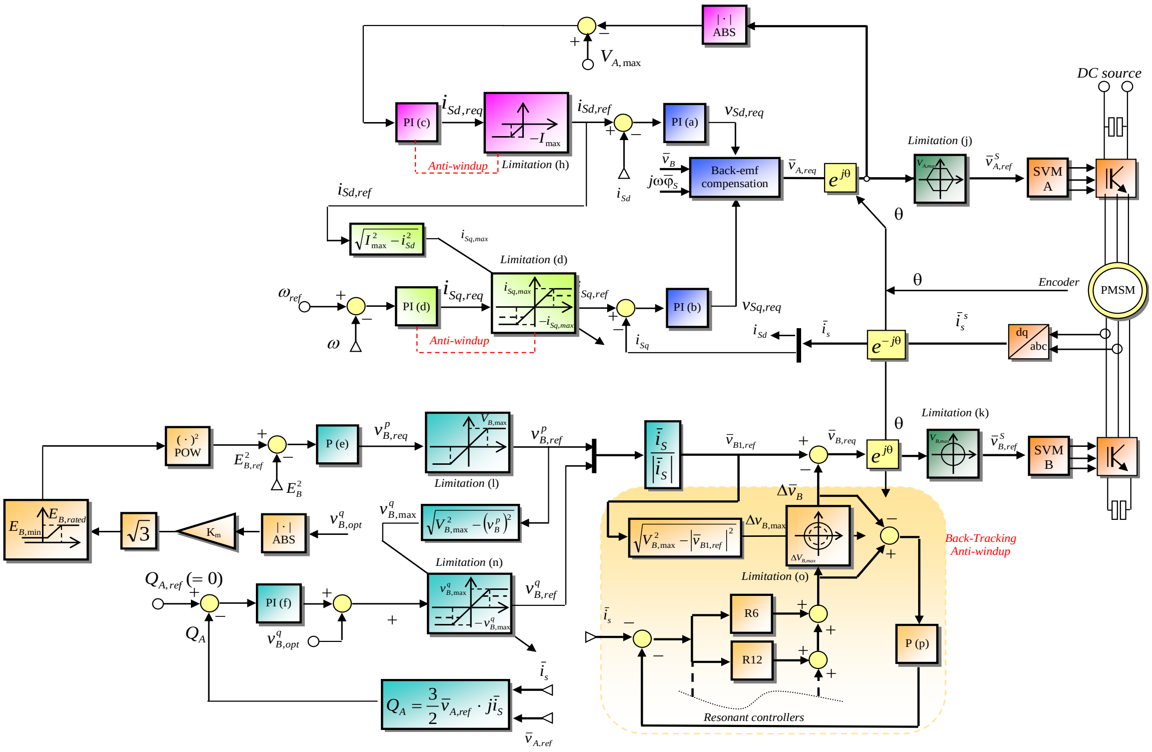

Fig. 6.6. Block diagram of the control scheme for the open-end winding surface permanent magnet machine fed by the dual-inverter system, with the primary inverter operating in voltage overmodulation

A. *Experimental Results*

Fig. 6.7 shows the start-up transient of the drive with the primary inverter in overmodulation. The control of the voltage across the floating capacitor increases with speed, while the power factor of inverter A is kept constant over all the speed range. However, these two variables are mostly influenced by the behavior of the fundamental component of the current, so it could be more of interest to evaluate the waveform of the phase currents in condition of overmodulation.

Fig. 6.8 and Fig. 6.9 show the phase currents at steady state at the rotor speed of 2000 rpm without and with the harmonic compensation respectively. At this speed the drive is already in flux weakening region, hence the overmodulation has been already taken place. It can be seen how the resonant controllers are able to compensate the distortion introduced by the primary inverter and this can be also appreciated from the spectrum of the currents in the two cases, in Fig. 6.10 and Fig. 6.11 respectively.

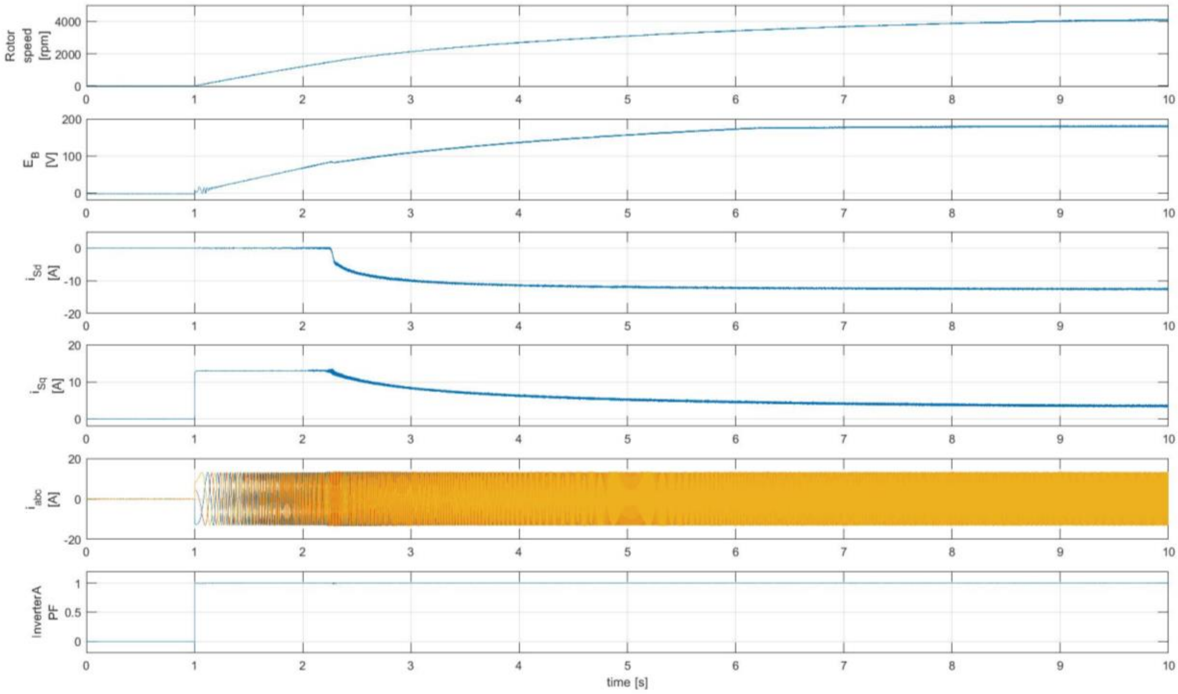

Fig. 6.7. Experimental behavior of the SPM motor during a speed transient from zero to the maximum speed of the dual inverter.

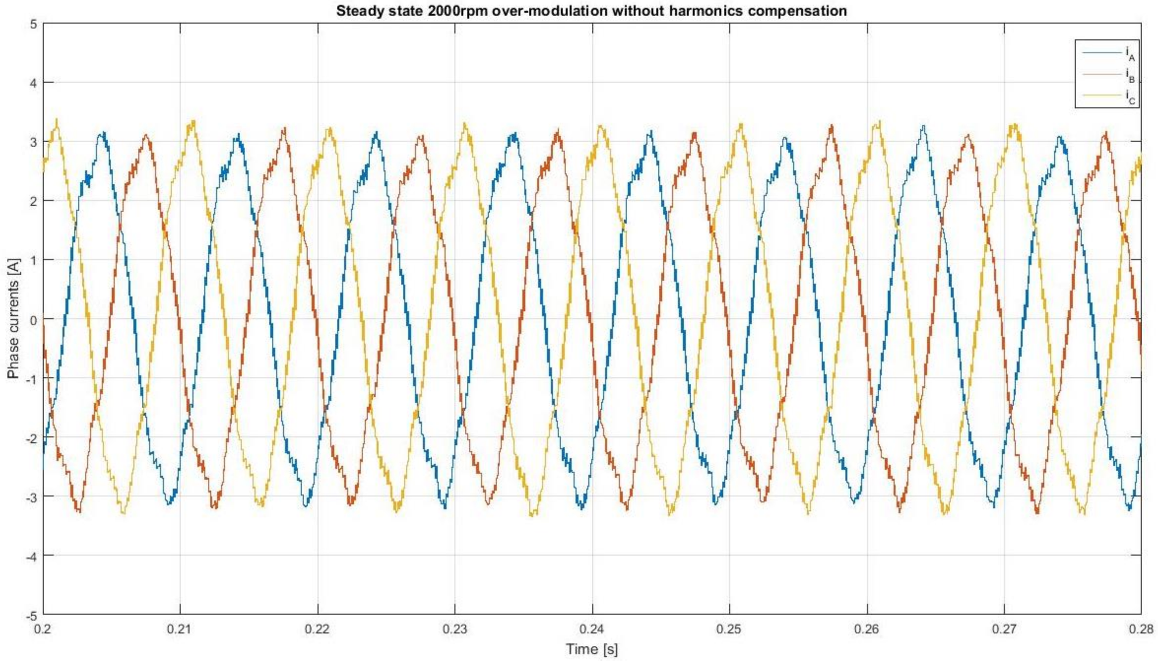

Fig. 6.8. Phase currents in steady-state at 2000 rpm when the harmonic compensation is off.

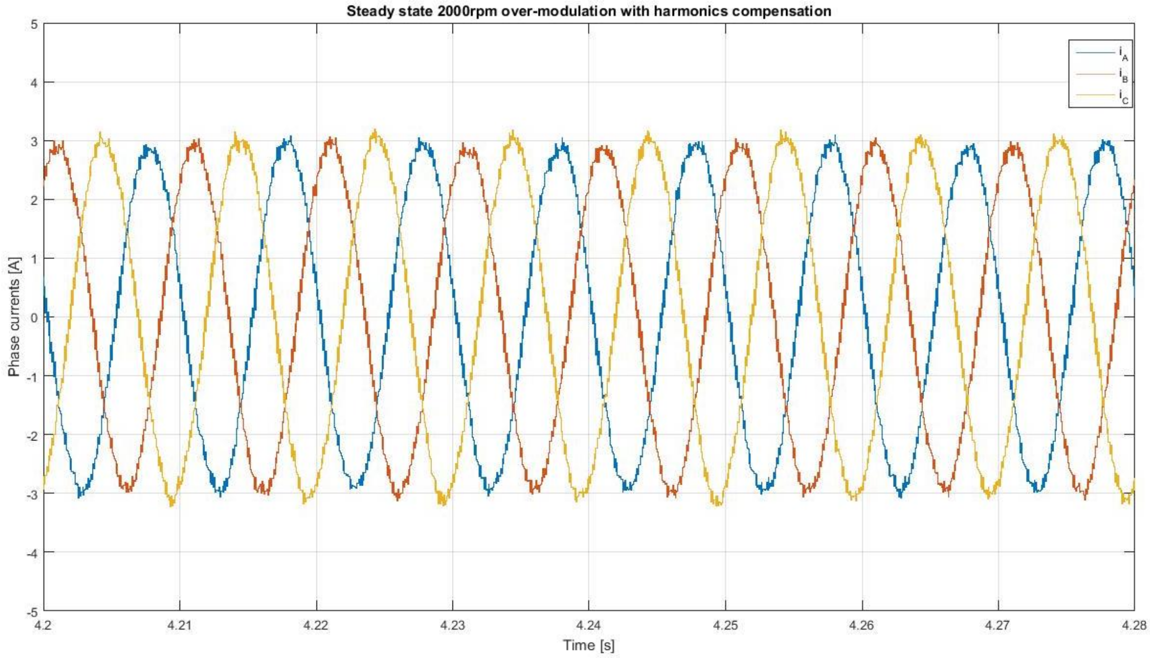

Fig. 6.9. Phase currents in steady-state at 2000 rpm when the harmonic compensation is on.

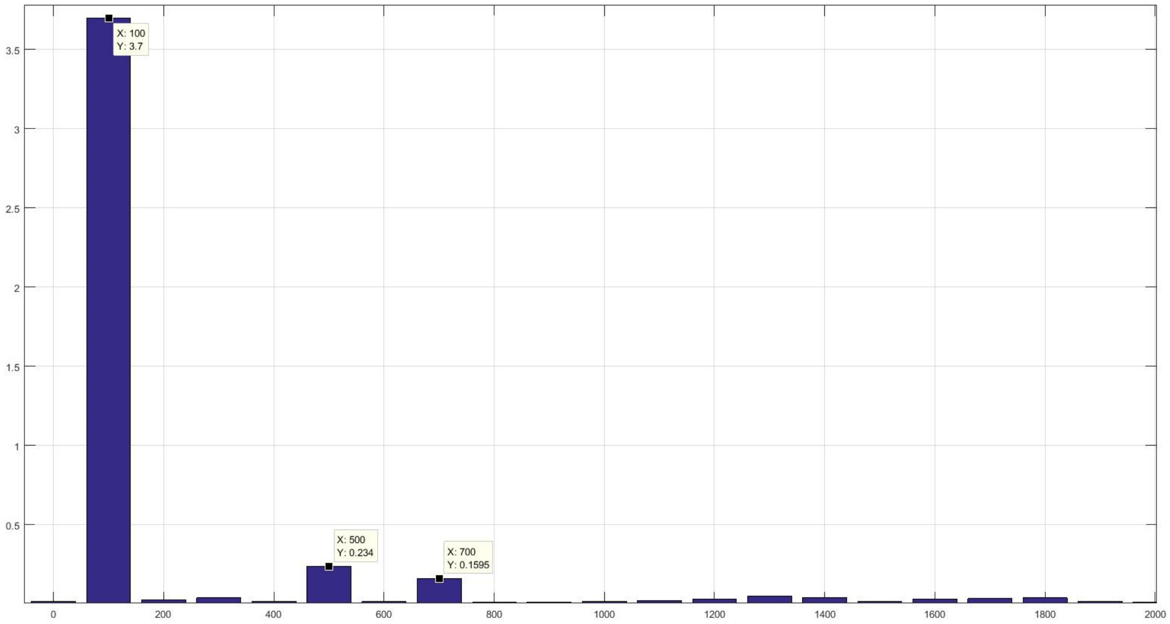

Fig. 6.10. Spectrum of the Phase currents in steady-state at 2000 rpm when the harmonic compensation is off.

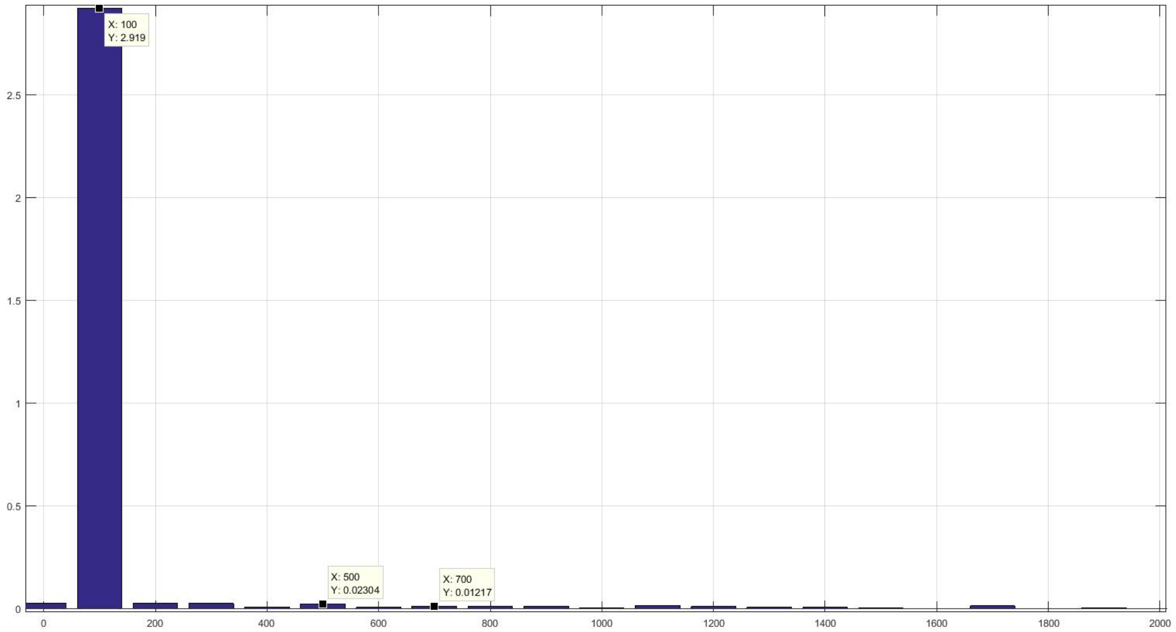

Fig. 6.11. Spectrum of the Phase currents in steady-state at 2000 rpm when the harmonic compensation is not on.

The overmodulation allows the primary inverter to apply a fundamental component of voltage that tends to the theoretical upper limit of $(2/\pi)E_B$ when a six step modulation is used.

This voltage allows to extend the constant torque speed range and the maximum power of 11%, as shown in Fig. 6.12, compared with the dual inverter drive working in linear region.

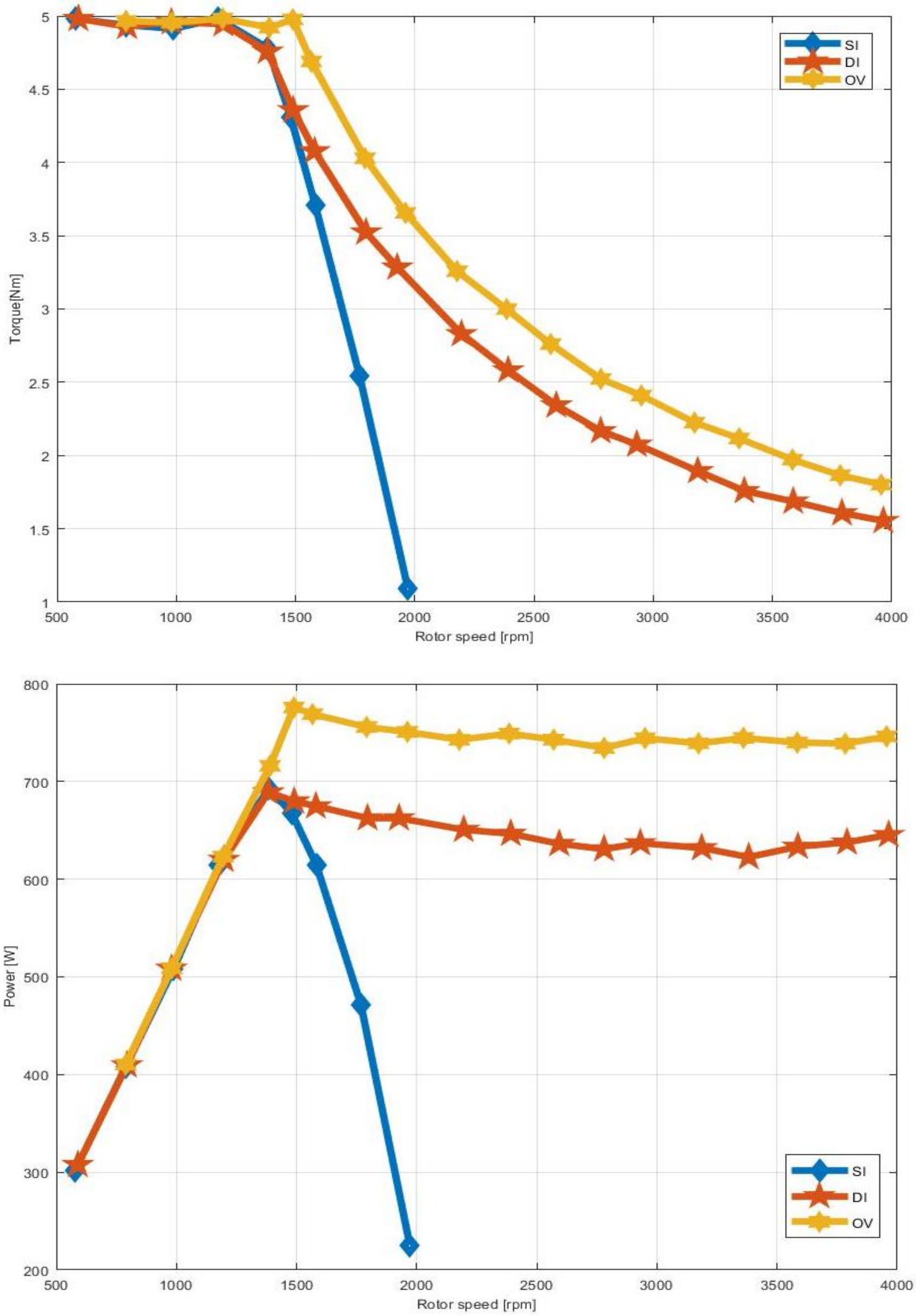

Fig. 6.12. Performance of the drive fed by the single inverter system (blue) by a dual inverter system working in linear modulation (red) and overmodulation (yellow).

6.4 SIX-STEP OPERATION OF THE PRIMARY INVERTER

To further improve the performance of the dual inverter system, it is possible to make the primary inverter work in six-step modulation. This will allow the primary inverter to generate an higher voltage and in addition to drastically reduce the switching losses.

The square wave reference signal is obtained from the sinusoidal reference signal given by the flux and speed control as for the previous schemes. This reference signal is limited to the maximum voltage at the fundamental component of $(2/\pi)E_B$ achievable with a square wave. The difference between the square wave generated and the sinusoidal reference signal represents the harmonic distortion introduced with the six-step modulation and is therefore feedforward to array of resonant controllers for a fast harmonic compensation.

The control scheme used is shown in Fig. 6.13.

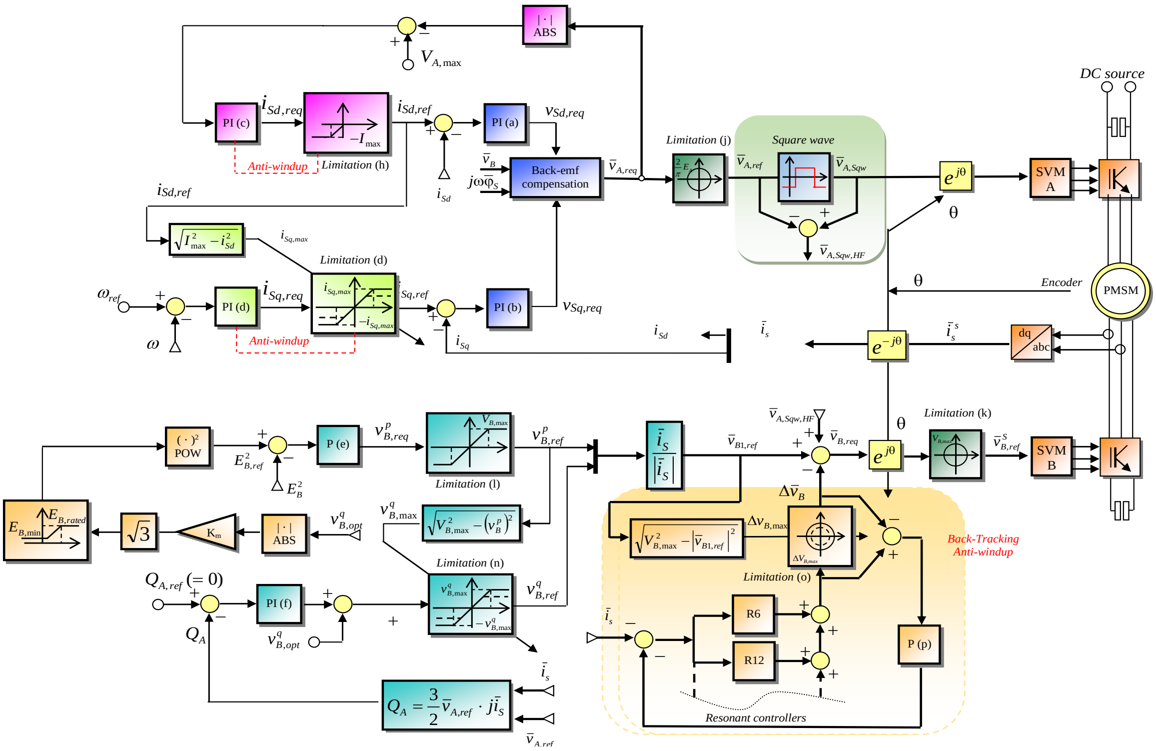

Fig. 6.13. Block diagram of the control scheme for the open-end winding surface permanent magnet machine fed by the dual-inverter system, with the primary inverter operating in voltage six-step modulation

A. *Experimental Results*

Fig. 6.14 shows the steady-state condition at 2000 rpm of the phase current, the square wave phase voltage of the primary inverter with the reference sinusoidal signal and the phase voltage of the floating bridge. The harmonic compensation achieved through the floating bridge, allows the inverter A to work in six-step modulation, while ensuring a low harmonic content in the phase current.

Fig. 6.15 and Fig. 6.16 show the spectrum of the phase currents before and after the harmonic compensation.

In Fig. 6.17 the performance improvements due to the six-step operation have brought an increase of the base speed of 17%, which causes an increase of the maximum power of the drive of the same amount.

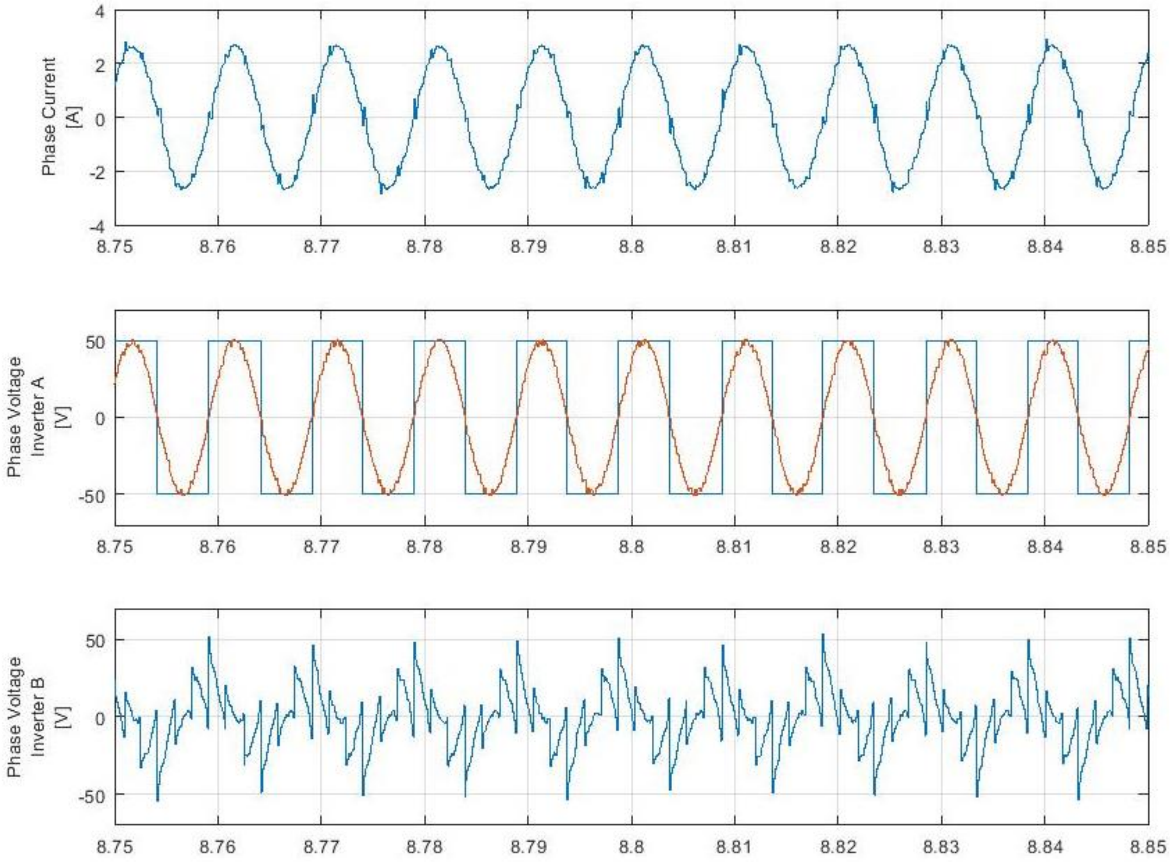

Fig. 6.14. Experimental behavior of the SPM motor with open-end windings in steady-state condition at 2000 rpm, with the primary inverter working in six-step modulation. Time scale: 0.1 s/div.

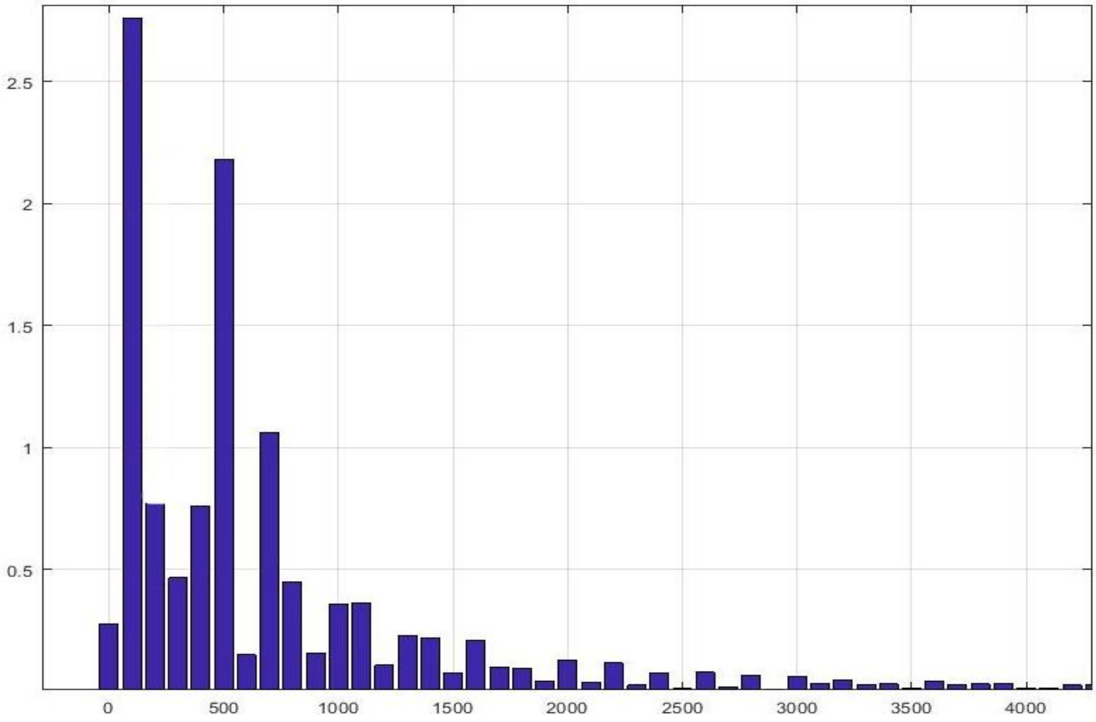

Fig. 6.15. Spectrum of the Phase currents in steady-state at 2000 rpm when the harmonic compensation is off. Scale: Current 0.5 A/div, Frequency 500 Hz/div

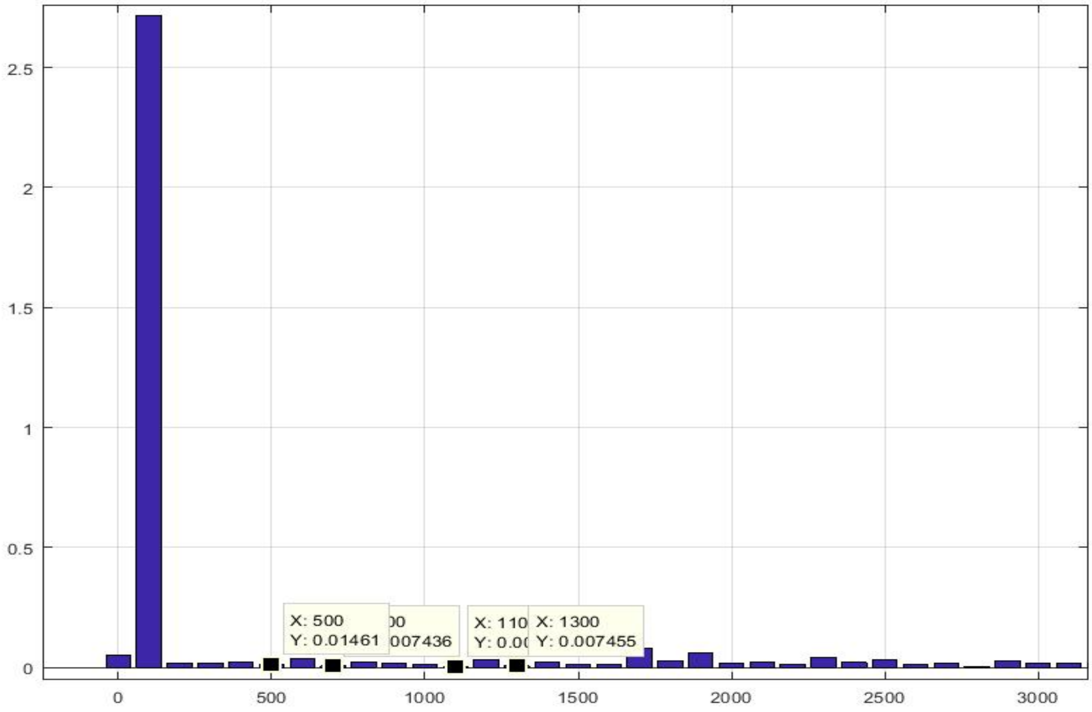

Fig. 6.16. Spectrum of the Phase currents in steady-state at 2000 rpm when the harmonic compensation is off. Scale: Current 0.5 A/div, Frequency 500 Hz/div

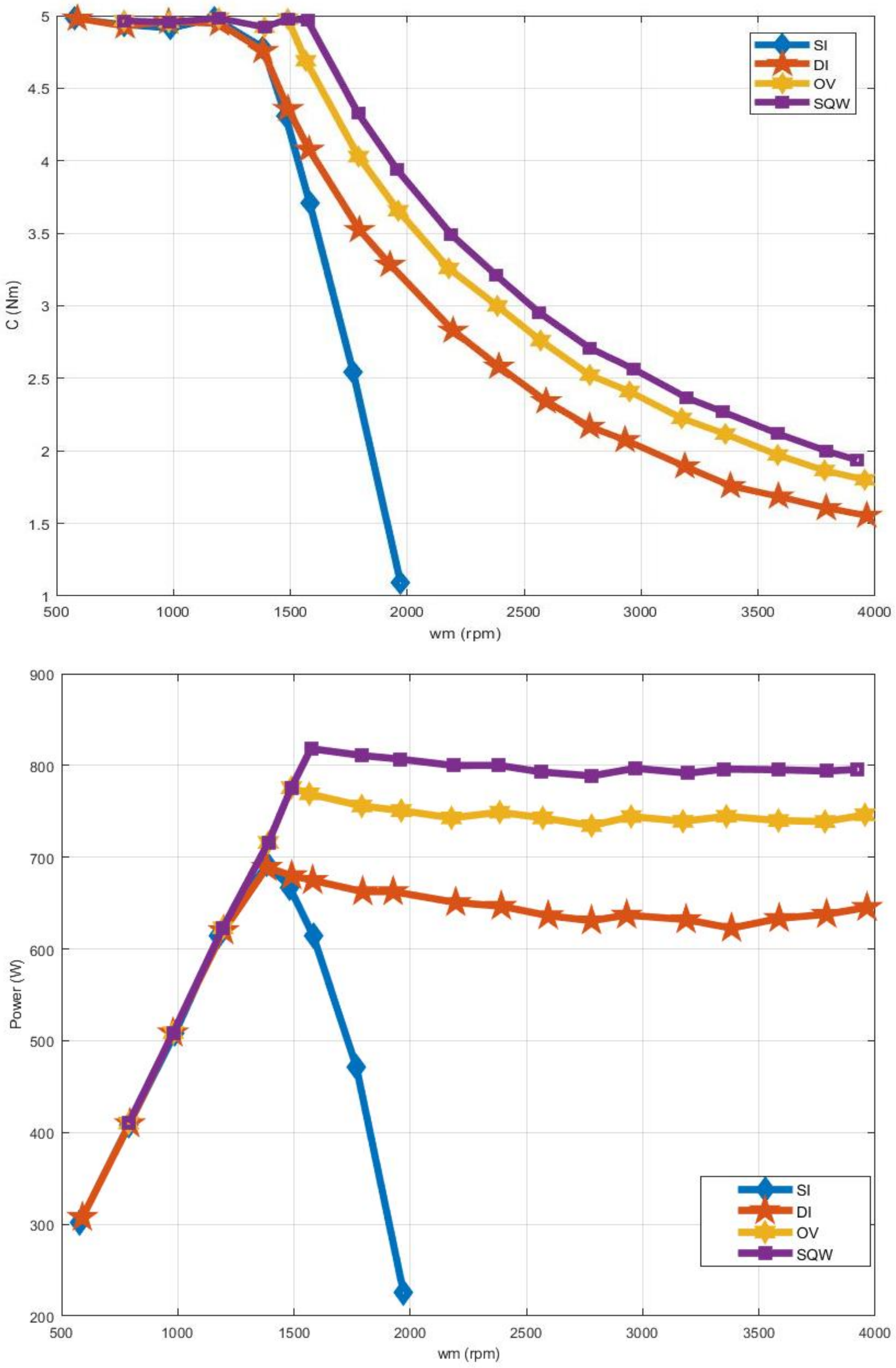

Fig. 6.17. Performance of the drive fed by the single inverter system (blue) by a dual inverter system working in linear modulation (red), overmodulation (yellow) and in six-step mode (purple)

Chapter 7

SYNCHRONOUS RELUCTANCE MOTOR WITH OPEN-END WINDINGS

Despite the lower torque and power densities, synchronous reluctance motors have better efficiencies than induction motors and can operate at high speeds by adjusting the stator flux level.

The dual inverter with a floating capacitor bridge not only extends the motor speed range but can supply the machine with a multi-level PWM voltage to reduce the current ripple, which can be quite significant for sync-rel machines designed for low phase voltages and with a low number of turns.

7.1 SYSTEM MODEL

A. *Mathematical Model and Admissible Domain of Stator Current*

The mathematical model of a sync-rel motor can be written in a d-q reference frame, with the d axis aligned with the direction of maximum reluctance, as follows:

$$v_{Sd} = R_S i_{Sd} - \omega \varphi_{Sq} + \frac{d\varphi_{Sd}}{dt} \tag{7.1}$$

$$v_{Sq} = R_S i_{Sq} + \omega \varphi_{Sd} + \frac{d\varphi_{Sq}}{dt} \tag{7.2}$$

$$\varphi_{Sd} = L_{Sd} i_{Sd} \tag{7.3}$$

$$\varphi_{Sq} = L_{Sq} i_{Sq} = \xi L_{Sd} i_{Sq} \tag{7.4}$$

$$T = \frac{3}{2} p \left(L_{Sd} - L_{Sq} \right) i_{Sd} i_{Sq} = \frac{3}{2} p L_{Sd} \left(1 - \xi \right) i_{Sd} i_{Sq} \tag{7.5}$$

where ω is the angular frequency of the rotor in electric radians, p is the number of pole pairs, T is the electromagnetic torque, v_{Sd} and v_{Sq} are the d-q components of the stator voltage vector $\overline{v}_S$, i_{Sd} and i_{Sq} are the d-q components of the stator current vector $\overline{i}_S$, φ_{Sd} and φ_{Sq} are the d-q components of the stator flux vector $\overline{\varphi}_S$, L_{Sd} and L_{Sq} are the stator inductances, and

R_S is the stator resistance. The saliency ratio ξ of the motor is defined as the ratio of L_{Sq} and L_{Sd}.

It is straightforward to find the voltage constraints for inverter A and inverter B for a syncrel motor with open-end stator windings considering (7.1)-(7.5) in (4.33) and (4.34)

$$|\omega| L_{Sd} \frac{i_{Sd}^2 + \xi i_{Sq}^2}{\sqrt{i_{Sd}^2 + i_{Sq}^2}} \le V_{B,max} \tag{7.6}$$

$$L_{Sd}\left(\xi - 1\right) \frac{\left|\omega i_{Sd} i_{Sq}\right|}{\sqrt{i_{Sd}^2 + i_{Sq}^2}} \le V_{A,max} \,. \tag{7.7}$$

Inequality (7.6) is valid only as long as (7.7) is verified. If $\bar{v}_B$ is saturated, (7.6) must be replaced by the following inequality

$$\left| |\omega| \, \bar{\varphi}_S - V_{B,max} \frac{\bar{i}_s}{|\bar{i}_s|} \right| \le V_{A,max} \,. \tag{7.8}$$

The admissible domain of the stator current vector, resulting from the constraints of the inverter voltages and the stator currents, can be plotted in a complex plane where the horizontal and vertical axes are respectively i_{Sd} and i_{Sq}, as shown in Fig. 7.1.

The admissible current vectors are those delimited by a circle with constant radius I_{max}. Conversely, the curves coming from the voltage constraints (7.7) and (7.6), which depend on the motor parameters, delimit the set of current vectors that can be injected into the machine at a given speed.

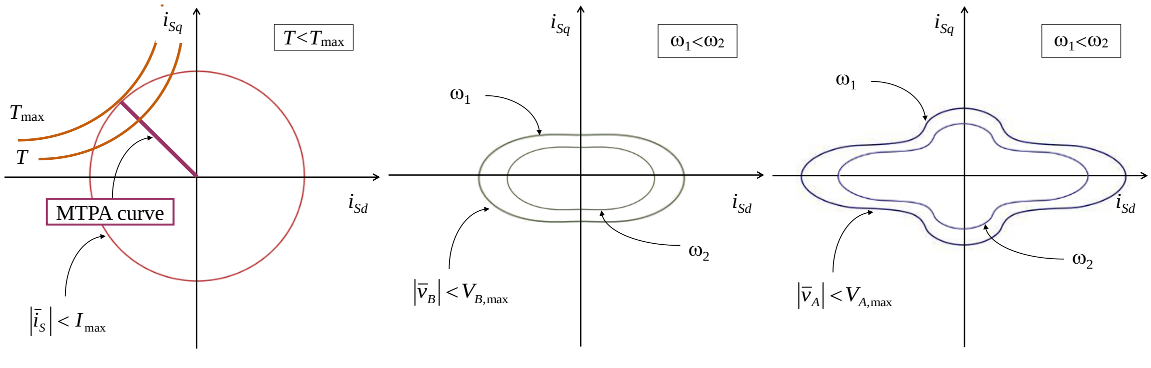

(a) (b) (c)

Fig. 7.1. Representation of the constraints due to maximum inverter current (a), the maximum voltage of inverter B (b) and the maximum voltage of inverter A (c) in plane i_{Sd}-i_{Sq} for a dual inverter drive.

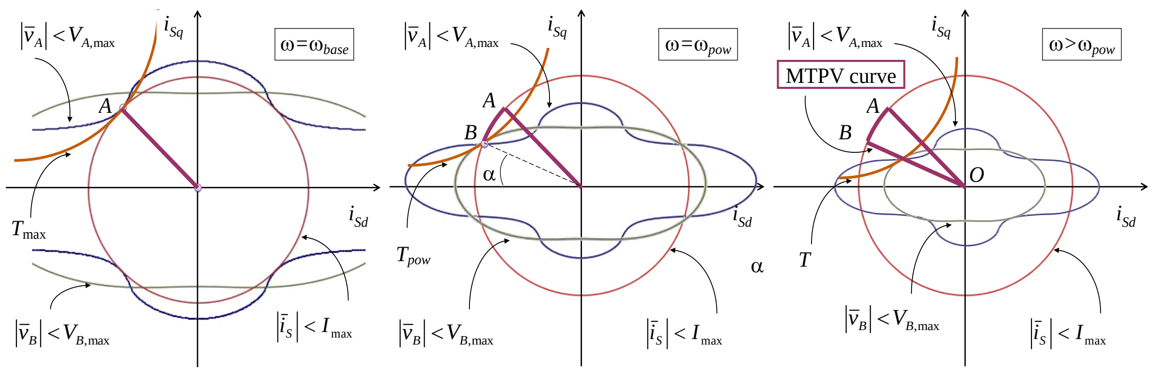

(a) (b) (c)

Fig. 7.2 . Representation of the admissible domain of the stator current at the base speed ω_{base} (a), at speed ω_{pow} (b) and above ω_{pow} (c).

As long as the angular frequency increases, (7.6) generates a set of curves, which are formed by two lobes and tend to become smaller, shown in Fig. 7.1(b). Similarly, (7.6)-(7.8) produces a family of curves with four lobes, shown in Fig. 7.1(c).

The graphical representation of Fig. 7.1 can be used to identify the operating conditions corresponding to the maximum torque capability, since a constant-torque curve in the i_{Sd}-i_{Sq} plane is represented by an hyperbola. The closer the hyperbola is to the origin, the lower the torque.

Furthermore, Fig. 7.1(a) shows the torque locus corresponding to the break-down torque $T_{\max}$. The stator current is represented by a point of the plane that is the intersection of the current circle and the Maximum Torque Per Ampere (MTPA) curve, which is ideally a straight line with a slope of 45 degrees in sync-rel motors.

Fig. 7.2 shows how the domain of the admissible stator current vectors changes as the speed increases, and the corresponding torque capability. Up to the base speed, ω_{base}, the motor can generate the torque $T_{\max}$ and the stator current is represented by point A on the complex plane. When the speed increases above the base speed, Fig. 7.2(b) shows that the operating point corresponding to the maximum torque moves on arc A-B.

Finally, above ω_{pow}, the operating point corresponding to the maximum torque capability at unity power factor is on the segment B-O, which is the Maximum Torque Per Volt (MTPV) curve of the motor.

B. *Resulting Speed Range*

The base speed of the dual inverter system can be calculated from (7.7) when i_{Sd} is $-I_{\max}/\sqrt{2}$ and i_{Sq} is $I_{\max}/\sqrt{2}$.

$$\omega_{base} = \frac{2V_{A,max}}{(\xi - 1) L_{Sd} I_{\max}}. \tag{7.9}$$

Combing (7.1)-(7.4), (4.13) and neglecting the voltage drop on the stator resistance, it is possible to calculate the base speed of the same motor fed by a single inverter. When i_{Sd} is $-I_{\max}/\sqrt{2}$ and i_{Sq} is $I_{\max}/\sqrt{2}$, one finds

$$\omega'_{base} = \frac{V_{A,\max}\sqrt{2}}{L_{Sd} I_{\max}\sqrt{1+\xi^2}}. \tag{7.10}$$

Consequently, the dual inverter system increases the base speed of the machine by a factor $\sqrt{2}\,\frac{\sqrt{1+\xi^2}}{\xi - 1}$, which depends on the saliency ratio. This quantity is equal to the inverse of the motor power factor at the base speed of the single inverter solution as highlighted in (4.39) and shown in the following steps:

$$\bar{v}_{A,base} \simeq j\omega'_{base}\,\bar{\varphi}_S = \omega'_{base} L_{Sd}\left(-\xi i_{Sq} + j i_{Sd}\right), \angle\bar{v}_{A,base} = atan\left(-\frac{i_{Sd}}{\xi i_{Sq}}\right) = atan\left(\frac{1}{\xi}\right) \tag{7.11}$$

The current phase at the base speed is equal to $\frac{3}{4}\pi$, therefore the power factor can be found as:

$$\begin{aligned}
\cos(\varphi) &= \cos\left(atan\left(\frac{1}{\xi}\right) - \left(\frac{3}{4}\pi\right)\right) = \\
&= \cos\left(atan\left(\frac{1}{\xi}\right)\right)\cos\left(\frac{3}{4}\pi\right) + \sin\left(atan\left(\frac{1}{\xi}\right)\right)\sin\left(\frac{3}{4}\pi\right) = \\
&= \cos\left(\frac{\pi}{2} - atan(\xi)\right)\cos\left(\frac{3}{4}\pi\right) + \sin\left(\frac{\pi}{2} - atan(\xi)\right)\sin\left(\frac{3}{4}\pi\right) = \\
&= \frac{\xi}{\sqrt{1+\xi^2}}\frac{\sqrt{2}}{2} - \frac{1}{\sqrt{1+\xi^2}}\frac{\sqrt{2}}{2} = \frac{\xi - 1}{\sqrt{2}\sqrt{1+\xi^2}}.
\end{aligned} \tag{7.12}$$

As long as the speed increases, the operating point corresponding to the maximum torque moves from A to B. The active power delivered by inverter A remains equal to $\frac{3}{2}V_{A,\max}I_{\max}$ so also the mechanical power of the motor is roughly constant (constant power speed range). The position of point B is a function of $V_{B,max}$. If the current components i_{Sd} and i_{Sq} are rewritten in polar form as in (4.40) and (4.41), treating (7.7) and (7.6) as equalities, and solving the resulting set of equations, one can find the value of α and the position of point B. The resulting equation for α is as follows:

$$\frac{1}{\tan\alpha}+\xi\tan\alpha=\frac{V_{B,max}}{V_{A,max}}\left(\xi-1\right) \tag{7.13}$$

The highest speed of the constant power speed range can be found from equation (4.42), where δ is equal to ξ and the excitation flux φ_e is equal to zero.

$$\omega_{pow}=\frac{V_{B,max}}{L_{Sd}I_{\max}\left(\cos^2\alpha+\xi\sin^2\alpha\right)}. \tag{7.14}$$

Above ω_{pow}, the speed is too high and the voltage is not sufficient to inject the maximum current in the motor. In Fig. 7.2(c), this operating condition is represented by segment B-O (MTPV curve).

In an electric drive with a single inverter, it is straightforward to verify that the maximum current can be injected in the motor if the speed is lower than ω'_{pow}:

$$\omega'_{pow}=\frac{V_{A,\max}\sqrt{1+\xi^2}}{\sqrt{2}\xi L_{Sd}I_{\max}}. \tag{7.15}$$

The ratio $\omega_{pow}/\omega'_{pow}$ shows that the constant-power speed range is wider in the dual inverter system, roughly proportionally to the factor $V_{B,\max}/V_{A,\max}$.

The resulting speed ranges of the single-inverter and dual-inverter systems are shown in Fig. 7.3, which has been plotted under the assumption that the voltage drops on the stator resistances and the iron losses are negligible. The parameters necessary to draw the curves are those of a low-power prototype used to carry out the experimental results. The parameters are listed in Table 7. The saliency ratio is 2.36.

TABLE 7 – SYNC-REL OEW- PARAMETERS

T_{rated}	=	5	Nm	R_S	=	0.20	Ω
$I_{S,rated}$	=	21	A_{peak}	L_{Sd}	=	0.0036	H
J_m	=	0.0038	Kg m^2	L_{Sq}	=	0.0086	H
$E_{A,max}$	=	100	V	p	=	3	
$E_{B,max}$	=	300	V	C	=	2.2	mF

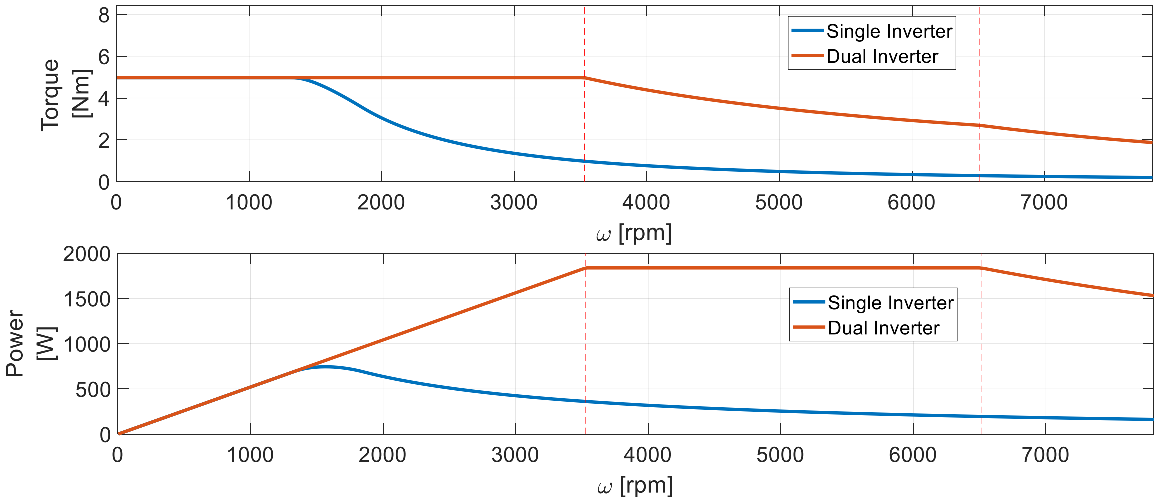

Fig. 7.3. Performance of the drive fed by a dual inverter system (red) and a single inverter system (blue).

As can be seen, the dual inverter system leads to a significant increase in the speed range of the drive. The base speed of the dual inverter drive is 3528 rpm, which is 2.7 times greater than that of the single inverter drive. Furthermore, the constant power speed range, which reaches 6510 rpm, becomes 3.5 times wider in comparison to the single inverter drive, with a noteworthy increase in the output power.

7.2 CONTROL SCHEME

The control scheme of the dual inverter system is shown in Fig. 7.4 and can be divided into two parts. The first part concerns the control of inverter A, which is connected to the power supply. It includes the control loops for speed, flux and stator currents. The aim of the second part is to control the DC voltage of the floating inverter B and to compensate the reactive power of inverter A.

A. *Control of Flux, Speed and Stator Currents*

Two PI regulators control the d-q components of the stator currents. Feed-forward signals are added to the output of these regulators to compensate the back electromotive force of the motor and the voltage generated by inverter B.

To reduce the effect of a mismatch in the machine parameters, a closed-loop flux weakening strategy is used to regulate the stator flux. A PI regulator defines the maximum value of current i_{Sq} by comparing the voltage request of inverter A with $V_{A,max}$ and the voltage request of inverter B with $V_{B,max}$. If one of this signal overcomes the admissible threshold,

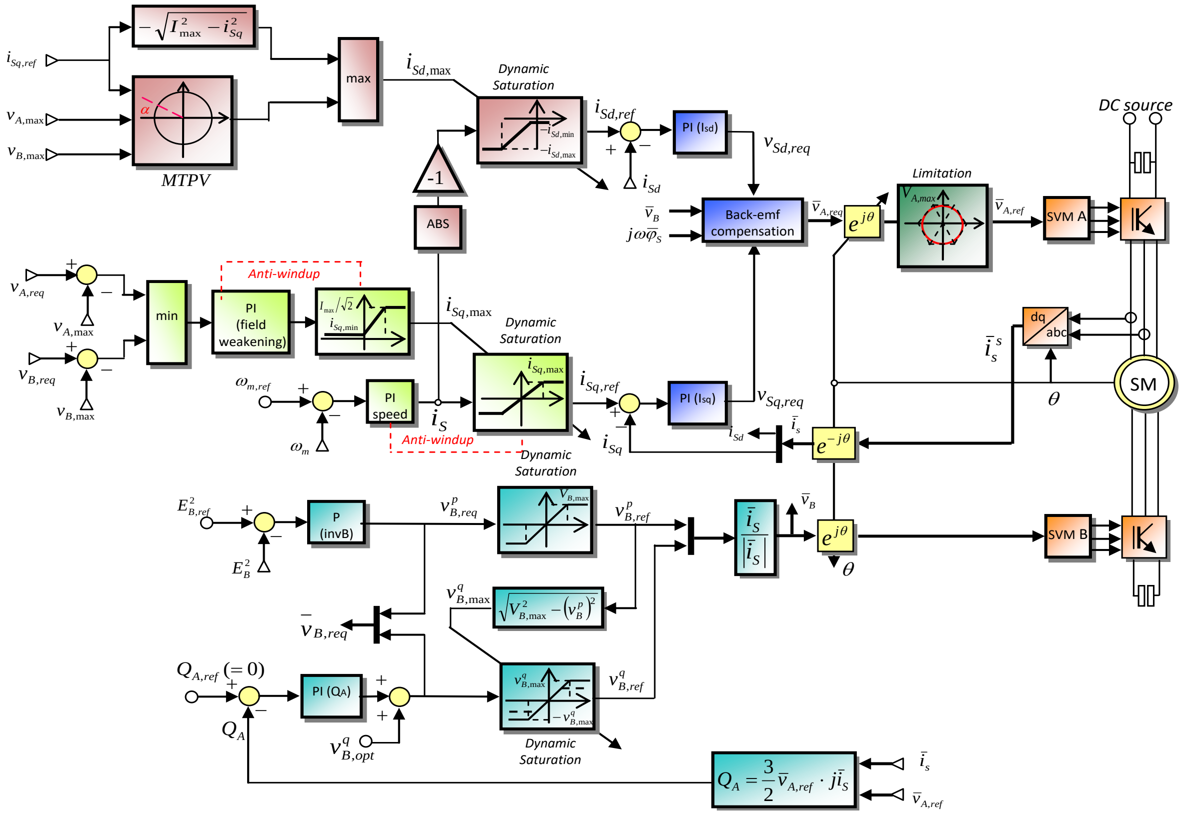

Fig. 7.4. Block diagram of the control scheme for the open-ended sync-rel machine fed by the dual-inverter system.

the control system reduces $i_{Sq,max}$. Since current i_{Sd} is calculated as $-\sqrt{I_{\max}^2-i_{Sq}^2}$, the stator flux decreases. Finally, another PI controller chooses the reference value of i_{Sq} on the basis of the speed error.

B. *Control of the Floating Capacitor and of the Reactive Power*

A PI regulator keeps the DC-link voltage E_B at the reference voltage $E_{B,ref}$, whose level is adjusted depending on the voltage resulting from (4.26), which is necessary to compensate the reactive power of inverter A. Another PI regulator ensures that inverter A operates at unity power factor by zeroing its reactive power Q_A. The feed-forward signal v_B^q given by (4.26) is added to the output of this regulator to improve the dynamic performance.

7.3 *EXPERIMENTAL RESULTS*

Some experimental results have been performed with a small laboratory prototype to verify the feasibility of the developed control scheme. The parameters of the drives are the same shown in TABLE 7.

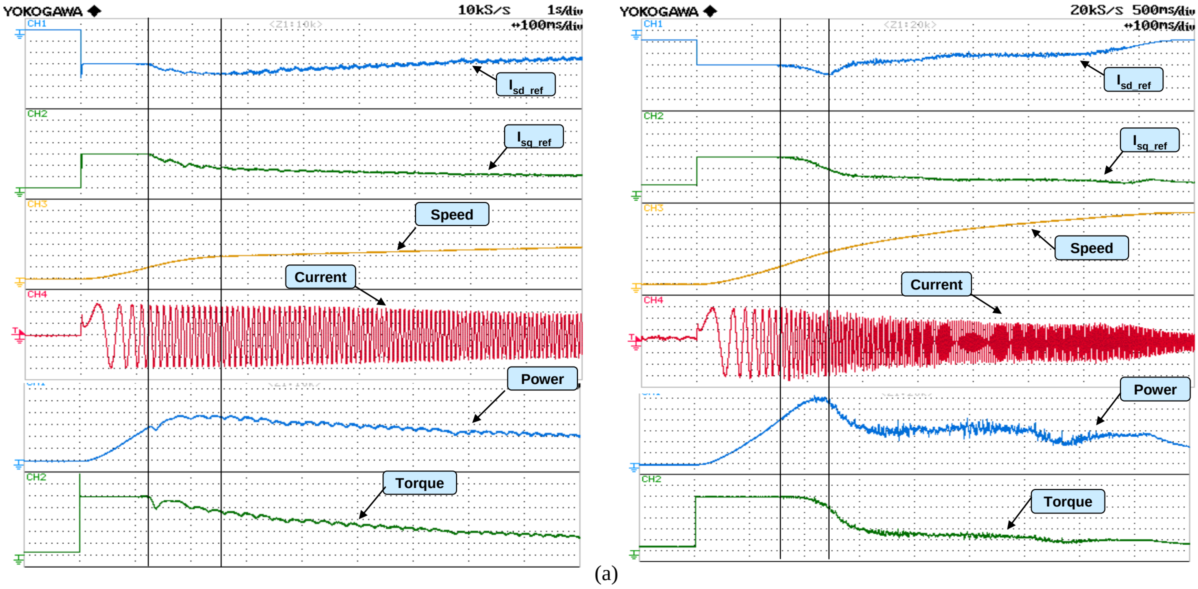

(a) (b)

Fig. 7.5. Experimental behavior of the sync-rel motor during a speed transient from zero to the maximum speed with a single inverter system (a) and a dual inverter system (b). i_{Sd}, i_{Sq} (5 A/div), rotor speed (1000 rpm/div), phase current (7 A/div), power (200 W/div), motor torque (1 Nm/div).

Fig. 7.5 compares the behavior of a single inverter drive and a dual inverter drive during a speed transient up to the maximum speed. As can be noted, current i_{Sq} progressively decreases in both Fig. 7.5(a) and (b). Conversely, current i_{Sd} presents a initial reduction (constant power speed range) followed by a subsequent increase, as soon as the motor reaches the MTPV speed range.

By comparing the peak value of the power delivered to the load shown in Fig. 7.5(b) with the one shown in Fig. 7.5(a), one comes to the conclusion that the performance of the dual inverter system is remarkably greater.

Finally, Fig. 7.6 compares the speed of both drives during the same transient of Fig. 7.5. As can be seen, after 900 ms, the dual inverter system reaches a speed that is nearly twice that of the single inverter system

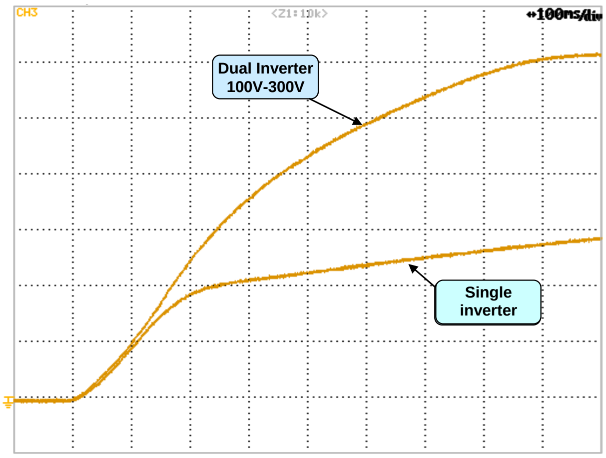

Fig. 7.6. Waveform of the speed of the sync-rel motor with a single inverter system and a dual inverter system during a speed transient from zero to the maximum speed. Speed (1000 rpm/div).

CONCLUSIONS

This PhD work has concerned the development of the control system for grid-connected and front-end converters.

In the first part the control system for an Active Power Filter (APF) has been developed, based on the mathematical model of the application. The current controller, which represents the core of the APF, has been widely investigated. Resonant and repetitive regulators, based on the Internal Model Principle (IMP), have been tested on a laboratory prototype of APF, connected to the power grid through a decoupling inductance, used to compensate the distortion in the line currents generated by a distorting load. Both the regulators have shown great performance in terms of harmonic compensation. The repetitive control has been able to compensate all the high harmonics of the fundamental component of the line currents, requiring quite lower computational burden compared to the resonant controllers. However, the selectivity of the resonant controllers, which uses a resonant regulator for each harmonic that is intended to be compensated, can be useful in case of voltage overmodulation or current saturation, since it allows the control system to choose which harmonics have to be compensated without compromising the overall performance. Therefore, this kind of regulator has been used to develop three different saturation algorithms that adaptively allocate the available voltage among the resonant controllers in such a way that the compensation of the most significant current harmonics is privileged.

The same technologies used to correct the power factor and compensate the current harmonics of the power grid have been successfully applied to motor drives with open-end windings fed by two inverters, where one is a floating bridge. The introduction of a floating bridge allows one to improve the performance of the drive and the quality of the motor currents.

A mathematical model, adaptable to the most common electrical motors, has been developed. On the basis of this model, a control strategy for three different motors has been implemented and tested. This control system has been firstly tested on an induction motor. The power factor correction made by the floating bridge has allowed the drive to extend the constant power speed range, ensuring higher power at high speed compared with the single-inverter system. A further improvement has been achieved with the inverter connected to the primary energy source working in the overmodulation region and the floating bridge working as a harmonic compensator, in order to cancel the distortion introduced by the non linear operation. This feature gives an additional voltage boost and, consequently, a power boost to the drive, without compromising the current quality of the motor.

The same procedure has been adapted to a surface permanent magnet synchronous motor with open-end windings. In addition, for this motor, the six-step modulation has been tested for the primary inverter, while the floating bridge has been used to compensate the high order harmonics of the currents by means of an array of resonant controllers.

Finally, the developed methods of power factor correction have been applied also to a Synchronous Reluctance Motor with open-end windings.

As shown in Chapter 4, the working condition at unity power factor for an electrical motor allows one to extend the constant torque speed range, hence, to increase the absolute value of the output power depending on the power factor at the base speed. By ensuring the unity power factor in flux-weakening region, the dual inverter configuration allows extending the Constant Power Speed Range (CPSR) in proportion to the ratio of the voltage across the floating bridge and the primary inverter.

From the experimental results, it is possible to conclude that the Sync-Rel motor is the one that showed the highest performance improvements in terms of output power, due to its low power factor over the entire speed range. The SPMSM, which works nearly at unity power factor in the constant torque speed range, does not benefit of a significant increase in the absolute value of the output power, but the open-end winding configuration allows extending considerably the constant power speed range and the maximum achievable speed.

TABLE 8 – PERFORMANCE IMPROVEMENTS

Electrical Motor	***Output Power (P_{Dual}/P_{Single})***	***CPSR ($\omega_{pow}/\omega'_{pow}$)***	***Maximum Speed ($\omega_{max}/\omega'_{max}$)***
IM	$\simeq \frac{I_{\max}}{\sqrt{I_{\max}^2 - I_{Sd,rated}^2}}$	$\sqrt{2}\frac{V_{B,\max}}{V_{A,\max}}$	-
SPMSM	1	$\frac{V_{B,\max}}{V_{A,\max}}$	$\frac{V_{B,\max}}{V_{A,\max}}+1$
Sync-Rel	$\sqrt{2}\frac{\sqrt{1+\xi^2}}{\xi-1}$	$\sqrt{2}\frac{V_{B,\max}}{V_{A,\max}}$	-

The induction motor usually presents better power factor, compared to the Synch-Rel motor, but still presents substantial improvements over all the speed range.

In TABLE 8 the performance improvements for each motor are summarized as ratio between the dual inverter and single inverter cases. It is possible to note that the maximum speed ratio for the IM and Sync-Rel cases cannot be quantified since both are theoretically able to achieve infinite speed

References

[1] X. Liang, "Emerging Power Quality Challenges Due to Integration of Renewable Energy Sources," *Industry Applications,* vol. 53, no. 2, pp. 855-866, 2017.

[2] H. Akagi, "Control strategy and site selection of a shunt active filter for damping of harmonic propagation in power distribution systems," *IEEE Trans. Power Del.,* vol. 12, no. 1, p. 354–362, Jan. 1997.

[3] C. D. Schauder and S. A. Moran, "Multiple reference frame controller for active filters and power line conditioners". U.S. Patent 5 309 353, May 3 1994.

[4] S. Bhattacharya, A. Veltman, D. Divan and R. D. Lorenz, "Flux-based active filter controller," *IEEE Trans. Ind. Appl.,* vol. 32, no. 3, p. 491– 502, May/Jun. 1996.

[5] P.-T. Cheng, S. Bhattacharya and D. M. Divan, "Experimental verification of dominant harmonic active filter for high-power applications," *IEEE Trans. Ind. Appl.,* vol. 36, no. 2, p. 567–577, Mar./Apr. 2000.

[6] L. Malesani, P. Mattavelli and S. Buso, "Robust dead-beat current control for PWM rectifiers and active filters," *IEEE Trans. Ind. Appl.,* vol. 35, no. 3, p. 613–620, May/Jun. 1999.

[7] S. Buso, L. Malesani and P. Mattavelli, "Comparison of current control techniques for active filters applications," *IEEE Trans. Ind. Electron.,* vol. 45, no. 5, p. 722–729, Oct. 1998.

[8] S. Buso, S. Fasolo, L. Malesani and P. P. Mattavelli, "A dead-beat adaptive hysteresis current control," *IEEE Trans. Ind. Appl.,* vol. 36, no. 4, p. 1174–1180, Jul./Aug. 2000.

[9] P. Mattavelli and F. P. Marafao, "Repetitive-based control for selective harmonic compensation in active power filters," *IEEE Trans. Ind. Electron.,* vol. 51, no. 5, p. 1018–1024, Oct. 2004.

[10] P. Mattavelli, "A closed-loop selective harmonic compensation for active filters,," *IEEE Trans. Ind. Appl.,* vol. 37, no. 1, p. 81–89, Jan./Feb. 2001.

[11] M. J. Newman, D. N. Zmood and D. G. Holmes, "Stationary frame harmonic

reference generation for active filter systems," *IEEE Trans. Ind. Appl.*, vol. 38, no. 6, p. 1591–1599, Nov./Dec. 2002.

[12] X. Yuan, W. Merk, H. Stemmler and J. Allmeling, "Stationary-frame generalized integrators for current control of active power filters with zero steady-state error for current harmonics of concern under unbalanced and distorted operating conditions," *IEEE Trans. Ind. Appl.*, vol. 38, no. 2, pp. 523-532, Mar/Apr 2002.

[13] C. Lascu, L. Asiminoaei, I. Boldea and F. Blaabjerg, "Frequency response analysis of current controllers for selective harmonic compensation in active power filters," *IEEE Trans. Ind. Elect.*, vol. 56, no. 2, pp. 337-347, Feb. 2009.

[14] R. I. Bojoi, G. Griva, V. Bostan, M. Guerriero and F. F. Farina, "\Current Control Strategy for Power Conditioners Using Sinusoidal Signal Integrators in Synchronous Reference Frame," *IEEE Transactions on Power Electronics*, vol. 20, no. 6, pp. 1402 - 1412, Nov. 2005.

[15] L. Limongi, I. Bojoi, G. B. Griva and A. Tenconi, "Digital Current-Control Schemes," *IEEE INDUSTRIAL ELECTRONICS MAGAZINE*, 2009.

[16] A. G. Yepes, F. D. Freijedo, J. D. Gandoy and O. Lopez, "Effects of Discretization Methods on the Performance of Resonant Controllers," *IEEE TRANSACTIONS ON POWER ELECTRONICS*, vol. 25, no. 7, pp. 1692-1712, 2010.

[17] W. Lu and K. Y. Y. Zhou, "A General Internal Model Principle Based Control Scheme for CVCF PWM Converters," in *2nd IEEE International Symposium on Power Electronics for Distributed Generation Systems*, 2010.

[18] G. Escobar, A. A. Valdez, J. Leyva-Ramos and P. Mattavelli, "Repetitive-Based Controller for a UPS Inverter to Compensate Unbalance and Harmonic Distortion," *IEEE TRANSACTIONS ON INDUSTRIAL ELECTRONICS*, vol. 54, no. 1, pp. 504-511, 2007.

[19] B. Zhang, D. Wang, K. Zhou and Y. Wang, "Linear Phase Lead Compensation Repetitive Control of a CVCF PWM Inverter," *IEEE TRANSACTIONS ON INDUSTRIAL ELECTRONICS*, vol. 55, no. 4, pp. 1595-1603, April 2008.

[20] I. Boldea, L. N. Tutelea, L. Parsa and D. Dorrell, "Automotive electric propulsion systems with reduced or no permanent magnets: An overview," *IEEE Trans. Ind.*

Electron, vol. 61, no. 10, p. 5696–5711, Oct. 2014.

[21] M. Zeraoulia, M. E. H. Benbouzid and D. Diallo, "Electric motor drive selection issues for HEV propulsion systems: a comparative study," *IEEE Trans. Vehic. Technol.*, vol. 55, no. 6, pp. 1756-1764, 2006.

[22] Y. Kawabata, E. Ejiogu and T. Kawabata, "Vector-controlled double-inverter-fed wound-rotor induction motor suitable for high-power drives," *IEEE Trans. Ind. Appl.*, vol. 35, no. 5, p. 1058–1066, Sep./Oct. 1999.

[23] K. Chen, P. Delarue, A. Bouscayrol, P. Vidal and M. Pietrzak-David, "Minimum copper loss and power distribution control strategies of double inverter-fed wound-rotor induction machines using energetic macroscopic representation," *IEEE Trans. Energy Convers.*, vol. 25, no. 3, p. 642–651, Sep. 2010.

[24] G. Poddar and V. T. Ranganathan, "Sensorless field-oriented control for double-inverter-fed wound-rotor induction motor drive," *IEEE Trans. Ind. Electron.*, vol. 51, no. 5, p. 1089–1096, Oct. 2004.

[25] Y. Han and J.-I. Ha, "Single external source control of doubly-fed induction machine using dual inverter," in *Proc. 2013 IEEE Energy Convers.*, Denver, CO, USA, 2013.

[26] J. S. Park and K. Nam, "Dual inverter strategy for high operation of HEV permanent magnet synchronous motor," in *Proc. 41st IAS Annu. Meeting*, Tampa, FL, USA, 2006.

[27] Y. Lee and J.-I. Ha, "Power enhancement of dual inverter for open-end permanent magnet synchronous motor," in *Proc. Appl. Power Electron. Conf. Expo.*, Long Beach, CA, USA, 2013.

[28] R. U. Haque, M. S. Toulabi, A. M. Knight and J. Salmon, "Wide speed range operation of PMSM using an open winding and a dual inverter drive with a floating bridge," in *Proc. 2013 IEEE Energy Convers. Congr. Expo.*, Denver, CO, USA, 2013.

[29] R. U. Haque, A. Kowal, J. Ewanchuk, A. Knight and J. Salmon, "PWM control of a dual inverter drive using an open-ended winding induction motor," in *Proc. Appl. Power Electron. Conf. Expo.*, Long Beach, CA, USA, 2013.

[30] J. Ewanchuk, J. Salmon and C. Chapelsky, "A method for supply voltage boosting in an open-ended induction machine using a dual inverter system with a floating capacitor bridge," *IEEE Trans. Power Electron.,* vol. 28, no. 3, p. 1348–1357, 2013.

[31] J. Kim, J. Jung and K. Nam, "Dual-inverter control strategy for high-speed operation of EV induction motors," *IEEE Trans. Ind. Electron.,* vol. 51, no. 2, p. 312–320, 2004.

[32] M. Mengoni, A. Tani, L. Zarri, G. Rizzoli, G. Serra and D. Casadei, "Control of an open-ended induction machine using a dual inverter system with a floating capacitor bridge," in *Proc. 2015 IEEE Energy Convers. Congr. Expo.*, Montreal, QC, Canada, 2015.

[33] S. Chowdhury, P. Wheeler, C. Gerada and P. C., "A dual two-level inverter with a single source for open end winding induction motor drive application," in *Proc. 2015 17th Eur. Conf. Power Electron. Appl.*, 2015.

[34] S. Chowdhury, P. W. Wheeler, C. Patel and C. Gerada, "A multilevel converter with a floating bridge for open-end winding motor drive applications," *IEEE Trans. Ind. Electron.,* vol. 63, no. 9, p. 5366–5375, Sept. 2016.

[35] S. Foti, "A new approach to improve the current harmonic content on open-end winding ac motors supplied by multi-level inverters," in *Proc. 2015 IEEE Energy Convers. Congr. Expo.*, Montreal, CA, USA, 2015.

[36] S. Pramanick, N. A. Azeez, R. S. Kaarthik, K. Gopakumar and C. Cecati, "Low-order harmonic suppression for open-end winding IM with dodecagonal space vector using a single dc-link supply," *IEEE Trans. Ind. Electron.,* vol. 62, no. 9, p. 5340–5347, Sep. 2015.

[37] M. Boby, S. Pramanick, R. S. Kaarthik, S. A. Rahul, K. Gopakumar and L. Umanand, "Multilevel dodecagonal voltage space vector structure generation for open-end winding IM using a single dc source," *IEEE Trans. Ind. Electron.,* vol. 63, no. 5, pp. 2757-2765, May 2016.

[38] S. Pramanick, M. Boby, N. A. Azeez, K. Gopakumar and S. S. Williamson, "A three-level dodecagonal space vector-based harmonic suppression scheme for open-

end winding IM drives with single-dc supply," *IEEE Trans. Ind. Electron.,*, vol. 63, no. 11, pp. 7226-7233, Nov 2016.

[39] J. Ewanchuk and J. Salmon, "A square-wave controller for a high speed induction motor drive using a three phase floating bridge inverter," in *Proc. 2010 IEEE Energy Convers. Congr. Expo.*, Atlanta, GA, USA, 2010.

[40] T. Gerrits, C. G. E. Wijnands, J. J. H. Paulides and J. L. Duarte, "Dual voltage source inverter topology extending machine operating range," in *Proc. 2012 IEEE Energy Convers. Congr. Expo.*, Raleigh, NC, USA, 2012.

[41] Jones, M. D. M. and E. Levi, "An open-end winding drive with a single dc voltage source," in *Proc. 41st Annu. Conf. IEEE Ind. Electron. Soc.*, Nov. 2015.

[42] X. Xu and D. W. Novotny, "Selection of the flux reference for induction machine in the field weakining region," *IEEE Trans. Industry Applic.*, vol. 28, no. 6, pp. 1353-1358, 1992.

[43] S. H. Kim and S. K. Sul, "Maximum torque control of an induction machine in the field weakening region," *IEEE Trans. Industry Applic.*, vol. 31, no. 4, pp. 787-794, Jul./Aug. 1995.

[44] D. Casadei, M. Mengoni, G. Serra, A. Tani and L. Zarri, "A control scheme with energy saving and DC-link overvoltage rejection for induction motor drives of electric vehicles," *IEEE Trans. Ind. Applic.*, vol. 46, no. 4, pp. 1436-1446, 2010.

[45] M. Mengoni, L. Zarri, A. Tani, G. Serra and D. Casadei, "A comparison of four robust control schemes for field-weakening operation of induction motors," *IEEE Trans. on Power Electronics*, vol. 27, no. 1, pp. 307-320, Jan. 2012.

[46] A. M. El-Refaie and T. M. Jahns, "Comparison of Synchronous PM Machine Types for Wide Constant-Power Speed Operation: Converter Performance," *IET Electr. Power Appl.*, p. 217–222, 2007.

[47] B. Wang, G. L. G. E. Murr, J. Wang, A. Griffo, C. Gerada and T. Cox, "Overall Assessments of Dual Inverter Open Winding Drives," in *IEMDC 2015*, Coeur d'Alene, ID, USA, 10-13 May 2015.

[48] B. Welchko and J. Nagashima, "The influence of topology selection on the design of EV/HEV propulsion systems," in *Power Electronics Letters IEEE Volume 1*, June

2003.

[49] S. Chowdhury, P. Wheeler, C. Gerada and S. L. Arevalo, "A dual inverter for an open end winding induction motor drive without an isolation transformer," in *APEC 2015*, Charlotte, NC, USA , 15-19 March 2015.

[50] L. Rovere, A. Formentini, G. L. Calzo, P. Zanchetta and T. Cox, "IGBT-SiC Dual Fed Open End Winding PMSM Drive," in *IEMDC 2017*, Miami, USA, 21-24 May 2017.

[51] M. Pulvirenti, G. Scarcella, G. Scelba and A. Testa, "On-Line Stator Resistance and Permanent Magnet Flux Linkage Identification on Open-end Winding PMSM Drives," in *ECCE 2017*, Cincinnati, OH, USA, 1-5 Oct. 2017.

[52] A. Galassini, G. L. Calzo, A. Formentini, C. Gerada, P. Zanchetta and A. Costabeber, "uCube: Control platform for power electronics," in *in 2017 IEEE Workshop on Electrical Machines Design, Control and Diagnosis (WEMDCD)*, 2017.